A: Universality in Vortex Formation
B: Evaluation of Mach Wave Radiation in a Supersonic Jet

Thesis by
Kamran Mohseni

In Partial Fulfillment of the Requirements
for the Degree of
Doctor of Philosophy

California Institute of Technology
Pasadena, California

2000

(Submitted April 2000)

Acknowledgements

I would like to thank my advisors, Professors T. Colonius and M. Gharib for their patience, support and guidance throughout this study. Their scientific intuition has been an inspiration.

I would like to thank my committee members Professors T. Colonius, M. Gharib, J. Marsden, A. Leonard, and C. Brennen for their comments. I have benefitted through stimulating conversations with Professors M. Cross, P. Weichman, and J. Marsden on statistical equilibrium theory; A. Leonard on vortex filament method; and S. Lele on adjoint technique in compressible flow. I would like to thank Professor J. Freund at the university of California/Los Angles for providing the raw DNS data used in the second part of this study. I am grateful to Professor J.T. Stuart, FRS at Imperial College/London for his advice and support which led to my studies at Caltech.

I have enjoyed the collaborations and discussions with people in the CFD Lab, in particular productive collaboration with Mr. H. Ran on numerical study of pinch-off process, and many computer advises from Mr. J. Eldredge.

I would like to thank J. Forss for her continuous support and encouragement over the last three years and for her careful proof reading of this thesis.

Finally my deepest gratitude goes to my parents and my brothers and my sister for their constant support, unlimited love and encouragement.

Abstract

In this thesis two distinct features of coherent structures are investigated.

In Part I a model for the pinch-off process in vortex ring formation is developed. The predicted nondimensional stroke length L/D (referred to as "formation number") satisfactorily matches experimental observations. The model introduces two nondimensional parameters that govern the limiting value of the formation number: a nondimensional energy and circulation, E_{nd} and Γ_{nd}, respectively. The predicted value of E_{nd} also matches well with the experimental data. The limiting value for the new nondimensional circulation is predicted to be in the range $1.77 \lesssim \Gamma_{nd} \lesssim 2.07$. We perform detailed computations of vortex ring formation by nonconservative forcing. The validity of the assumptions in our model is verified in these computations. Some techniques for generating fat rings are successfully investigated, resulting in generation of vortex rings with Hill's like properties.

We consider thermodynamics of the vorticity density field (ω/r), and we develop a statistical equilibrium theory for axisymmetric flows. It is shown that the statistical equilibrium of an axisymmetric flow is the state that maximizes an entropy functional constrained to the invariants of motion. Furthermore, it is shown that the final equilibrium state satisfies a variational principle similar to Kelvin's variational principle.

In Part II Mach wave radiation mechanisms in a fully expanded supersonic jet is studied. We compare a direct numerical simulation (DNS) of a 1.92 Mach number jet with a linearized Navier-Stokes (LNS) simulation. The numerical integration technique, inflow boundary conditions, and grid distributions are the same in both simulations. We found that the generated noise in the DNS calculation is dominated by the first two azimuthal modes, and contributions from all other azimuthal modes were limited to less than 1.5 dB in the acoustic field. The total directivity of the sound field in the LNS matches reasonably well with the sound field of the DNS data. At the peak Strouhal frequency, particularly for the azimuthal mode $n = 1$, the amplification of flow variables in the LNS closely matches that of the DNS data. However, for frequencies away from the peak Strouhal number the DNS data shows amplification rates comparable to those of the peak Strouhal number, while in the LNS data any disturbances away from the peak Strouhal number are highly damped. These extra noise sources in the DNS data have the characteristics of a nonlinear interaction

among various modes.

The noise generated by the first two modes in the linearized computation is substantially weaker than in the DNS. For example, in the near acoustic field, at a distance of 6 jet diameters from the jet centerline, the sound pressure level in the linearized computation is as much as 8 db smaller than the DNS results. We observed that the maximum amplification rate for the DNS data occurs at an axial location further downstream than for the LNS data, which corresponds to regions around and beyond the end of the potential core. Our results indicate that the missing sound generation mechanisms in the LNS computation at the frequencies considered in this study can be attributed to the non-linear sound generation mechanisms, that are not captured in linear theories.

Contents

List of Figures

List of Tables

Part I

Universality in Vortex Formation

Chapter 1

Introduction

Vortex rings are among the simplest three-dimensional vortical structures. Their persistence and compactness have fascinated fluid dynamists for many years. Vortex rings are quite common in nature (*e.g.*, see [70]), and perhaps the most familiar example is the smoke ring. Due to their simplicity and the variety of unanswered questions, they are still a fertile research area. In general, vortex rings are defined by a confined region of vorticity with closed vortex lines. This confined region is generally referred to as the core of the vortex ring. A vortex ring need not to be axisymmetric; however, to simplify our analysis we will concentrate on axisymmetric rings only.

The generation, formation, evolution and interactions of vortex rings have been the subject of numerous studies. There are many ways to create a vortex ring. One way is to apply a unidirectional impulse to a circular region of a fluid medium. In this case the vortex ring is characterized by its azimuthal vorticity in a toroidal region around the direction of the impulse. A practical way to create a vortex ring in this way is when a disk is dragged in the direction normal to its surface. This way an impulsive force will be imparted on the fluid, resulting in a vortex ring translating in the direction of the disk movement. In the laboratory, however, vortex rings can be generated by the motion of a piston pushing a column of fluid of length L (see figure 1.1) through an orifice or nozzle of diameter D. The boundary layer at the edge of the orifice or nozzle will separate and roll up into a vortex ring, as depicted in figure 1.2. The mathematical foundations of vortex rings are well provided in Saffman's book [118]. Much of our current understanding of vortex ring phenomena and

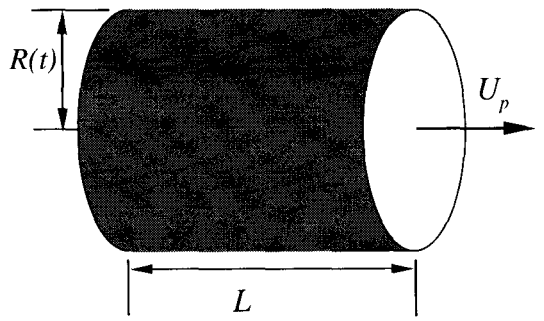

Figure 1.1 A slug of fluid.

unresolved problems are gathered in the review papers by Shariff and Leonard [124] and Lim and Nickels [66].

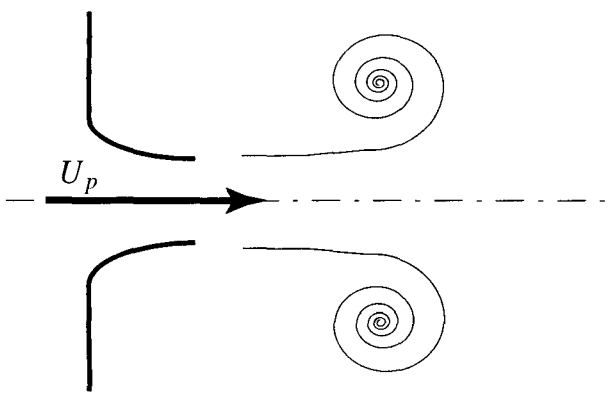

Figure 1.2 Vortex roll up at the exit of an orifice.

1.1 Vortex Pinch-off Process

The present work deals with the so called "pinch-off" process, where a leading vortex ring separates from a trailing starting jet for long stoke lengths in a cylinder-piston mechanism. An important problem in vortex ring generation is to determine how much circulation and energy can be delivered to the vortex ring by the apparatus. This work was motivated by the recent experimental observations in vortex ring generation by cylinder-piston mechanism. The experiments of Gharib, Rambod and Shariff [46] (hereafter denoted as GRS) have shown that for large piston stroke vs. diameter ratios (L/D), the generated flow field consists of a leading vortex ring followed by a trailing jet. They observed that for a set of flow parameters, there is a limiting stroke length that imposes an upper bound on the circulation that a vortex ring can acquire. The vorticity field of the formed leading vortex ring is disconnected from that of the trailing jet at a critical value of L/D (dubbed the "formation number"), at which time the vortex ring attains a maximum circulation. Furthermore, they observed that the maximum circulation is achieved for a narrow range of the formation number $F = L/D$ between 3.6 and 4.5 for a variety of exit diameters and exit plane geometries. For the average discharged velocity $\bar{U}_p$, the stroke length L is given by $L = \bar{U}_p T_f$, where T_f is the discharge time (formation time). Therefore, $F = T_f$.

An explanation for this effect was given based on the Kelvin variational principle (see [46] and section 3.3), which states that steadily translating vortex rings have maximum energy with respect to isovortical perturbations that preserve impulse. In simple terms, the idea is as follows. The piston delivers circulation to the flow at a certain rate. At early times this circulation is delivered to the leading vortex ring. As the circulation of this vortex ring grows, the ring eventually obtains the maximum Kelvin energy. At this point the shear layer cannot deliver more circulation to the leading vortex ring, and therefore, the vortex ring separates from the trailing jet and translates downstream faster than the following shear layer. Thus, the ring pinches off at the point in time when it obtains its maximum Kelvin energy. Alternative explanations for the pinch-off process are presented in section 4.3. In chapter 2 (see Mohseni and Gharib [89] as well) a theoretical model to predict the formation number is considered. The fluid discharging from the cylinder is modeled as a slug-flow, and it is assumed that at the moment of pinch-off the invariants of the resulting vortex ring

can be approximated by the invariants of a vortex in the family of Norbury vortices. While the model is crude, it predicts the range of formation numbers observed in the experiments. This model is based on relaxation ideas rather than focusing on the the dynamics of the shear layer during the formation process. Therefore, we view the pinch-off process as a relaxation from an initial state of an axisymmetric flow to a final equilibrium state. The equilibrium state must be consistent with the known results for steadily translating vortex rings (*e.g.*, Kelvin variational principle). Consequently, in chapter 3 a general theory of statistical equilibrium theory for axisymmetric flows are developed (following Miller [81] and Miller, Weichman, and Cross [82]). The Euler equations are convectively nonlinear (and therefore have the filamentation problem), making them unsuitable for long time calculations toward an equilibrium state. However, the resulting equation from the statistical equilibrium theory is exact and valid over coarse grains. Therefore, it requires much less computational resources to obtain the equilibrium state. Computational verification of our model, as well as verification of new ideas on how to generate thicker vortex ring, and validation of the assumptions in our model of chapter 2 are explored in chapter 4.

In this study we focus on vortex ring formation by axisymmetric mechanisms, in particular cylinder-piston mechanism and nonconservative forcing of axisymmetric Navier-Stokes equations. While experimental evidence [46] indicates that the formation number for pinched off vortex rings are the same for both laminar and turbulent vortex rings, our computations are focused on laminar rings only. We refer to pinch-off Universality in vortex ring formation with these limitations in mind.

Chapter 2

A Model for Universal Time Scale of Vortex Ring Formation

There is strong evidence in support of the notion that the formation of vortex rings is mainly an inviscid process. This can be easily checked by comparing the relaxation time toward a steady vortex ring with the viscous diffusion time at high Reynolds numbers. Under the inviscid approximation, the long-time behavior of a vortical flow is characterized by an infinite number of invariants of the axisymmetric Euler equation [85]. Any accurate model for vortex ring formation must respect these invariants.

The purpose of this chapter is to show that the formation number can be predicted analytically, based on simple assumptions on the formation process. To develop our model we make two assumptions. First that the discharge process of the fluid out of the cylinder can be predicted by a slug model. Second, that at the pinch-off moment the invariants of the resulting vortex ring can be approximated by those of a vortex in the family of Norbury vortices [101]. While physical vortex rings have peakier vorticity distributions (ω) than those with uniform vorticity density (ω/r), such as of the Norbury family of vortices, the quantitative behavior, and in particular the stream lines, are very similar [131]. These considerations along with the fact that Norbury family of vortices are very well documented suggest that for the limiting process under consideration the Norbury vortices can be considered as a first approximation to more general vorticity distributions. Peakiness of the vorticity profiles in this context is considered in more detail in [46]. Furthermore, the experimental results provided by Gharib *et al.* [46] for different velocity profiles of the piston

and exit conditions suggest that the limiting formation number is not very sensitive to the vorticity distributions. This is physically manifested in constant values for nondimensional energy E_{nd} and circulation Γ_{nd} (both quantities are defined later) for the leading vortex of a pinched off jet.

The Norbury family of vortices are steady solutions to the axisymmetric Euler equations. They are characterized by the parameter α_N with $0 < \alpha_N \leq \sqrt{2}$. Here α_N is defined as the nondimensional mean core radius. The family ranges from vortex rings of small cross-section, where $\alpha_N \to 0$, to Hill's spherical vortex, for which $\alpha_N = \sqrt{2}$. It has already been shown by Wan [156] that the Norbury family of vortices are the solution of a maximization problem on the energy function subjected to fixed impulse and circulation.

2.1 Slug Model With Time Varying Exit Diameter and Velocity

To be able to extend our results to the case of a time varying exit diameter or piston velocity, in this section we derive an extension of the well-known slug model, where the slug velocity and diameter at the nozzle exit are functions of time. The circulation, impulse and energy of an infinitesimal fluid element at the exit cross section of the nozzle are calculated as follows. Consider a fluid element with radius $R(t)$ and thickness dx at the exit cross section of the nozzle (see figure 2.1). If we neglect the boundary layer thickness at the nozzle wall we can write

$$\frac{d\Gamma}{dt} = \int \omega U dr = \int \frac{\partial}{\partial r}\left(\frac{U}{2}\right) dr = \frac{1}{2}U^2, \tag{2.1}$$

where ω is the azimuthal vorticity and $U(t)$ is the velocity at the nozzle exit. Therefore, the circulation generated by such a fluid element may be calculated as

$$d\Gamma = \frac{1}{2}U^2 dt. \tag{2.2}$$

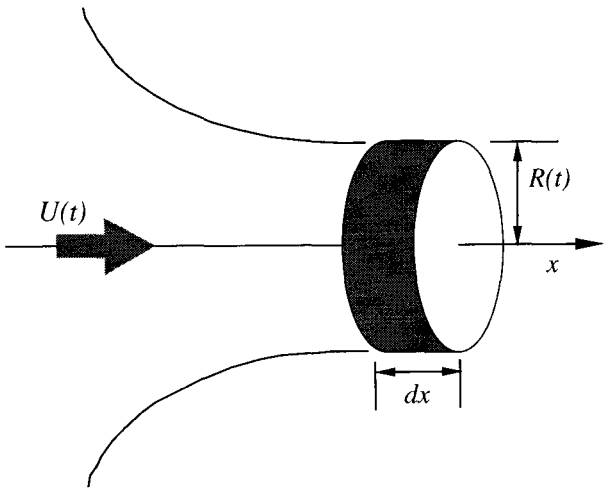

Figure 2.1 Slug model fluid at the exit of a nozzle with time varying diameter and piston velocity.

Similarly, the impulse and energy of the fluid element can be approximated by

$$dI = \pi R^2 U^2 dt, \tag{2.3}$$

$$dE = \frac{\pi R^2}{2} U^3 dt. \tag{2.4}$$

Therefore, one can write

$$d\Gamma = \frac{dI}{2\pi R^2}, \tag{2.5}$$

$$dE = \frac{U}{2} dI. \tag{2.6}$$

An estimate for the total circulation, impulse, and energy of such a model is easily obtained by integrating equations (2.2-2.4) over time. In the case of a slug of fluid with constant diameter $D = 2R$, length L, and with uniform velocity U_p we obtain the well-known expressions for the kinetic energy per unit density, circulation, and impulse per unit density [124]

as

$$E = \frac{1}{8}\pi D^2 L U_p^2 = \frac{U_p}{2} I, \tag{2.7}$$

$$\Gamma = \frac{1}{2} L U_p, \tag{2.8}$$

$$I = \frac{1}{4}\pi D^2 L U_p = \frac{1}{2}\pi D^2 \Gamma. \tag{2.9}$$

2.2 Model

Before developing the model we would like to make an interesting point. Using equations (2.7-2.9) we can write

$$E = \frac{I\Gamma}{L}. \tag{2.10}$$

Hence, for fixed impulse and circulation (and therefore from (2.9) for fixed D) the minimum stroke length L, which results in a Norbury vortex, maximizes the energy.

The corresponding invariant quantities for the Norbury vortices are nondimensionalized as follows:

$$E = \left(\Omega \alpha_N^2 l^2\right)^2 l^3 E_N, \tag{2.11}$$

$$\Gamma = \left(\Omega \alpha_N^2 l^2\right) l \Gamma_N, \tag{2.12}$$

$$I = \left(\Omega \alpha_N^2 l^2\right) l^3 I_N, \tag{2.13}$$

where the subscript N refers to the corresponding nondimensional quantity for the Norbury vortices, $\Omega = \omega / r$ is the vorticity density, and l is the vortex radius (see [101]). For future reference we note that the dimensional translation velocity U_{tr} and the nondimensional translation velocity U_N of the Norbury vortices are related by

$$U_{tr} = \left(\Omega \alpha_N^2 l^2\right) U_N. \tag{2.14}$$

An estimate for U_{tr} may be obtained from Robert's relation [116]:

$$\frac{\partial E}{\partial I} \mid_{\text{fixed } \Gamma \& \text{ vol.}} = U_{tr}, \tag{2.15}$$

which for the slug model (2.7-2.9) results in:

$$U_{tr} = \frac{U_p}{2}. \tag{2.16}$$

Note that similar results has been reported by other researchers using different approaches. Therefore, equation (2.14) can be transformed using (2.16) to

$$U_p = 2\left(\Omega \alpha_N^2 l^2\right) U_N. \tag{2.17}$$

Our approach here is to calculate the corresponding parameter α_N of the resulting Norbury vortex and solve for the corresponding nondimensional stroke length, L/D. The final stage is governed by the main invariants of motion for axisymmetric flows. These are the kinetic energy, the total circulation, and the impulse. Equating these quantities for the slug model (2.7-2.9) with the corresponding quantities in the Norbury vortices (2.11-2.13) and using (2.17), we obtain

$$\frac{L}{D} = \sqrt{\frac{\pi}{2}} \frac{I_N^{1/2} \Gamma_N^{3/2}}{E_N} = f(\alpha_N), \tag{2.18}$$

$$\frac{L}{D} = \sqrt{\frac{\pi}{2}} \frac{\Gamma_N^{3/2}}{U_N I_N^{1/2}} = g(\alpha_N), \tag{2.19}$$

$$E_N = U_N I_N. \tag{2.20}$$

According to Norbury [101] the right-hand side of equations (2.18-2.20) are only a function of α_N. The nondimensional stroke length L/D from equations (2.18) and (2.19), as function of α_N, are shown in figure 2.2. Their intersection yields the parameter α_N of the resulting Norbury vortex. The corresponding stroke length L/D for the resulting Norbury vortex is thus approximately equal to 3. Finally, note that α_N can also be calculated from (2.20), which yields the same value as predicted from figure 2.2. This consistency is in fact a manifestation of the existing relation (equation 2.15) between the invariants of motion for

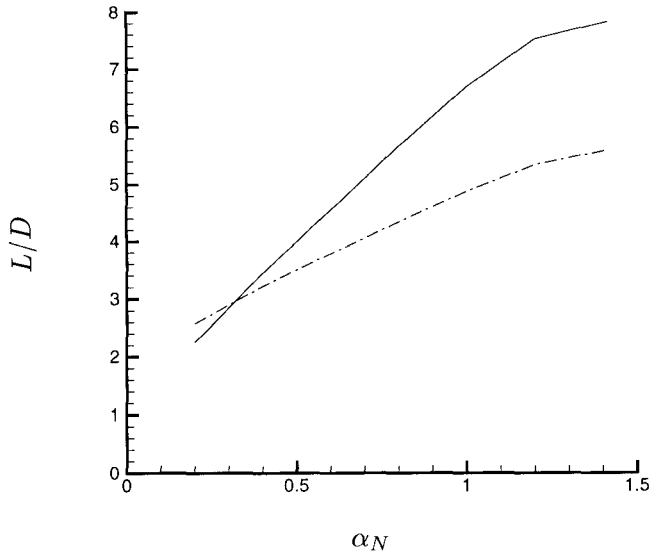

Figure 2.2 Relation between the formation number (L/D) and the parameter of Norbury's family of vortices (α_N). —— equation (2.18); — - — equation (2.19).

axisymmetric flows, which for the slug model is represented by equation (2.17).

Equations (2.18) and (2.19) may also be derived using dimensional analysis. This will also show that these are the only independent relations involved in the prediction of pinch-off process. We assume that the variables involved in the pinch-off process are L/D, U_p (or equivalently U_{tr}, which is obviously related to U_p by (2.15) and (2.16)), and the invariants of motion E, Γ, I. Therefore, we can write:

$$\frac{L}{D} = f(E, \Gamma, I, U_p). \tag{2.21}$$

A straightforward dimensional analysis reveals that the limiting L/D only depends on the nondimensional energy E_{nd} and circulation Γ_{nd} defined as follows:

$$E_{nd} = \frac{E}{\Gamma^{3/2} I^{1/2}}, \tag{2.22}$$

$$\Gamma_{nd} = \frac{\Gamma}{I^{1/3} U_p^{2/3}}. \tag{2.23}$$

The nondimensional energy E_{nd} has already been defined in [44] and used in [46] in the pinch-off process. Γ_{nd} is another nondimensional number for pinch-off process with a universal value. In the next section we will estimate a narrow range for these nondimensional numbers based on our model. Equating the nondimensional energy and circulation between the slug model and the Norbury vortices and using (2.7-2.9), (2.11-2.13), (2.16) and (2.17) result in equation (2.18) and (2.19). Therefore, there are only two independent curves in figure 2.2, where their intersection gives the formation number associated with the pinch-off process.

In the case of time varying exit diameter or piston velocity, the invariants of motion for any exit velocity history $U(t)$ and radius $R(t)$ can be calculated by integrating equations (2.3-2.2) in time. The nondimensional energy is given by

$$E_{nd} = \sqrt{2\pi} \frac{\int R^2 U^3 dt}{\left(\int R^2 U^2 dt\right)^{1/2} \left(\int U^2 dt\right)^{3/2}} \tag{2.24}$$

and the nondimensional circulation is derived as

$$\Gamma_{nd} = \frac{1}{(2\pi)^{1/3}} \frac{\int U^2 dt}{\bar{U} \left(\int R^2 U^2 dt\right)^{1/3}} \tag{2.25}$$

The translational velocity can again be approximated by the Roberts formula [116]

$$\frac{\partial E}{\partial I} \Big|_{\text{fixed } \Gamma \& \text{ vol.}} = \frac{\bar{U}}{2}. \tag{2.26}$$

By removing circulation , $\Gamma = \int U^2 dt$, between these equations we obtain

$$\bar{U} E_{nd} \Gamma_{nd}^{3/2} = \frac{\int R^2 U^3 dt}{\int R^2 U^2 dt} \tag{2.27}$$

Now since $dx = U dt$, and $dV = \pi \int R^2 dx$ we obtain

$$\bar{U} E_{nd} \Gamma_{nd}^{3/2} = \frac{\int U^2 dV}{\int U \, dV} = \frac{2E}{I} \tag{2.28}$$

These relations clearly show that one can modify the values of E_{nd} and Γ_{nd} by a time varying piston velocity or time varying exit diameter. These ideas are numerically verified

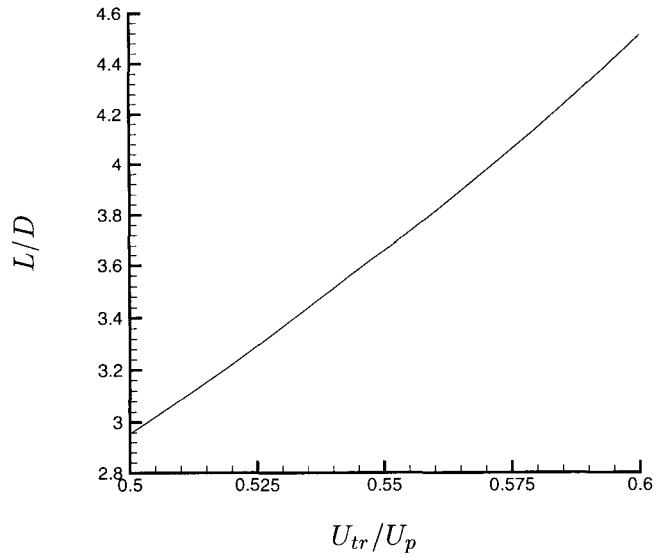

Figure 2.3 Variation of formation number (L/D) with nondimensional translation velocity (U_{tr}/U_p).

in chapter 4.

Note that in practice the translation velocity of real vortex rings is greater than $U_p/2$ (which is what the slug model with constant diameter predicts). However, due to the development of boundary layer at the edge of the cylinder, the effective diameter of the nozzle exit gradually decreases (due to increase in the momentum thickness), thus the mass conservation for constant piston velocity results in an increase in the average exit velocity of the slug of fluid. Therefore, the translational velocity of resulting ring increases above $U_p/2$. This situation can be modeled more effectively by a slug model with gradual decrease in the exit diameter (due to increase in momentum thickness at the edge of the cylinder) to obtain a vortex ring translational velocity more than $U_p/2$. If we repeat the calculations leading to equation (2.19), with U_{tr} varying between $0.5U_p$ and $0.6U_p$, we obtain $3.0 \lesssim \frac{L}{D} \lesssim 4.5$ (see figure 2.3). This range of stroke length for the pinch-off process is consistent with the values observed in the experiments by Gharib *et al.* [46].

2.3 Comments

The fact that the value of α_N corresponding to the pinch-off process is much smaller than $\sqrt{2}$ (Hill's vortex) is an indication of the limitations of the simple cylinder-piston mechanism in producing a very thick vortex ring. In fact, careful examination of figures 2.2 and 2.3 suggests that to produce a Hill's like vortex ring one needs a vortex generator that can deliver more energy compared to the simple cylinder-piston mechanism with the same circulation and impulse. One design could be based on a cylinder with a time varying exit diameter or time varying piston velocity. These designs for generating very strong vortex rings are investigated in section 4.5.

The fact that the pinch-off parameters are independent of the constant piston velocity reveals that the universal time scale of vortex formation does not depend strongly on the value of the piston's impulsive velocity, and was experimentally confirmed in [46]. On the other hand, it is expected that the velocity profile at the cylinder outlet may have a large effect on the final stage, and on the formation number (see chapter 4). This can be manifested as large variations of the invariants of motion to variations in the velocity profile at the cylinder outlet. This variation of the formation time scale with the exit velocity profile has also been observed in experiments by Gharib *et al.* [46].

As experimentally observed by Gharib *et al.* [46] there is a limiting value of E_{nd} around 0.33. The value predicted for E_{nd} in our model is $0.4 \gtrsim E_{nd} \gtrsim 0.27$ for U_{tr} varying between $0.5U_p$ and $0.6U_p$ (see figure 2.2), which is in good agreement with the experimental result. Furthermore, Gharib *et al.* [46] showed that for each experimental setup there is a maximum achievable circulation for the leading vortex for various L/D. Here we suggest that if we nondimensionalize the circulation as suggested by equation (2.23), all of the circulation curves in [46] fall into a single curve that shows a maximum achievable circulation for the leading vortex. Using our analytical model we predict that this limiting nondimensional circulation Γ_{nd} (calculated based on U_{tr}) falls in the range $1.77 \lesssim \Gamma_{nd} \lesssim 2.07$, which indicates that steady vortex rings with higher Γ_{nd} cannot be generated by a simple cylinder-piston mechanism. We have calculated this quantity for the leading pinched off vortex in the set of experiment by Gharib *et al.* [46] and found that it is indeed a constant, namely $\Gamma_{nd} \approx 1.75 \pm 0.05$.

Finally we would like to note that other mechanisms for vortex generation can be analyzed with our method if approximations for the invariants of motion E, Γ, I can be established. An example of this is the numerical generation of a vortex ring by a nonconservative force, as considered in chapter 4.

Chapter 3

Statistical Equilibrium Theory

It is well known that the evolution of the two-dimensional plane turbulence is dominated by the formation of coherent vortices [11, 78]. The formation of coherent structures in freely decaying two-dimensional flows eventually results in a quasi-steady state. The velocity field becomes increasingly dominated by the larger spatial scales as time progresses, and the like-signed vortex regions merge into increasingly larger vortices [78]. Many numerical and experimental studies suggest that the formation of large scale structures is mainly an inviscid process, and that viscosity and dissipation only affect the fine scale motion. This leads to the idea of using statistical mechanics for two-dimensional incompressible inviscid flows to understand these long-lasting structures.

Aside from the kinetic energy, the distinctive feature of both two-dimensional (2D) and axisymmetric turbulence in inviscid flows is the existence of an infinite number of invariants of motion: moments of vorticity. Kinetic energy and enstrophy (the only quadratic constants of motion) are conserved by the nonlinear interactions, whereas in the 3-D case only the former is conserved. Correspondingly, in the 3D case there is only one type of cascade, the energy cascade, which takes place locally from low to high wave numbers. By analogy with the direct energy cascade in three dimensions, Batchelor [8] and Kraichnan [60] conjectured the existence of an enstrophy cascade to the small scales in two-dimensional flows. This result implies that in the 2D case there are two cascade processes: energy cascade to larger scales and enstrophy cascade to smaller scales. The inverse energy cascade to large scales explains a physical mechanism behind the formation of coherent structures in 2D and

axisymmetric turbulence.

The well known enstrophy decay during mixing [78] is in apparent contradiction with the conservation of enstrophy for 2D Euler equations. We will discuss this issue in section 3.3 where we show that on a coarse grain only the linear functionals of vorticity are conserved during the equilibrium process.

The first insight into these problems was provided by Onsager's statistical theory of point vortices [105], later extended by Joyce and Montgomery [58]. For high enough Reynolds numbers, the enstrophy can decay significantly while the energy is decaying by a negligible amount. Prediction of this selective decay process was one of the main successes of point vortex theories. However, the main criticisms of point vortex models are that the infinite conservation laws of vorticity integrals of the Euler equations are not respected, that the quantitative prediction depends on the representation of a continuous vorticity field in terms of point vortices, which is not unique, and that the maximum vorticity is not bounded by the initial maximum, as it should be for 2D flows.

Miller *et al.* [81, 82] and Robert and Sommeria [115] independently developed a mean field theory that removes these limitations. The predicted statistical equilibrium appears to be a particular solution of the Euler equations with fine-scale vorticity fluctuations superimposed. The resulting equilibrium state can be calculated by maximizing a mixing entropy constrained by the invariants of motion, which are the energy, impulse and the global probability distribution of the vorticity fluctuations. It is desirable that the resulting mean field theory will be applicable to high Reynolds number flows as well as inviscid flows. A main criteria for the validity of this approach in predicting the long term behavior of viscous flows is that the relaxation time for the system must be shorter than the viscous time scale. When this condition is satisfied the system relaxes to an almost equilibrium state, before the viscous effects alter the integral of higher moments of vorticity.

In this chapter we are mainly concerned with axisymmetric inviscid flows. Although axisymmetricity is a limitation, a wide range of challenging problems reside in this category, including jet flows, vortex rings, drops, and pipe flows. What makes axisymmetric flows interesting is the existence of a geometrical stretching term in the vorticity equation, which is missing in 2D flows. Our approach is set in the conceptual framework of Hamiltonian

structure of ideal flows (*e.g.*, see [73]). In models for ideal fluids the Hamiltonian form is basic, and has received a great deal of attention in the last thirty years. Hamiltonian phenomenology provides a unifying framework for ideal fluids, provides simplification on many problems, and its existence is essential for developing a complete statistical equilibrium model for fluids.

Our objectives in this chapter are several. Following Szeri and Holmes [134], in §3.1 we derive an explicit expression for a canonical Poisson bracket of axisymmetric flows which is similar to the Poisson bracket of the 2-D plane case. This Poisson bracket satisfies the Jacobi identity (among other properties), and therefore, makes the space of functions of vorticity density fields on Ω (the volume occupied by the fluid) into a Lie algebra. In §3.2 our goal is to ask whether we can predict and explain the long-time evolution of flows, such as those mentioned above, without explicitly using dynamics. Costly dynamical simulations and significant errors at long times make such a theory very attractive for investigating problems where the transient dynamics are not of primary interest. In §3.3 we show that Kelvin's energy variational result can be deduced from the statistical equilibrium equations. The Hamiltonian structure of the vortex filament method for axisymmetric flows is considered in the appendix B. Finally some comments on other aspects of the theory are presented.

3.1 Governing Equations and Poisson Bracket

In this section we study the Hamiltonian structure of axisymmetric flows. It is not obvious how to develop a statistical mechanics theory without a Hamiltonian. Once the Hamiltonian is given, no choice in the development of the theory remains.

Consider an axisymmetric, inviscid homogeneous and incompressible flow in a three-dimensional axisymmetric region Ω (see figure 3.1). The velocity $\boldsymbol{u}(u_r, 0, u_x)$ of this flow is governed by the Euler equations

$$\boldsymbol{u}_t + (\boldsymbol{u} \cdot \nabla)\boldsymbol{u} = -\nabla p, \tag{3.1}$$

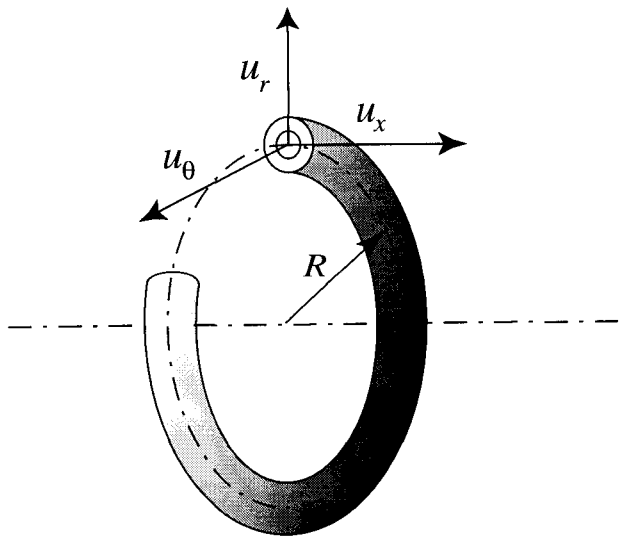

Figure 3.1 A vortex ring in axisymmetric flows.

where p is pressure, with the continuity equation

$$\nabla \cdot \boldsymbol{u} = 0, \tag{3.2}$$

and boundary condition: $\boldsymbol{u}$ tangent to $\partial\Omega$. Taking curl of the equation (3.1) results in the vorticity evolution equation:

$$\frac{\partial \omega}{\partial t} + u_x \frac{\partial \omega}{\partial x} + u_r \frac{\partial \omega}{\partial r} = \frac{u_r \omega}{r}. \tag{3.3}$$

where the scalar

$$\omega = (\nabla \times \boldsymbol{u})_\phi = \frac{\partial u_r}{\partial x} - \frac{\partial u_x}{\partial r}, \tag{3.4}$$

is the azimuthal component of vorticity. The $u_r\omega/r$ term on the right-hand side of the vorticity equation (3.3) is the geometrical vortex stretching. This term is absent in the two-dimensional vorticity equation in Cartesian coordinates.

Now, the governing system consists of a transport equation (3.3) coupled with the elliptic

system (3.2, and 3.4). We would like to use a formulation in terms of the "vorticity density" ξ defined as $\xi = \frac{\omega}{r}$. Consequently, the vorticity equation (3.3) can be written as

$$\frac{\partial \xi}{\partial t} + u_x \frac{\partial \xi}{\partial x} + u_r \frac{\partial \xi}{\partial r} = 0. \tag{3.5}$$

At any instant, the velocity field can be described by the Stokes stream function ψ defined by

$$u_x = \frac{1}{r}\frac{\partial \psi}{\partial r}; \qquad u_r = -\frac{1}{r}\frac{\partial \psi}{\partial x}.$$

Subsequently from (3.4) we obtain

$$\frac{1}{r}\frac{\partial \psi}{\partial r}\left(\frac{1}{r}\frac{\partial}{\partial r}\right) + \frac{1}{r^2}\frac{\partial^2 \psi}{\partial x^2} = -\xi.$$

Using the transformation $y = \frac{r^2}{2}$, one may recast the final set of equations as

$$\frac{D\xi}{Dt} := \frac{\partial \xi}{\partial t} + \frac{\partial \psi}{\partial y}\frac{\partial \xi}{\partial x} - \frac{\partial \psi}{\partial x}\frac{\partial \xi}{\partial y} = 0, \tag{3.6}$$

and

$$\mathcal{L}(\psi) := \frac{\partial^2 \psi}{\partial y^2} + \frac{1}{2y}\frac{\partial^2 \psi}{\partial x^2} = -\xi. \tag{3.7}$$

A suitable phase space for this system is the space of ξ's defined on the physical space occupied by the fluid. The natural choice for the Hamiltonian is the kinetic energy (with unity density) given by

$$H = \frac{1}{2}\int_{R^3} \boldsymbol{u}^2 dV, \tag{3.8}$$

where $dV = rdrdxd\theta$ represents the volume element. In the case of axisymmetric flows

without swirl, one can write

$$\begin{aligned} H &= \pi \int_{\Omega_r} \left(u_x^2 + u_r^2\right) r\, dx\, dr \\ &= \pi \int_{\Omega_r} \left(u_x \frac{\partial \psi}{\partial r} - u_r \frac{\partial \psi}{\partial x}\right) dx\, dr \\ &= \pi \int_{\Omega_r} \left(\omega\psi + \frac{\partial (u_x \psi)}{\partial r} - \frac{\partial (u_r \psi)}{\partial x}\right) dx dr \\ &= \pi \left\{ \int_{\Omega_r} \omega\psi\, dx dr - \oint \psi\, (u_x dx + u_r dr) \right\} \\ &= \pi \left\{ \int_{\Omega_y} \xi\psi\, dx dy - \oint \psi\, (u_x dx + u_r dr) \right\} \end{aligned} \tag{3.9}$$

where Ω_r is the half space $r \geq 0$, and Ω_y is the half space $y \geq 0$. By appropriate assumptions on the behavior of the flow field near the boundaries we can ignore the second term in (3.9). Therefore, we can write the kinetic energy (also called the excess kinetic energy, *e.g.*, [119]) as

$$H = \pi \int_{\Omega_y} \xi\psi\, d\mu = \pi \int \int \mathcal{M}(\boldsymbol{x}|\boldsymbol{x}')\, \xi(\boldsymbol{x})\, \xi(\boldsymbol{x}')\, d\mu\, d\mu', \tag{3.10}$$

where $\boldsymbol{x} = x\mathrm{i}_x + y\mathrm{i}_y$, $d\mu = dx\, dy$ is the area element in Ω_y, and the kernel $\mathcal{M}(\boldsymbol{x}|\boldsymbol{x}')$ is defined by [62]

$$\mathcal{M}(\boldsymbol{x}|\boldsymbol{x}') = \frac{\sqrt{yy'}}{2\pi} \int_0^{2\pi} \frac{\cos\theta\, d\theta}{\sqrt{(x-x')^2 + 2y + 2y' - 4\sqrt{yy'}cos\theta}}. \tag{3.11}$$

Using standard transformations $\mathcal{M}(\boldsymbol{x}|\boldsymbol{x}')$ can be written as

$$\mathcal{M}(\boldsymbol{x}|\boldsymbol{x}') = \frac{(4yy')^{\frac{1}{2}}}{2\pi} \left\{ \left(\frac{2}{k} - k\right) K(k) - \frac{2}{k} E(k) \right\}, \tag{3.12}$$

where k is given by

$$k^2 = \frac{8\sqrt{yy'}}{(x-x')^2 + \left(\sqrt{2y} + \sqrt{2y'}\right)^2},$$

and K and E are the complete elliptic integrals of the first and the second types, respec-

tively [2]. Clearly the kinetic energy is conserved by the flow. The functional derivative of the Hamiltonian (3.10) with respect to ξ is

$$\frac{\delta H}{\delta \xi} = 2\pi \int \mathcal{M}(\boldsymbol{x}|\boldsymbol{x}')\, \xi(\boldsymbol{x}')\, d\mu'. \tag{3.13}$$

Now, we define the Lie-Poisson bracket

$$\{F, G\} = \int \xi(\mathbf{x}) \left\{ \frac{\delta F}{\delta \xi}, \frac{\delta G}{\delta \xi} \right\}_{xy} d\mu, \tag{3.14}$$

where $\{f, g\}_{xy} = \dfrac{\partial f}{\partial x}\dfrac{\partial g}{\partial y} - \dfrac{\partial g}{\partial x}\dfrac{\partial f}{\partial y}$ is the canonical (x, y)-Poisson bracket. One may use (3.13) and (3.14) to show that

$$\xi_t = \{\xi, H\}, \tag{3.15}$$

which is another form of the vorticity density evolution equation. It is not known whether there exists a pair of canonical coordinates (functionals of ξ) which diagonalize the bracket (3.14). However, what is required in statistical equilibrium theory is an invariant measure on the phase space, which will be provided by Liouvill's theorem. Therefore, neither the existence of the canonical coordinate nor the existence of the Lie-Poisson bracket (3.14) is required in the statistical equilibrium theory. The dynamics of the Euler equations preserves phase space volumes, *i.e.*, the flow in the phase space is incompressible. The ergodic hypothesis ascribes weights in proportion to phase space volume. Therefore, the phase space flow preserves relative probabilities in the chosen variables. It also follows that the new radial variable y is necessary to compensate for the geometrical increase in the volume element of the x-r space; $dx\, dy = r\, dx\, dr$. Finally, we would like to note that similar results have been obtained by Szeri and Holmes [134] in considering the nonlinear stability of axisymmetric swirling flows.

The Hamiltonian structure of axisymmetric vortex filaments has been known for more than a century, see [125] and references there in. The Hamiltonian formalism of vortex filaments can be considered as a special case of the field Hamiltonian formalism of this section. Derivation of vortex filament Hamiltonian from the field Hamiltonian is carried

out in the appendix B.

Arnold [4] showed that the Euler equations are geodesic equations on a group of volume-preserving diffeomorphisms with the metric defined by the kinetic energy. He then introduced a powerful version of the Liapunov stability method based on the Casimirs of the Hamiltonian theory [6, 5]. Equation (3.6) implies that there are an infinite number of conserved vorticity integrals, $\int_{\eta(t)} f(\xi)\, d\mu$, for any path $\eta(t)$ moving with the fluid where f is an arbitrary function. Therefore,

$$I_f = \int_{\Omega_y} f(\xi(\boldsymbol{x}))\, d\mu \tag{3.16}$$

defines an infinite number of conserved quantities for the Euler equation (3.6) which can be characterized by

$$I_n = \int_{\Omega_y} \xi^n\, d\mu. \tag{3.17}$$

These conserved quantities are Casimirs, and by Noether's theorem they can be deduced through the invariance of the Euler equation (3.6) under the group of volume-preserving diffeomorphisms $Diff_V(\Omega_y)$. Note that these conserved quantities are in involution with respect to the Poisson bracket (3.14), *i.e.*, $\{I_f, I_{f'}\} = 0$ for any two functional of the form (3.17). Furthermore, substitution of I_f and H into equation (3.14) and integration by parts yields

$$\{I_f, H\} = 0,$$

i.e., any vorticity density integral commutes with the Hamiltonian. Finally, one can verify that the linear momentum

$$P = \frac{1}{2}\int (\boldsymbol{x} \times \boldsymbol{\omega})_x\, \hat{\theta}\, dV = 2\pi \int_{\Omega_y} \xi\, y\, d\mu \tag{3.18}$$

is also an invariant of motion.

The Poisson bracket (3.14) that we have derived for axisymmetric ideal flows is similar to the canonical Poisson bracket of the 2-D plane flows (*e.g.*, [74]). It satisfies the Jacobi

identity (inherited from that for $\{,\}_{xy}$, as is generally the case for Lie-Poisson brackets), among other properties. Therefore, Ω_y is a Lie algebra. One might expect to obtain the same results by a reduction process [74, 73] from the 3D Euler equations with axial symmetry. Now that the Hamiltonian formalism for axisymmetric flows is established, we can proceed with our development of statistical mechanics of vorticity fields.

3.2 Statistical Equilibrium Theory

The equilibrium description of two-dimensional plane inviscid flows was first suggested by Onsager [105] for point vortices. However, this covers only a limited subset of practical vorticity distributions, and approximating a continuous distribution of vorticity with point vortices is a subtle problem. While in practice one must be able to assign any value to the integral of any finite power of vorticity, in Onsager's theory one is limited to the integral of powers of the delta function. This limitation can be removed by the statistical theory presented here.

The statistical mechanics of a continuous vorticity field for 2-D plane flows has been recently developed independently by two groups: Miller, Weichman, and Cross [81, 82] and Robert and Sommeria [115]. Miller *et al.* [81, 82] take a physical approach and offer many insights into the statistical nature of two-dimensional flows. They present two derivations of the mean-field equations. The first derivation [81] is combinatorial and relies on the weakness of the divergence in the Coulomb-type interaction between vortices at small distances. In the second derivation the Kac-Hubbard-Stratanovitch transformation is used to convert the long-range coulomb interaction into purely local square-gradient interaction. Robert and Sommeria's approach [115], on the other hand, is more mathematical. They work in an extended phase space, namely the space of Young measures, which is naturally constrained by the invariants of motion of the system. By using the modern large deviation theory, a thermodynamic limit in this framework is then calculated. Recently Weichman & Petrich [158] successfully extended the same method to predict the statistical equilibrium of shallow water equations.

The theory put forward by these two groups successfully predicts the long time behavior

of two-dimensional incompressible ideal flows. When the vorticity concentrations on intermediate scales are the dominant part of the total vorticity field, the traditional concept of transfer of enstrophy to smaller scales and transfer of energy to larger scales is suppressed (*e.g.*, computations by [78]). The lifetimes of the resulting coherent vortices are much longer than the eddy turn-over time for the turbulent field. Many experimental and computational studies show that the final equilibrium state only decays on a viscous time scale.

Our intention in this section is to derive the statistical equilibrium equations for axisymmetric flows. In doing so we assume ergodicity, *i.e.*, that the dynamics of the flow samples all of the phase space consistent with the conservation laws. The treatment we describe is to cast the problem as a variational problem with conservation constraints. The maximization of an entropy functional will then result in the equations for statistical equilibrium of the flow.

The governing equations are given by (3.6) and (3.7), and the conserved quantities are H, P, and the infinite series I_n. The conservation of P results from the absence of global pressure forces in the x-direction. Note that H and I_n are conserved in the general case for any domain Ω. By contrast the conservation of the physical momentum P is specific to a given geometry.

The scalar vorticity is not advected passively by the flow, but is coupled to its motion through the elliptic equation (3.7). The strong fluctuations of the stream function caused by this coupling will mix the vorticity at small scales and stimulate the appearance of coherent structures at larger scales. In the axisymmetric Euler equation (3.6), the vorticity density ξ is a material property. This implies that the total area fraction occupied by each vorticity density level σ is conserved. We call this quantity the global probability distribution of vorticity density $\gamma(\sigma)$. The distribution function $n_0(\boldsymbol{x}, \sigma)$ is defined as the local (but coarse-grained) probability of finding the vorticity level σ in an $\boldsymbol{x}$-neighborhood. Therefore, $n_0(\boldsymbol{x}, \sigma)$ may be considered as the local density of the vorticity density with strength σ. This distribution function satisfies the normalization condition

$$\int n_0(\boldsymbol{x}, \sigma)\, d\sigma = 1. \tag{3.19}$$

Subsequently (3.17) may be recast as the conservation of

$$\gamma(\sigma) = \int n_0(\boldsymbol{x}, \sigma)\, d\mu = \int \delta\left(\sigma - \xi(\boldsymbol{x})\right) d\mu. \tag{3.20}$$

Physically $\gamma(\sigma)$ measures the fractional area covered by the vorticity level σ.

What makes this theory more desirable than the point vortex models is the conservation of $\gamma(\sigma)$, *i.e.*, conservation of all moments of vorticity density. Now the coarse-grained (macroscopic) equilibrium vorticity density $\overline{\xi}(\boldsymbol{x})$ is defined as

$$\overline{\xi}(\boldsymbol{x}) = \int n_0(\boldsymbol{x}, \sigma)\, \sigma\, d\sigma. \tag{3.21}$$

The coarse-grained equilibrium stream function $\overline{\psi}$ is related to $\overline{\xi}$ through equation (3.7). Note that the macrostate has fluctuations in vorticity density, but as $\overline{\psi}$ is obtained by an integration of vorticity density, there are no fluctuations in the stream function. For a system with very small viscosity, we expect that these fluctuations will be smoothed out, so that the resulting steady flow becomes the actual final state of the system.

Finally the entropy is defined by

$$S = -\int n_0(\boldsymbol{x}, \sigma) \ln n_0(\boldsymbol{x}, \sigma)\, d\sigma d\mu. \tag{3.22}$$

Now the standard methods of statistical mechanics can be used. We started by a Hamiltonian system which gives the dynamics of a great number of particles and which is the microscopic level of description of the system. Then, at a macroscopic level, we consider some relevant means, which we call macroscopic observables. To these two levels of description we associate an entropy functional using Boltzmann's formula $S = k \log W$, where W is the volume occupied in the phase space (endowed with the invariant Liouville measure) by the set of all the microstates giving the same macrostate. Maximizing the entropy functional then gives the equilibrium states. The entropy functional in equation (3.22) represents the logarithm of the number of possible vorticity configurations associated with a final macrostate.

The equilibrium state is obtained by maximizing the mixing entropy (3.22) subjected to

the constraints of motion (3.17-3.18) and the normalization condition (3.19). We write these constraints in terms of the locally averaged vorticity density $\overline{\xi}$ and the associated stream function $\overline{\psi}$. The resulting constrained variational problem can be treated by introducing the Lagrange multipliers such that the first variations satisfy

$$\delta S - \beta \delta H - \beta \int \alpha(\sigma)\, \delta\gamma(\sigma)\, d\sigma - \int \zeta(\boldsymbol{x})\, \delta \left(\int n_0 d\sigma \right) d\mu - \beta U\, \delta P = 0, \tag{3.23}$$

where β is the inverse of the temperature, $\alpha(\sigma)$ is the chemical potential of species σ, and U is the translation velocity. In general, energy or temperature may be considered as an indicator of how closely the vorticity is packed (we will come back to this point later). The final state can be considered either as a critical point of the entropy for any admissible perturbations (that satisfies the invariants of motion) or equivalently, as a critical point of the free energy F [14]:

$$F = S - \beta H - \beta \int \alpha(\sigma)\, \gamma(\sigma)\, d\sigma - \iint \zeta(\boldsymbol{x})\, n_0\, d\sigma\, d\mu - \beta U P. \tag{3.24}$$

The resulting distribution function is a Gibbs state of the form

$$n_0(\boldsymbol{x}, \sigma) = e^{-\beta\left[2\pi\sigma\left(\overline{\psi}+yU\right)+\alpha(\sigma)\right]-1-\zeta}. \tag{3.25}$$

Using the normalization constraint (3.19) we can remove the Lagrange multiplier ζ to obtain

$$n_0(\boldsymbol{x}, \sigma) = \frac{e^{-\beta\left[2\pi\sigma\left(\overline{\psi}+yU\right)+\alpha(\sigma)\right]}}{\int e^{-\beta\left[2\pi\sigma\left(\overline{\psi}+yU\right)+\alpha(\sigma)\right]} d\sigma}. \tag{3.26}$$

A differential equation for $\overline{\psi}$ may be obtained by multiplying both sides of (3.26) by σ and integrating:

$$\mathcal{L}(\overline{\psi}) = -\overline{\xi} = -\frac{\int \sigma\, e^{-\beta\left[2\pi\sigma\left(\overline{\psi}+yU\right)+\alpha(\sigma)\right]} d\sigma}{\int e^{-\beta\left[2\pi\sigma\left(\overline{\psi}+yU\right)+\alpha(\sigma)\right]} d\sigma}. \tag{3.27}$$

This can be written as

$$\mathcal{L}(\overline{\psi}) := \frac{\partial^2 \overline{\psi}}{\partial y^2} + \frac{1}{2y}\frac{\partial^2 \overline{\psi}}{\partial x^2} = \frac{1}{2\pi\beta}\frac{d}{d\overline{\psi}} \ln \mathcal{Z}, \tag{3.28}$$

where the partition function $\mathcal{Z}$ is given by

$$\mathcal{Z}(\overline{\psi}) = \int e^{-\beta\left[2\pi\sigma\left(\overline{\psi}+yU\right)+\alpha(\sigma)\right]}\, d\sigma. \tag{3.29}$$

The partition function relates the properties of the microscopic system. It provides all the statistical parameters of a macroscopic system. The Lagrange multipliers β, U, and functions $\alpha(\sigma)$ are determined by the global conservation of vorticity density,

$$\gamma = \int \frac{e^{-\beta\left[2\pi\sigma\left(\overline{\psi}+yU\right)+\alpha(\sigma)\right]}}{\mathcal{Z}(\overline{\psi}(\boldsymbol{x}))}\, d\mu, \tag{3.30}$$

by fixing the energy E,

$$E = -\pi \int \overline{\psi}\, \mathcal{L}(\overline{\psi})\, d\mu, \tag{3.31}$$

and by conservation of linear momentum P,

$$P = -2\pi \int y\, \mathcal{L}(\overline{\psi})\, d\mu. \tag{3.32}$$

Note that by an argument similar to the one in [115], one can easily show that the fine scale vorticity density fluctuations are of higher order and do not contribute to the energy.

In analogy to statistical thermodynamics, $\alpha(\sigma)$ is called the chemical potential of species σ, and β is the inverse of temperature [105]. The energy or temperature is an indicator of how closely the vorticity is packed. Knowing the invariants of motion and the Lagrange multipliers, Z will be only a function of $\overline{\psi}$, and therefore, equation (3.28) will be of the form $\mathcal{L}(\overline{\psi}) = f(\overline{\psi})$.

The equilibrium states are not steady in general but translate uniformly with velocity U. In the case of nonvanishing circulation, we can change the frame of reference to the one moving with the center of vorticity density, where $P = 0$. The stream function in this case

is obviously $\psi + yU$.

3.3 Kelvin's Variational Result

A general variational principle due to Arnold [4, 7] characterizes steady flows in an ideal fluid as constrained extremal for the kinetic energy functional defined on an appropriate class of competing vortices. For two dimensional flows the underlying variational principle was known to Kelvin [59]. Kelvin [59] pointed out that a variational principle exists for the steady motion of vortices and the steady states are given by stationary values of the kinetic energy for given linear and angular hydrodynamic impulse and circulation, with respect to kinematically allowable perturbations. Kelvin states the principle without proof as being obvious to him (see sections 4 and 18 of [59]). A proof of a similar variational principle was provided after almost a century by Benjamin [9]. While Arnold's principle is based upon the so-called isovortical variations, Benjamin prefers to prescribe the functional relation between vorticity and stream function instead. Conceptually, these variational results lead to a formulation of the general mathematical problem entirely in terms of the natural physical invariants associated with the equations governing vortex dynamics – namely energy, impulse and circulation. Note that Benjamin [9] used his variational method to show the existence of steady solutions to axisymmetric Euler equations. A one-parameter family of such solutions was presented by Norbury [101]. One might expect that a similar approach can be used to show the existence of a mean field in statistical equilibrium theory.

In this section we show that the equilibrium solution predicted from the statistical equilibrium theory (entropy maximization) satisfies an energy extremization similar to Kelvin's approach, *i.e.*, the final mean field profiles satisfy a constrained energy maximization problem similar to the one in [59].

The input to the statistical theory is the initial vorticity density distribution $\xi(\boldsymbol{x})$, or equivalently all the invariants of motion, H, P, and $\gamma(\sigma)$. However, in most practical applications (*e.g.*, the Red Spot of Jupiter and vortex ring pinch-off process [89]) our information on the initial condition is very limited. What is usually measurable is the finite resolution vorticity distribution $\overline{\xi}(\boldsymbol{x})$. Here we follow the approach of Miller *et al.* [82]. Therefore,

the only measurable distribution function is the dressed distribution function (as defined for the two dimensional case in [82])

$$\gamma_d(\sigma) = \int \delta(\sigma - \overline{\xi})\, d\mu. \tag{3.33}$$

Here, $\gamma(\sigma)$ is the initial distribution function and $\gamma_d(\sigma)$ is the distribution function observed on any finite length scale. Note that $\overline{\xi}(\boldsymbol{x})$ is a smooth function except for $\beta \to \pm\infty$ and that in general the vorticity distribution function $\gamma_d(\sigma)$ derived from the mean field profile $\overline{\xi}$ is not the same as $\gamma(\sigma)$. In the process of statistical equilibrium, when going from the microscopic description to the macroscopic description, it is natural that a major part of the information about the details of the small scales be lost. Therefore, the vorticity density conservation laws (3.17), except for the total circulation I_1, are all violated on the macroscopic scale. No other moment of the vorticity is necessarily the same for both γ and γ_d. In this process only the energy, circulation and impulse are conserved both on the fine scales and on the coarse scales. Although it is impossible to experimentally infer $\gamma(\sigma)$ from the equilibrium state alone, one can make partial predictions by knowing $\gamma_d(\sigma)$. In two-dimensional Euler or high Reynolds number Navier-Stokes equations, it is well-known that there is an inverse cascade of energy to large scales and a forward cascade of enstrophy (second integral of vorticity, I_2) to smaller scales. Therefore, by measurement of finite resolution one might expect to recover almost all of the initial kinetic energy of the system, while the conservation of enstrophy will be violated.

Following Miller *et al.* [82], a *dressed vorticity density corollary* is in order: $\overline{\xi}(\boldsymbol{x})$, the averaged vorticity density field, is the maximum energy solution (corresponding to $T \to 0^-$ or $\beta \to -\infty$) of the statistical equilibrium equations with constraint function $\gamma_d(\sigma)$. For the maximum energy solution, $\gamma_d(\sigma) = \gamma(\sigma)$. The proof is omitted here, since it is analogous to the proof for a similar corollary in two-dimensional turbulence in the plane [82]. Although γ_d is in general different from γ, a consequence of the above argument is that at a given energy, γ_d results in the same equilibrium solution as γ. Furthermore, the given energy turns out to be precisely the maximum energy compatible with γ_d.

The other implication of the dressed vorticity corollary is that for a fluid in statistical

equilibrium, coarse-grained quantities suffice to determine the equilibrium. This observation suggests that our equilibria might persist in the presence of a viscosity acting to smear the small scales. An equivalent way of stating this result is that the long-time dynamics of an inviscid fluid will evolve to a configuration which is a global extremum of the energy, subject to satisfying the long-time (dressed) vorticity distribution.

Note that the total circulation I_1 is preserved during the equilibrium process, *i.e.*,

$$\int \sigma\, \gamma(\sigma)\, d\sigma = \int \sigma\, \gamma_d(\sigma)\, d\sigma. \tag{3.34}$$

Therefore, one can say that for a system with fixed circulation and impulse the statistical equilibrium state is the one that maximizes the energy consistent with the $\gamma_d(\sigma)$, *i.e.*, isovortical perturbations. This is analogous to the Kelvin's variational principle which states that in an incompressible inviscid flow with fixed circulation and impulse the steady solution maximizes the energy for isovortical perturbations. The connection between statistical equilibrium and the equilibrium solutions of steady Euler equations are clear in this argument. Note that the higher moments of vorticity are not explicitly specified in Kelvin's variational principle (in contrast to Arnold's approach [7]). Since the energy, circulation and impulse of the system are preserved during the equilibrium process, the final solution of the statistical equilibrium theory satisfies the requirement of Kelvin's variational principle. This result is valid both in the Cartesian coordinates considered in [82, 115] and in the axisymmetric coordinates described in this chapter.

3.4 Discussion

In this chapter a statistical mechanical theory for describing the equilibrium state of axisymmetric Euler equations was derived. The resulting solutions of the statistical equilibrium theory are in fact the equilibrium solutions to the axisymmetric Euler equations, stabilized by the infinite invariants of motion. All the invariants of motion are accounted for, and an exact set of nonlinear mean field equations are derived for the vorticity density profile. We observed that while the infinite number of Casimirs were crucial in developing the theory, integrals of the nonlinear powers of vorticity density measured on any physical scale will

not be the same as in the initial state. The only apparent conserved quantities are energy, impulse, and total circulations. This is similar to previous results in two dimensional plane flows. These are the quantities specified in Kelvin's variational result. Through a dressed vorticity density corollary the connection between the statistical equilibrium state and Kelvin's variational principle was considered. The only inputs to the statistical equilibrium theory are the values of the invariants of motion, which can be derived from the initial conditions. Other than the value of these invariants, the equilibrium state is independent of the initial condition or the details of its subsequent evolution.

It is known that the Euler equations or the high Reynolds number Navier-Stokes equations have filamentation properties due to mixing effects. A deterministic description of such flows would require rapidly increasing amount of information as time goes on. The excessive spatial information requires very high resolution. This problem can be remedied by solving the mean field equations for macroscopic quantities (coarse-grained) where all the microscopic fluctuations (fine-grained) are smoothed out. Consequently, solving the nonlinear differential equation (3.28) requires much less resolution than solving the time evolving Euler equations, since the fine scale vorticity structures have already been filtered out by statistical averaging. In brief, to find the equilibrium state of a system it is cheaper to numerically integrate the mean field equation (3.28) than the Euler equations (3.1-3.2) or (3.7).

In a real system there is always at least a small amount of damping due to viscosity [157]. If the physical system is very large, it might be possible for this damping to eliminate all the small scale fluctuations required for ergodicity. Therefore, the system might freeze in an intermediate state before having the chance to sample the entire phase space. In other words, the mixing only occurs in a confined region of space. For the statistical equilibrium theory to be valid, the effective relaxation time toward the final microcanonical distribution must be less than the viscous diffusion time, otherwise the physical viscosity can alter the invariants of motion and cause changes in the final state. It is to be expected that for some special configurations of large systems, global ergodicity will not be achieved, and that thermal equilibrium is therefore reached in a local region, where vorticity remains trapped and well stirred inside a bubble. Since the relaxation process is driven by fine-

scale vorticity fluctuations, it may happen that these fluctuations vanish (*e.g.*, by viscous effects) before the system reaches its global equilibrium. However, in such cases the idea of 'vorticity localization' [16] or the 'maximum-entropy bubble' [14] could be used to explain stable multiple vortex states. This idea has already been proven to be effective for two-dimensional plane turbulence [15, 14].

When the flow under consideration has more invariants of motion, all of them should be accounted for. Each invariant introduces a new Lagrange multiplier. A typical case for axisymmetric flows is the conservation of angular momentum for flows in a rotating frame of reference.

Our motivation for the study of long time behavior of axisymmetric flows comes from our attempt to understand the universal formation number of vortex ring pinch-off process observed by Gharib *et al.* [46]. This formation number is the time that the vortex ring pinches off from its generating axisymmetric jet. Here we refer to the nondimensional stroke length L/D as the formation number, where L is the piston's stroke length and D is the exit diameter. Inspired by the statistical equilibrium theory we have formulated an analytical model that predicts this universal time scale (see Mohseni & Gharib [89] and chapter 2). In this case our goal is to predict and explain the longtime behavior of such systems without resorting to dynamics. It was both experimentally and analytically [46, 89] observed that the limiting stroke L/D occurs when the generating apparatus is no longer able to deliver energy, circulation and impulse at a rate comparable with the requirement that a steadily translating vortex ring has maximum energy with respect to kinematically allowable perturbations. We expect that a similar result can be obtained through an entropy maximization problem. The physical explanation is that for short stroke length the system relaxes to a steadily translating vortex ring. Increasing the stroke length results into a larger vortex ring. Note that any vorticity generation mechanism has its own specific rate of energy, circulation and impulse generation. For a cylinder piston mechanism these rates are given in [89]. For high stroke lengths the traditional cylinder piston mechanism is not able to provide energy compatible with an equilibrium state at that circulation and impulse. Consequently, for very high stroke length the system relaxes to a periodic array of vortex rings. To generate vortex rings with higher nondimensional circulations, one needs to alter

the rate of delivery of invariants of motion. For a cylinder piston mechanism, Mohseni & Gharib [89] proposed a time varying exit diameter, that was later verified numerically [88]. Numerical experiments on this problem will be the topics of a future paper.

The field statistical theory of two-dimensional Euler equations in Cartesian coordinates can be considered as the generalization of the statistical theory of point vortices to continuous vorticity distributions. In this respect, the Lundgren and Pointin point vortex mean field theory [71], and the Kraichnan energy-enstrophy theory [61] were rederived as special limiting cases (see, *e.g.*, [82, 157] for details). Therefore, we expect that a similar result will be valid between the field theory of axisymmetric flows of this chapter and the resulting statistical theory of axisymmetric vortex filaments. In this respect connections at the microscopic level of description are presented in the appendix B.

Chapter 4

Numerical Results

In this chapter a numerical study of vortex formation process is performed. We would like to acknowledge collaboration with Mr. H. Ran on performing some of the numerical computations presented in this chapter (see also Mohseni *et al.* [91]).

According to the pinch-off process model presented in chapter 2, the formation number is only a function of the translational velocity of the vortex ring, U_{tr}, vortex ring diameter, D, and several invariants (in the inviscid case) of the motion E, Γ and I. Where E is the kinetic energy, Γ the circulation, and I the impulse. We equate these invariants of motion for a model of the discharge process (slug-model) and a model for the leading vortex ring (a vortex in the Norbury family) to obtain an estimate for the formation number. Alternatively, one can use dimensional analysis to achieve the same result. An implicit relation between the involved quantities can be represented as

$$\frac{tU_{tr}}{D} = f(E, \Gamma, I, U_{tr}). \tag{4.1}$$

An estimate for U_{tr} may be obtained from [116] formula

$$U_{tr} = \frac{\partial E}{\partial I} \Big|_{\text{fixed } \Gamma \& \text{ vol.}}, \tag{4.2}$$

which for a slug model results in (see [89]):

$$U_{tr} = \frac{U_p}{2}. \tag{4.3}$$

For a slug of fluid $L = tU_p$, we obtain

$$\frac{L}{D} = 2\frac{tU_{tr}}{D}. \tag{4.4}$$

This is a relation between the stroke ratio for a cylinder-piston mechanism and the formation number based on the properties of the resulting vortex ring. While L/D is specific to vortex generation by cylinder-piston mechanism, tU_{tr}/D is a more general parameter in terms of measurable vortex quantities.

It is believed that the pinch-off process is a generic vortex phenomenon, that can be observed in other vortex formation mechanisms, including vortex generation by nonconservative forcing considered in this paper. For these other formation mechanisms characterization of the pinch-off process in terms of the stroke-length is not appropriate. Here we recast the formation number into a "pinch-off time," t_{po}, which is that time after the force is turned on when the leading vortex ring has achieved maximum circulation (and will later become disconnected from the trailing jet). A straightforward dimensional analysis on the functional relation (4.1) results in three nondimensional parameters, related by

$$t_{nd} = f(E_{nd}, \Gamma_{nd}) \tag{4.5}$$

where

$$t_{nd} = \frac{t_{po}U_{tr}}{D} \qquad E_{nd} = \frac{E}{\Gamma^{3/2}I^{1/2}}, \qquad \Gamma_{nd} = \frac{\Gamma}{I^{1/3}U_{tr}^{2/3}}. \tag{4.6}$$

E_{nd} is the same nondimensional energy defined in GRS, while Γ_{nd} is a new normalized circulation introduced in Mohseni and Gharib [89]. Experiments by GRS and computations by Rosenfeld *et al.* [117] have shown that vortex ring generators with different stroke length, orifice diameters, piston velocities, and orifice geometries all lead to similar formation numbers, so long as the velocity profile leaving the orifice is nearly uniform. Gharib *et al.* [46] measured values of E_{nd} around 0.33, and Mohseni and Gharib [89] predicted that E_{nd} should fall in the range of 0.27 and 0.4, and that Γ_{nd} should fall in the range of 1.77 and 2.07.

Numerically, there are several ways to simulate this process. A given vorticity distribution and its corresponding velocity field may be used as the initial condition (*e.g.*, Stanaway, *et al.* [129]). This method is usually restricted to simple vorticity distributions (Gaussian or uniform core distribution), and a differential equation must be solved numerically to determine the corresponding pressure field. Another method is to prescribe an axial velocity profile $U_z(r)$ at an inlet, in an attempt to model the injection of fluid through the nozzle of the experimental apparatus (*e.g.*, Verzicco, *et al.* [154]). This approach was also used in recent computations by Rosenfeld *et al.* [117], who investigated formation for long discharge times with a number of different geometrical configurations and piston velocity programs. Their numerical results largely confirm the previous experiments of GRS, showing that the formation time is insensitive to the details of the formation process, including the piston velocity and its variation in time, details of the geometry of the generator, and the Reynolds number. They also found that the velocity profile of the discharged fluid can be an important factor in determining the formation number. For example, if a very long cylinder is used, the velocity profile at the discharge will be parabolic (assuming laminar flow), and the formation number is smaller than the "universal" value by a factor of 4.

A simpler method of numerically generating vortex rings is to apply a nonconservative force directly in the equations of motion. In laboratory, nonconservative force, *i.e.*, rotational force can be generated by imposing currents in the fluid with a magnetic field. McCormack and Crane [76] discussed vortex ring generation by an impulsive force applied over a circular area. In numerical simulation of the interaction between a vortex ring and a solid wall, Swearingen *et al.* [133] used an impulsive body force applied over a circular region of fluid to generate a vortex ring with the desired properties.

We have used a similar force distribution, but have studied forces with longer duration. Thus long duration forces are used to simulate the formation of vortex rings in the laboratory. Our main objective is to verify the theoretical predictions [89], and establish the relation between laboratory methods of vortex ring generation and those generated with applied nonconservative forces. The results largely confirm the experimental results of GRS, and the computations of Rosenfeld *et al.* [117]. Rosenfeld *et al.* showed that in addition to the universality of the formation time, the circulation of the leading vortex ring, when

scaled with the average piston velocity and cylinder diameter, varied by only 40% as the formation conditions were varied. Here we show that under similar conditions this variation is, in fact, very much smaller, around 5%, if the vortex circulation is normalized with the impulse of the ring and its translation velocity, as defined in Mohseni and Gharib [89]. We also investigate the extent to which thicker rings (with relatively higher nondimensional circulations) can be formed.

This chapter is organized as follows. In section 4.1 we analyze the form of the nonconservative force and the invariants of the resulting vortex ring. In section 4.2 we briefly describe the numerical method which is used for the computations. We also discuss how properties of the leading vortex ring (such as impulse, energy and circulation) are computed. In section 4.3 we present two approaches in describing the pinch-off process. The results of the numerical experiments are presented in section 4.4. Two ways of generating thick (strong) vortex rings are discussed in section 4.5, where we compare the results with vortices of the Norbury family. Concluding remarks are placed in section 4.7.

4.1 Vorticity Generation by Nonconservative Force

Vortex rings are generated by a nonconservative force added to the momentum equation. Cylindrical-polar axisymmetric coordinates (r,x) are used. The body force is aligned with x, and has the form:

$$f_x(r,x,t) = C\ F(t)\ G(x)\ H(r) \tag{4.7}$$

where C is an amplitude constant with units of circulation, and F, G are functions with units of inverse time and inverse length, respectively, and H is nondimensional function. For impulsive forces, $F(t)$ is a regularized Dirac delta function (a Gaussian):

$$F(t) = \frac{e^{-\left(\frac{t-t_0}{\alpha_t}\right)^2}}{\alpha_t\sqrt{\pi}}, \tag{4.8}$$

and for long duration forces, a regularized step-function:

$$F(t) = -\frac{\tanh\left(\alpha_t(t_0 - t)\right) + \tanh\left(\alpha_t(t - t_0 - T)\right)}{2T} \tag{4.9}$$

where in both cases α_t is a time scale which controls the smoothing. For the nonimpulsive case, T is the duration of the applied force.

The functions G and H control the vorticity distribution generated by the force. For the axial distribution, we again use a regularized delta function:

$$G(x) = \frac{\sqrt{\alpha}}{\alpha_x\sqrt{\pi}}\, e^{-\alpha(\frac{x}{\alpha_x})^2} \tag{4.10}$$

while for the radial distribution, we use:

$$H(r) = \frac{1}{2}\, erfc\big(\sqrt{\alpha}\,\frac{r - R}{\alpha_r}\big) \tag{4.11}$$

where, as shown below, R is the nominal toroidal radius of an impulsively generated ring, and α_r and α_x are length scales which control the smoothing, and α is a purely numerical nondimensional constant discussed below. For impulsive forces, the azimuthal vorticity field generated by the force is given, to leading order (*e.g.*, [118]), by:

$$\omega_\theta(x, r) = -\frac{\partial f_x(x, r)}{\partial r}. \tag{4.12}$$

Thus for impulsive forces, the vorticity field is approximately a two-dimensional Gaussian distribution (for small α_r):

$$\omega_\theta = \frac{C\alpha}{\pi\alpha_x\alpha_r}\, e^{-\alpha\left((\frac{r-R}{\alpha_r})^2 + (\frac{x}{\alpha_x})^2\right)}, \tag{4.13}$$

which is the rationale for the functional dependence chosen for H and G. Weigand & Gharib [159] showed that vortex rings generated by a piston/cylinder arrangement possessed a Gaussian vorticity distribution in their core. Note that the constant factor $\alpha = 1.25643\cdots$ is used so that the maximum tangential velocity in the core is located at $r = R \pm \alpha_r$. Thus α_r is also the core radius.

The circulation for the impulsive case is then given by (integrating equation (4.13) over the area):

$$\Gamma = C \qquad \text{impulsive force.} \tag{4.14}$$

A variety of length and time scales are available for nondimensionalization of various quantities associated with vortex ring generation. In what follows, we choose the (nominal) ring radius, R as the basic length scale, and use this with the amplitude of the force (with units of circulation), C, to form time and velocity scales. Thus we have the following 4 nondimensional parameters associated with the forcing: α_r/R, α_x/R, TC/R^2, and $\mathrm{Re} = C/\nu$.

Note that C is only the circulation of the vortex ring when the forcing is impulsive. For nonimpulsive forces there is a maximum forcing time beyond which a leading vortex ring pinches off from a trailing jet. Thus for nonimpulsive forces the Reynolds number based on $\frac{C}{\nu}$ is not the most appropriate Reynolds number to describe the leading vortex ring. For such cases we define an additional Reynolds number:

$$\mathrm{Re}_{l.v.r.} = \frac{\Gamma_{l.v.r.}}{\nu} \qquad \text{nonimpulsive force.} \tag{4.15}$$

where $\Gamma_{l.v.r.}$ is the (measured) circulation of the leading vortex ring. In most of the cases, Reynolds number defined by $\Gamma_{l.v.r.}$ is greater than 1500.

4.2 Numerical Method

For practical reasons, an existing code for the axisymmetric compressible Navier-Stokes equations has been used to study vortex ring formation. The code was initially developed to investigate the acoustics of turbulent vortex rings and jets. While the numerical method is inefficient for computing low Mach number flows, the CPU requirements for the present problem are minimal and all the computations were performed on a small workstation. In the cases presented here, the maximum Mach number in the flow was 0.2, and it was verified that changes in Mach number below this value had no impact on the results presented.

A sixth order compact finite difference scheme [64] is used in both the axial and radial

directions, and an explicit fourth-order Runge-Kutta method is used for time advancement. At the boundary we use the buffer zone proposed by Freund [41] to absorb the waves. To avoid problems with the polar coordinate singularity, the centerline treatment proposed by Mohseni and colonius [88] is used in combination with symmetry relations for axisymmetric flows. From the location of the applied force, the computational domain extends to $-3R$ and $21R$ in the axial directions and about $4R$ in the radial direction. The grid spacing is $\frac{1}{25}R$, and the time step is $\frac{1}{25}R/a$ where a is the sound speed. Cases with higher time and spatial resolutions established the independence of the solution on the resolution.

For the results presented in the next section, we need to calculate the kinetic energy, impulse, and circulation:

$$E = \pi \int \omega\psi dxdr, \qquad I = \pi \int \omega r^2 dxdr, \qquad \Gamma = \int \omega dxdr, \tag{4.16}$$

respectively, of the leading vortex ring. To compute the integrals, the velocity field from the computations is differentiated to obtain the vorticity. In order to distinguish between the leading vortex ring and the rest of the vorticity, we set the vorticity to zero outside of a closed iso-contour of vorticity around the leading vortex core, at which point the vorticity is 2% of the maximum vorticity in the core. Then an integral equation [118] is used to obtain the stream function, ψ, from the vorticity distribution, and equations (4.16) are integrated numerically with a 4th-order accurate quadrature scheme. The translational velocity, U_{tr}, is estimated by tracking the position of the maximum vorticity in the leading vortex core.

To estimate the uncertainty in determining E_{nd} and Γ_{nd} from the computational data in this way, we set up a Hill's spherical vortex ring in the domain, computed the integrals in (4.16) and compared them with theoretical results. Obviously, the accuracy depends on how well the boundary of the vortex ring can be resolved by the grids. With grid spacing $\frac{1}{25}R$, where R is the radius of the Hill's Vortex, and the error in calculating Γ, E, I is 0.5%, 4%, 6% respectively.

Another uncertainty in determining E_{nd} and Γ_{nd} comes from the cutoff level. As mentioned above, for all cases, we use 2% of the maximum vorticity in the core. The optimal cutoff level should be the minimum contour level that distinguishes between the leading

vortex ring and the rest of the vorticity, which is varying with time and Reynolds number. We compared the values of E_{nd} and Γ_{nd} of the leading vortex ring, computed with 2% cutoff level, with values computed with the optimal cutoff level for several cases. The difference is less then 2% for E_{nd} and 1% for Γ_{nd}.

4.3 Vortex Ring Pinch-off Process

Vortex rings are generally the final outcome of the evolution of cylindrical vortex layers (shear layers). In the laboratory, a common method of generating a vortex ring is by using the so called cylinder-piston mechanism. In this method a slug of fluid is pushed through an orifice or nozzle, which creates a sharp shear layer. This shear layer is intrinsically unstable and rolls up into a spiral structure. The resulting vortex ring is fed by the shear layer at a specific rate (velocity), which is the velocity of the shear layer. The rate with which the invariants of motion (in an inviscid case, E, Γ, I) are delivered is essential in determining the properties of the resulting leading vortex ring. This rate is in fact a main characteristic of the vortex generator and varies among different vortex generation tools.

We offer two explanations for the pinch-off process. The first one describes the process as a dynamical problem, where we focus on the transitional dynamics of the leading vortex ring and its following shear layer. In the second approach we consider the phenomenon as the relaxation process of the leading ring to its final equilibrium state.

Dynamical approach: Here we describe the evolution of the leading vortex ring and the trailing shear layer in the early stages of formation. The vorticity distribution is plotted in figure 4.1 at three different times for a typical pinch-off case. At the earliest time 46.8, which is nearing the end of the forcing time, the velocity profile at the axial center of the forcing region, $x = 3$ in the figure, resembles the velocity profile at the exit of a nozzle. At $x = 5.8$, the location of maximum vorticity at time 46.8, the axial velocity profile has two local peaks. The upper maximum corresponds to the maximum axial velocity of the leading vortex ring. The lower peak corresponds to the maximum velocity in the shear layer. Since the vortex has been enlarged significantly at this stage, it pushes the shear layer toward the axis of symmetry. This is evident by the shifting of the maximum axial velocity in the

shear layer toward the axis of symmetry. Since the leading vortex ring gains its strength from the shear layer, it ceases to grow if the local velocity of the shear layer is less than the velocity of the vortex at that location. We believe that this instant characterizes the pinch-off time. At time 122.7, the leading vortex is almost separated from the tail, and is in transition to absorb the remains of the tail-vorticity into its core. At a later time, 217.6, the leading vortex spreads more, leading to a decrease in its axial velocity. This trend is illustrated in the vorticity profiles as well. The thin shear layer rolls up into a highly peaked vorticity region that accelerates and moves the shear layer toward the axis of symmetry. At the pinch-off time, the vorticity strength in the shear layer trailing the leading vortex tends to zero at $r = 0$. From this time on, the vortex spreads more toward its final configuration where the vorticity is not highly concentrated.

Therefore, one might conclude that the dynamical criterion for the pinch-off is that the maximum axial velocity in the rings equals the maximum axial velocity of the following shear layer. Alternatively, the pinch-off time is when the shear layer is unable to enlarge the leading vortex ring, the strength of the shear layer tends to zero at $r = 0$.

This approach suggests means to modify the properties of the resulting vortex ring by manipulating the characteristics of the generating shear layer. One way is to gradually move the shear layer away from the symmetry axis, so that the leading vortex ring grows away from the symmetry axis. The other is to gradually increase the velocity of the generating shear layer in order to compensate for the increasing translational velocity of the ring. These are investigated in section 4.5.

Relaxational approach: While the dynamical approach is insightful, it is cumbersome to model. It depends on the nonlinear dynamics of the leading vortex ring and its interaction with the trailing vorticity, and as such relies on obtaining an accurate estimate of the velocity profile in the leading ring and in the trailing shear layer. To overcome this difficulty Mohseni and Gharib [89] proposed a relaxational approach to the pinch-off process. They suggested that in the inviscid case the final state of the problem is governed by the first few invariants of the motion, namely the energy, impulse, and circulation. While there are an infinite number of conserved integrals of motion in an inviscid flow, on a macroscopic level, only the linear functionals of the vorticity density are conserved, which are the energy,

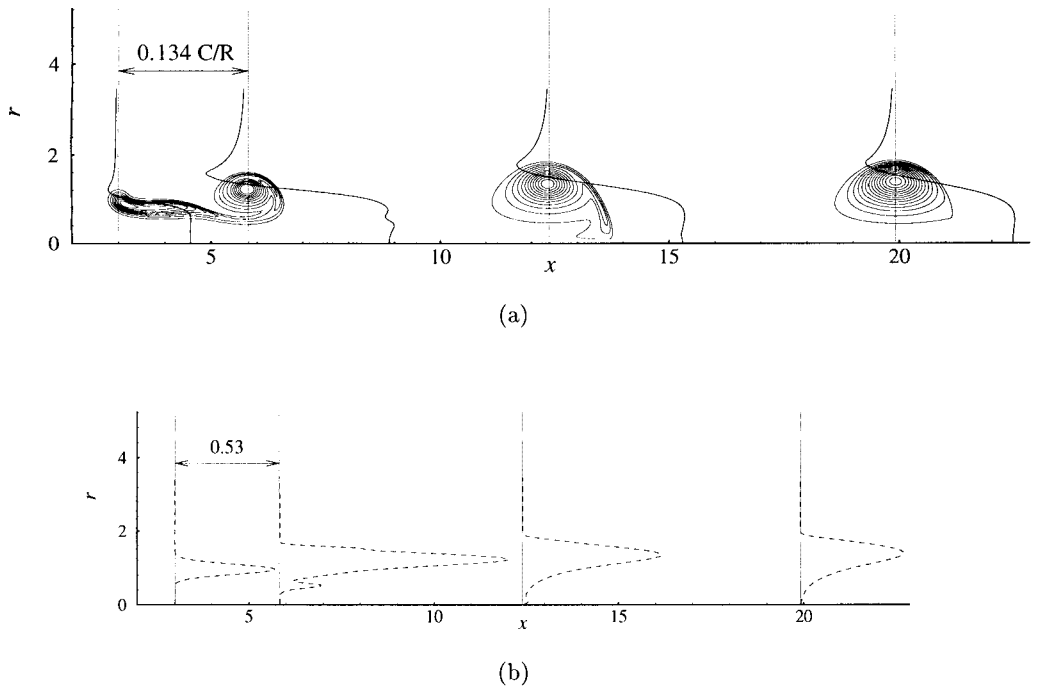

Figure 4.1 (a) Nondimensional vorticity contours ($\omega R^2/C$) and axial velocity (uR/C) profiles, and (b) vorticity profiles at nondimensional times tC/R^2 =46.8, 122.7, and 217.6. (———) axial velocity and (- - - -) azimuthal vorticity. Axial velocity and vorticity distributions at the axial center of the forcing region at the nondimensional time 46.8 is also plotted. The scales for velocity and vorticity profiles are shown in the picture.

impulse, and circulation [85]. These few conserved quantities are the ones considered in the Kelvin variational principle. A straightforward dimensional analysis results in the governing three parameters, nondimensional energy E_{nd} and nondimensional circulation Γ_{nd}, and nondimensional time t_{nd}. The equivalence of the nondimensional energy and circulation for the initial and final state of the fluid results in a prediction for the pinch-off time. The same approach is valid for other mechanisms of shear layer generation as long as an estimate of U_{tr} and toroidal radius of the vortex ring in terms of the known quantities is known a priori. If an estimate for the rate of generation of nondimensional energy and circulation is known, an estimate of the pinch-off time is obtained by the equivalence of these quantities for the

generation mechanism and for the final state. In section 4.5 we investigate how to change the properties of the shear layer generator so that it can provide more energy at the later stages of the formation process compatible with the invariants of motion for thick vortex rings in the Norbury family of vortices.

4.4 Numerical Results

In this section, we present results for vortex ring generation by nonimpulsive forces. This corresponds to long stroke length in vortex generation by a cylinder-piston mechanism. In particular, we wish to establish under what conditions the normalized circulation, Γ_{nd}, and energy, E_{nd}, of the leading vortex rings are independent of the parameters associated with the nonimpulsive forcing.

Vorticity contours at several different stages of the formation process are presented in figure 4.2 for a typical case with $\alpha_r/R = 0.2$, $\alpha_x/R = 0.2$, $TC/R^2 = 25.29$, and $\mathrm{Re} = 3600$. The Reynolds number based on the circulation of the leading vortex ring is $Re_{l.v.r.} = 2800$. In figure 4.2(a), a vortex ring with small core size is generated shortly after the onset of the forcing. As the vortex ring grows in size (figure 4.2(b)), it translates downstream due to its induction velocity. In figure 4.2(c) the spiral structure of the core is well-established, and at the lowest vorticity level depicted in the figure the tail is disconnected from the leading ring.

In figure 4.3, we plot the instantaneous vorticity field for three different values of the force duration at a time when the leading vortex ring has translated about $5\frac{1}{2}$ times the ring diameter. For $TC/R^2 > 9.11$, the leading vortex ring is pinched off from its trailing jet. In case (a), $TC/R^2 = 4.05$, all of the shear layer generated by the nonconservative forcing is absorbed by the leading vortex ring and there is no visible vorticity tail behind the vortex ring. In figure 4.3(b), where $TC/R^2 = 25.3$, the leading vortex ring reaches its final configuration, while a small part of the original shear layer is left behind and not absorbed by the leading vortex. For $TC/R^2 = 77.5$ (figure 4.3(c)), there is a strong trailing jet behind the leading vortex ring. It is important to note that the size of the leading vortex rings are very similar in figures 4.3(b) and (c) and the contour levels are the same. These

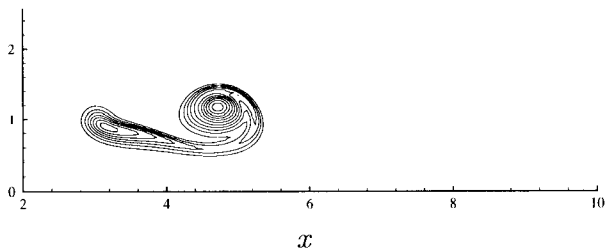

(a)

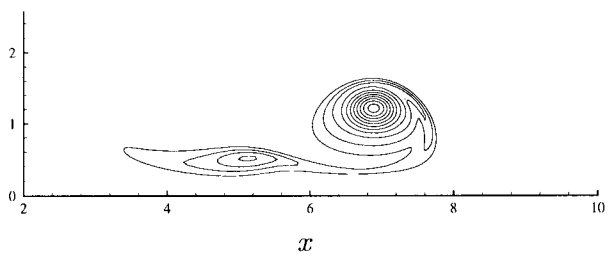

(b)

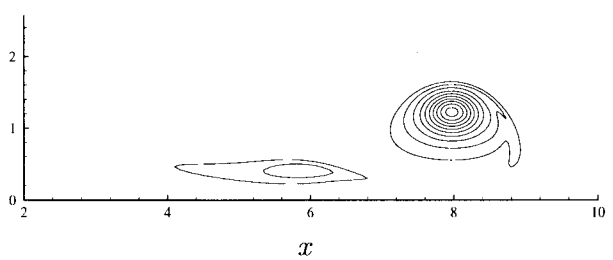

(c)

Figure 4.2 Vortex ring formation at different times; (a) $tC/R^2 = 26.83$, nondimensional vorticity ($\omega R^2/C$) contour levels (min=0.08, max=0.78, increment=0.07) /3.16 (b) $tC/R^2 = 44.72$, contour levels (min=0.05, max=0.65, increment=0.06) /3.16 and (c) $tC/R^2 = 53.66$, contour levels (min=0.06, max=0.66, increment=0.06) /3.16.

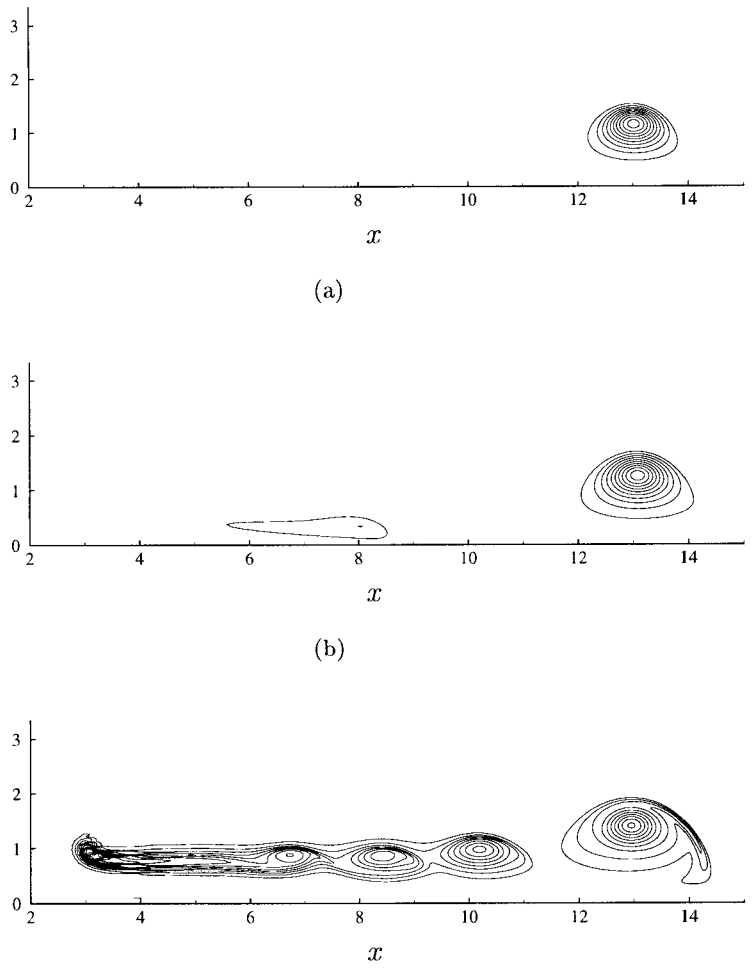

Figure 4.3 Vortex ring formation with different forcing times, (a) $TC/R^2 = 4.05$, contour levels (min=0.002, max=0.02, increment=0.002) (b) $TC/R^2 = 25.3$, contour levels (min=0.0023, max=0.0333, increment=0.0031), and (c) $TC/R^2 = 77.5$, contour levels (min=0.0023, max=0.0333, increment=0.0031).

figures should be compared qualitatively with figure 3 in [46], where a similar pinch-off process is observed in experiments.

In the rest of this section we quantitatively compare the nondimensional circulation and energy of the leading vortex. The total circulation and the circulation of the leading vortex

ring only are presented in figure 4.4. By varying the force duration, it was found that $TC/R^2 = 9.11$ was the critical "formation time" beyond which vorticity produced by the force at later time is not rolled into the leading ring. For $TC/R^2 > 9.11$, the circulation of the leading vortex ring normalized by C, varies between 0.65 and 1.05, and the translational velocity $U_{tr}R/C$ varies between 0.13 and 0.1. In figure 4.5 the nondimensional circulation of the leading vortex rings, Γ_{nd}, is plotted. The total circulation for the case with the critical value of $TC/R^2 = 9.11$ is also presented in figure 4.5. The nondimensional circulation is very close to 2, and varies by only 5 % for all the different forcing times considered. As is evident from the error bars in the figure (see section 4.2), the uncertainty in the measured circulation and translation velocity in the leading vortex ring are greater than the variation between the different cases. The constancy of the final nondimensional circulation indicates that the pinch-off time for all cases is nearly the same, with a value $t_{po}U_{tr}/D$, of 1.2. The nondimensional energy of the leading vortex rings is also very nearly invariant to the force duration, with values near 0.3.

As discussed in section 4.1, there are four independent parameters for the forcing profiles chosen: α_r/R, α_x/R, TC/R^2, and $\mathrm{Re} = C/\nu$. First we consider the effect of the Reynolds number on the vortex formation process, letting $Re_{l.v.r.}$ take on the values of 320, 800, 1890, 3680, and 7300, respectively. With small Reynolds numbers (320 and 800) the rapid decrease in Γ_{nd}, depicted in figure 4.6, shows the effect of viscosity. Note that in these highly viscous cases the vortex ring *is not* separated from its tail at a cut-off level of 2% of the maximum vorticity, resulting in large Γ_{nd} and small E_{nd} compared with the pinched off cases. As is evident in figure 4.6, for Reynolds numbers greater than 1500, the nondimensional circulation of the leading vortex ring is not much affected by the viscosity. It is interesting to note that $\Gamma_{l.v.r.}/\nu$ is also the ratio of viscous diffusion time scale and the relaxation time scale. Therefore, for high Reynolds numbers the fluid system relaxes to its final leading vortex configuration before viscous forces have a significant effect on the final outcome. All of the numerical examples in the rest of this paper are performed at Reynolds numbers above 1500 to minimize the viscous effects on the vortex ring formation process.

In the second set of computations, we change the axial extent of the forcing region, α_x/R. Changing α_x/R results in changes to the translational velocity. The more compact

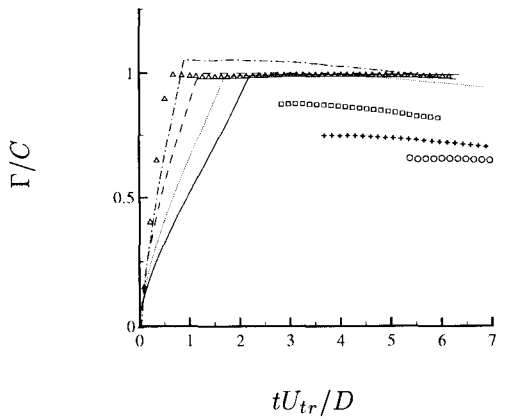

Figure 4.4 Vortex rings generated with $\alpha_x/R = 0.2, \alpha_r/R = 0.2$, and with different forcing duration TC/R^2. Total circulation: (Δ) $TC/R^2 = 4.05$; (—·—) $TC/R^2 = 9.11$; (----) $TC/R^2 = 14.2$; (·····) $TC/R^2 = 25.3$; (——) $TC/R^2 = 39.5$. Ring circulation: ($\Box$) $TC/R^2 = 14.2$; (+) $TC/R^2 = 25.3$; ($\circ$) $TC/R^2 = 39.5$. For cases with forcing time less than the pinch off time, namely $TC/R^2 = 4.05$ and 9.11, the total circulation and the circulation of the leading vortex ring are the same.

the forcing region, the higher the translational velocity. For $TC/R^2 = 25.3$ we obtain $U_{tr}R/C = 33.98, 24.03, 16.99$ for $\alpha_x/R = 0.1, 0.2, 0.4$ respectively. Although the leading vortex ring has higher translational velocity and circulation, if nondimensionalized as in (4.6), the normalized circulation Γ_{nd} is still around 2.0, as plotted in figure 4.7. We can also see that the normalized energy E_{nd} reaches it equilibrium value (≈ 0.29) after time $tU_{tr}/D = 4.0$. This implies that the leading vortex ring has reached the steady state. Therefore, the first time that the vortex generator delivers this amount of normalized circulation and energy, 2.0 and 0.29 respectively, is marked as the pinch-off time. If we stop forcing the flow at this time the final outcome will be a single vortex ring without any trailing vortices. If the forcing continues after this time, a leading vortex ring followed by a trail of vortices will be generated.

Next we change the radial extent of the forcing, α_r/R, while the other forcing parameters

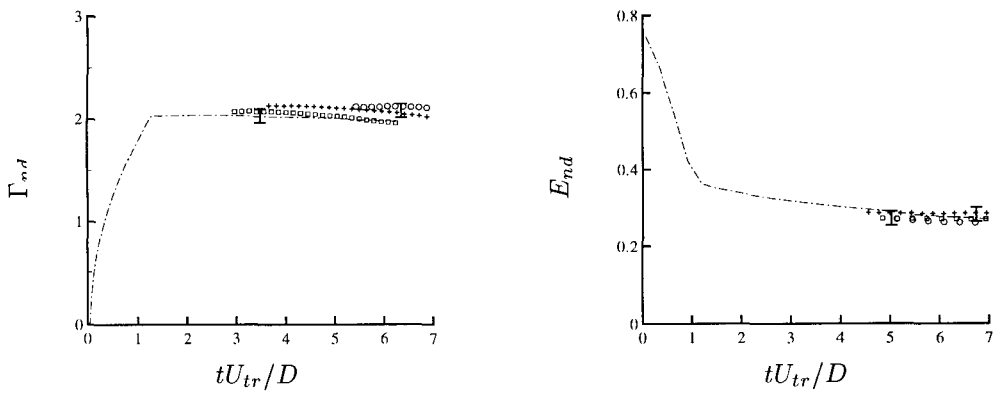

Figure 4.5 Vortex rings generated with $\alpha_x/R = 0.2, \alpha_r/R = 0.2$, and different forcing duration TC/R^2. (—·—) $TC/R^2 = 9.11$; (□) $TC/R^2 = 14.2$; (+) $TC/R^2 = 25.3$; (∘) $TC/R^2 = 39.5$.

are held constant. In physical terms α_r changes the thickness of the shear layer (boundary layer thickness in the cylinder-piston mechanism). For small α_r/R the invariants of motion, *i.e.*, circulation, impulse and energy, are not a strong function of α_r/R. The velocity profile at the forcing location resembles a top hat function in r. For the cases where α_r/R is less than 0.2, the final nondimensional circulation and energy are not affected by variations in α_r/R. The shear layer thickness in most of the experimental cases in [46] is less than 0.2. On the other hand, for large α_r/R the velocity profile at the forcing location spreads in r, which consequently changes the amount of impulse imparted on the fluid due to the action of force. The velocity profile at the forcing location is presented in figure 4.8 for values of α_r/R in the range 0.1 to 0.6. Note that increasing the value of α_r/R will gradually change the velocity profile from being close to a top hat function to a smoother velocity profile. Therefore, by changing α_r/R during the forcing period one can model the boundary layer growth in the shear layer.

The nondimensional circulation and energy are presented in figures 4.8(b) and 4.8(c). Rosenfeld *et al.* [117] considered the effect of the discharge velocity profile on the total circulation in a cylinder-piston mechanism. They pointed out that for constant average

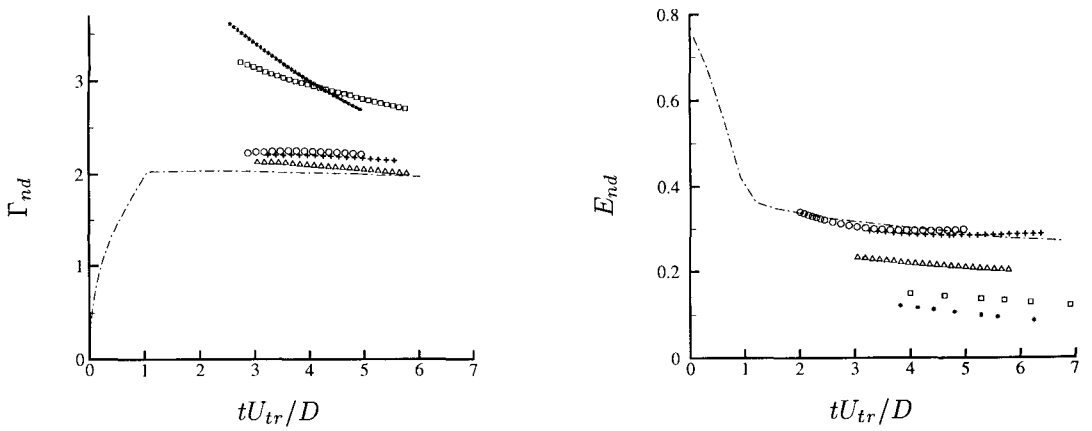

Figure 4.6 Vortex rings generated with $\alpha_x/R = 0.2, \alpha_r/R = 0.2, TC/R^2 = 25.3$, and different Reynolds number. (*) $\mathrm{Re}_{l.v.r.} = 320$; (□) $\mathrm{Re}_{l.v.r.} = 800$; (△) $\mathrm{Re}_{l.v.r.} = 1890$; (+) $\mathrm{Re}_{l.v.r.} = 3680$; (○) $\mathrm{Re}_{l.v.r.} = 7300$. The total quantities with the forcing duration $TC/R^2 = 9.11$ very close to the limiting case is also plotted as (—·—). For $\mathrm{Re}_{l.v.r.} = 320$ and 800 the leading vortex ring is not detached from the trailing jet at a cut-off level of 2% of the maximum vorticity.

piston velocity the circulation generated by a parabolic velocity profile is 4 times larger than the circulation generated by a top hat profile, resulting in a much smaller formation number. One should note that changing the velocity profile has a severe effect on the impulse imparted on the fluid due to the forcing. Figure 4.8 shows that for the present results the average velocity and maximum velocity at the axis of symmetry are nearly the same as the thickness of the shear layer is increased. Therefore, while the rate of generation of circulation in all cases is almost the same, the rate of impulse and energy generation varies significantly. This results in variations in the nondimensional circulation and energy, as shown in figures 4.8(b) and 4.8(c).

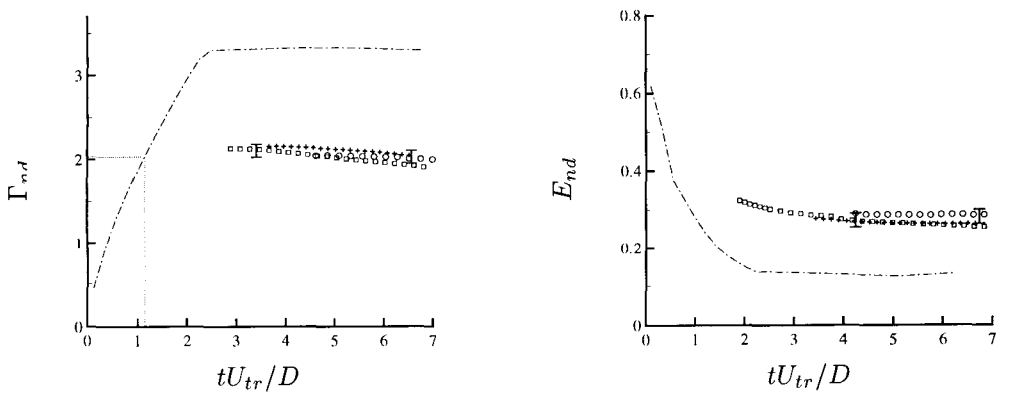

Figure 4.7 Vortex rings generated with $\alpha_r/R = 0.2, TC/R^2 = 25.3$, and different α_x/R. Leading vortex ring: (□) $\alpha_x/R = 0.1$; (+) $\alpha_x/R = 0.2$; (○) $\alpha_x/R = 0.4$. (—·—) total properties provided by the shear layer for $\alpha_x/R = 0.4$.

4.5 Generation of Thick Vortex Rings

Generation of very strong (high circulation) vortex rings is of importance in many fluid applications. An example is synthetic jets (*e.g.*, Glezer *et al.* [128]), where one tries to modify the main flow by imparting strong vortex rings from the boundary. In the experimental set-up described by Gharib *et al.* [46] (using a cylinder-piston mechanism), it was observed that for each L/D there is a limiting circulation for which it is not possible to generate a stronger vortex ring. Mohseni and Gharib [89] suggested that the nondimensionalization based on equations (4.6) results in a universal circulation $\Gamma_{nd} \approx 2$. Therefore, one can conclude that using the conventional cylinder-piston mechanism, it is not possible to generate a vortex ring with higher nondimensional circulation than 2.

In section 4.3 we argued that at the pinch-off moment the maximum axial velocity in the vortex ring equals the velocity of the following shear layer and that the shear layer is forced toward the axis of symmetry where it loses its strength. Therefore, one expects that if we move the shear layer away from the axis of symmetry or gradually increase the speed of the shear layer, it can still feed the leading vortex ring. Hence, we would be able to

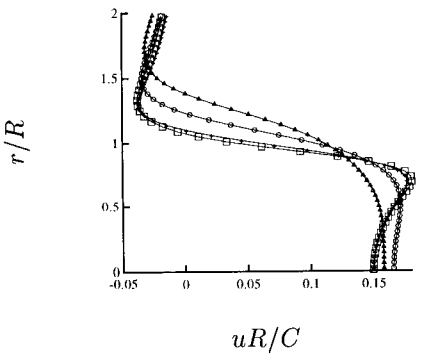

(a)

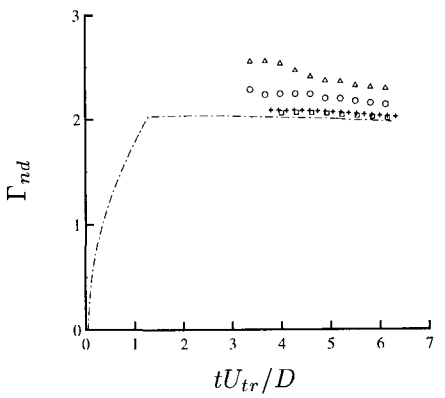

(b)

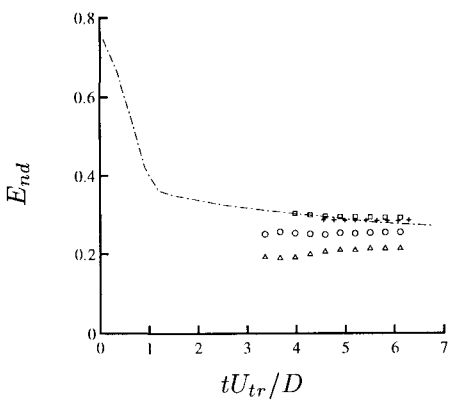

(c)

Figure 4.8 Vortex rings generated with $\alpha_x/R = 0.2, TC/R^2 = 25.3$, and different α_r/R: (a) Velocity profile at time $tU_{tr}/D = 9.11$; (b) Circulation; (c) Energy. (—·—) $TC/R^2 = 9.11$; (Δ) $\alpha_r/R = 0.6$; (o) $\alpha_r/R = 0.4$; (+) $\alpha_r/R = 0.2$; (□) $\alpha_r/R = 0.1$.

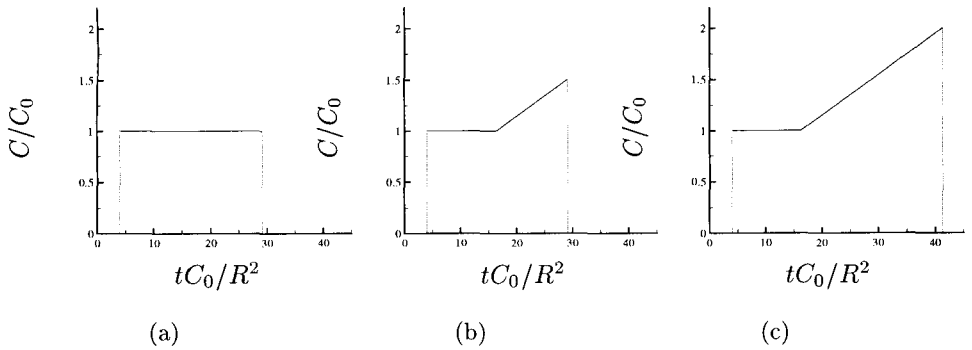

Figure 4.9 Time history of the forcing amplitude for the results in figure 4.10.

generate very strong vortex rings. These ideas are implemented in this section.

In the first set of experiments we gradually increase the amplitude of the forcing, analogous to gradually increasing the piston velocity in the cylinder-piston mechanism, to generate very strong rings. This way, we gradually increase the velocity of the shear layer, in order to compensate for the increasing translational velocity of the leading ring. Therefore more vorticity is fed into the leading ring, resulting in a stronger vortex ring. We consider a case where the amplitude of the forcing function changes linearly with time, see figure 4.9. The nondimensional energy and circulation of the leading vortex ring generated by two cases with variable forcing amplitude are presented in figure 4.10, where they are compared with the result for a constant forcing amplitude. The normalized circulation is $\Gamma_{nd} \approx 2.5$, 25% higher than the case with fixed diameter, and nondimensional energy is $E_{nd} \approx 0.2$, 40% smaller than the fixed diameter case, which suggests that the formed vortex ring has more vorticity than the case with fixed diameter.

Similarly one can gradually increase the radial extent of the forced region during the forcing period. This is similar to having a cylinder-piston mechanism with time-varying exit diameter. This way at later times the shear layer will be released at greater distance from the axis of symmetry, forcing the center of the vortex ring to move away from the symmetry axis. Consequently, while the rate of circulation generation is fixed during this

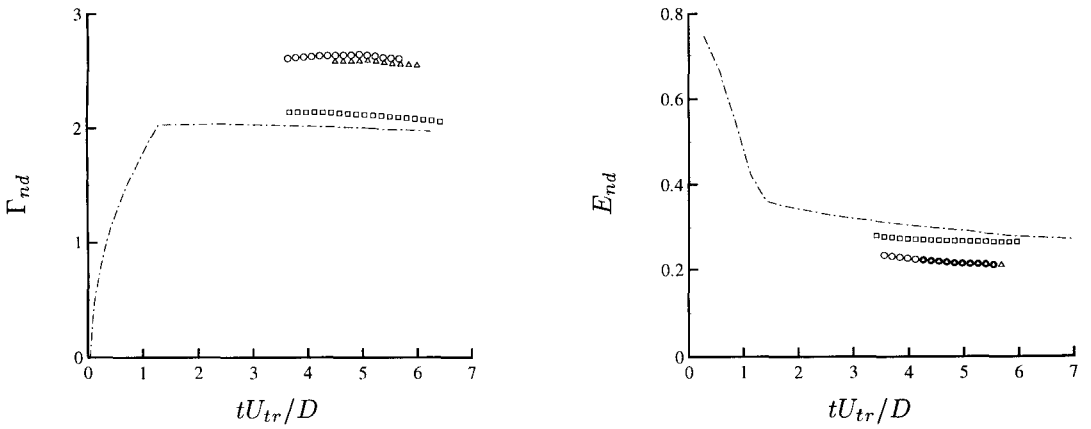

Figure 4.10 Vortex rings generated with varying forcing amplitude. (□) constant forcing amplitude in figure 4.9(a); (○) forcing amplitude depicted in figure 4.9(b); (△) forcing amplitude depicted in figure 4.9(c).

process, the rate of energy and impulse delivery to the vortex ring increases. Therefore, the vortex generator would be capable of providing energy compatible with a vortex in the Norbury's family for higher α_N (α_N, the parameter of the Norbury family of vortices, is the nondimensional mean core radius [101, 89]). The results presented in figure 4.11 are for a linear change of diameter with time as $R/R_0 = 0.0317(tC_0/R^2) + 0.9399$, where the force is applied for $1.9 \leq tC_0/R^2 \leq 0.9399$. It is observed that a very strong vortex ring with high nondimensional circulation and low energy, comparable with similar quantities for Hill's spherical vortex, can be generated.

In both numerical experiments, while no attempt was made to optimize the change in the radial extent of the forcing area or forcing amplitude with time, we were able to generate vortex rings with nondimensional circulation near 2.7 and nondimensional energy of about 0.2, which are very close indeed to the values of these quantities for Hill's spherical vortex, $\Gamma_{nd}^{\text{Hill}} = 2.7$ and $E_{nd}^{\text{Hill}} = 0.16$.

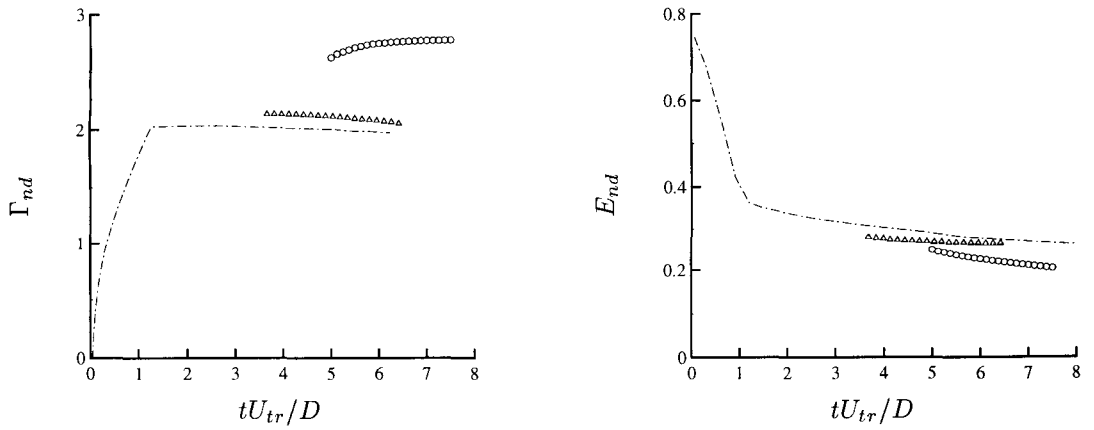

Figure 4.11 Vortex rings generated with varying exit diameter. $\alpha_x/R_0 = \alpha_r/R_0 = 0.2$, and (— · —) constant diameter with $TC/R_0^2 = 9.11$; (△) constant diameter with $TC/R_0^2 = 25.3$; (○) varying diameter with $TC/R_0^2 = 25.3$.

4.6 Comparison with Norbury Vortices

In this section we compare the nondimensional circulation and energy of the leading vortex rings with vortices of the Norbury family. The Norbury vortices are characterized by a single parameter α_N, the nondimensional mean core radius [101]. The parameter α_N varies from zero for vortex rings with zero mean core radius to $\sqrt{2}$ for Hill's spherical vortex. These vortices are steady solutions of the axisymmetric Euler equations, and satisfy the Kelvin variational principle. Although the vorticity distribution for an experimentally or computationally generated vortex ring is quite different from the Norbury vortices, the stream lines are very similar (see [132]).

Mohseni and Gharib [89] suggested that the invariants of motion for the leading vortex ring can be approximated by a vortex in the Norbury family. In this section we examine this assumption. The parameters for all the cases considered are given in table 4.1. The mean core radius for the computationally generated rings is defined by the radius of an equivalent vorticity region relative to the toroidal radius. The primary area of the leading vortex ring

case	TC/R_0^2	α_x/r	α_r/r	$Re_{l.v.r.}$	
1	9.11	0.2	0.2	2770	
2	14.2	0.2	0.2	3200	
3	25.3	0.2	0.2	3800	
4	39.5	0.2	0.2	4100	
5	25.3	0.2	0.2	7300	
6	50.6	0.4	0.2	6300	
7	25.3	0.2	0.4	4000	
8	25.3	0.2	0.6	4000	
9	31.6	0.2	0.2	3000	time varying diameter
10	25.3	0.2	0.2	3300	time varying amplitude

Table 4.1 Parameters for computational cases

depends on the cut-off level in defining the leading vortex ring. However, changing the cut-off level from 1% to 15% of the maximum vorticity, results in at most 6% variation in the mean core radius. Here, all the results are presented for the cut-off level of 2%.

In figure 4.12, we compare the nondimensional energy and circulation of the leading vortex ring with the same quantities for the Norbury family of vortices. It is observed that for all the cases with thin shear layers, namely $\alpha_r/r \lesssim 0.3$, the nondimensional circulation is around 2.1 ± 0.1 and the nondimensional energy is around 0.29 ± 0.04. These values are very close to the values predicted by a vortex in the Norbury family with the same nondimensional mean core radius. For cases like 7 and 8, which have a very thick shear layer that extends to regions close to the axis of symmetry, one obtains slightly thicker rings with higher circulation and lower energy. The strongest vortex rings are generated by the mechanisms proposed in the last section. It is interesting to note, however, that the nondimensional circulation and energy of the leading vortex ring follow closely the behavior of thick vortex rings in the Norbury family, as depicted in figure 4.12.

4.7 Conclusions

Vortex ring formation by long-duration nonconservative forces are considered. We investigate the appropriate form of the impulsive forcing function to generate a vortex ring with

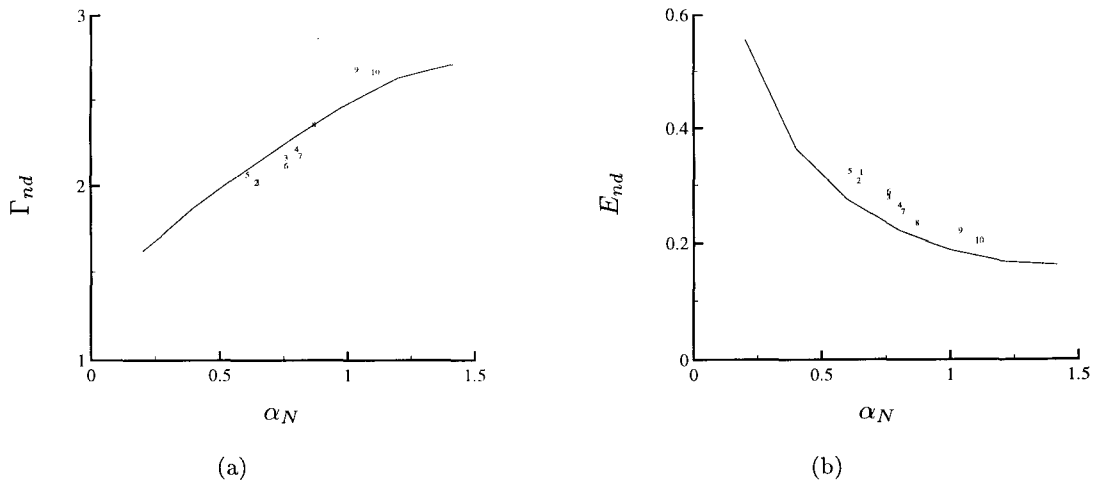

Figure 4.12 Comparison of nondimensional circulation and energy of the computational cases (shown in numbers) with the Norbury family (——).

desired core structure, total circulation, and ring radius.

An investigation of the vortex pinch-off process, as observed in the experiments by Gharib *et al.* [46], is carried out with long duration nonconservative forcing. The invariants of motion are directly computed for the leading vortex ring in order to determine the nondimensional energy and circulation. It is observed that if the rate of generation of the invariants of motion is constant during the forcing period, the leading vortex ring pinches off at around the nondimensional energy of 0.3 and nondimensional circulation of 0.2, consistent with the experimental observation and theoretical prediction [46, 89]. It was suggested that to generate stronger vortex rings with higher nondimensional circulation and lower nondimensional energy, one needs to modify the rate of generation of the integrals of motion during the forcing period. This modification must be consistent with the Norbury family of vortices. The leading vortex ring will pinch-off when the generating mechanism is not capable of providing the energy and circulation at a rate compatible with the Kelvin variational principle for a steadily translating vortex ring.

Two ideas for modifying the properties of the leading vortex ring were successfully

implemented, where we changed the radial extent of the forcing region or the amplitude of the forcing with time to generate very strong vortex rings. The nondimensional energy and circulation of the leading vortex rings were compared with an equivalent vortex in the Norbury family. This favorable agreement verified that the nondimensional energy and circulation of Norbury family of vortices are good approximations for the nondimensional energy and circulation of pinched off vortices.

Chapter 5

Conclusions and Future Work

Vortex rings are fluid structures efficient in transferring coherent packets of momentum, circulation, and impulse across relatively long distances. These properties make vortex rings useful for control strategies in industrial flows, for example, by using synthetic jets [128].

In this investigation we were concerned with finding the maximum circulation and energy that can be delivered to a vortex ring by an apparatus. Our study was motivated by experimental observations by by Gharib *et al.* [46]. In vortex ring generation by a cylinder-piston mechanism, they observed that for a large piston stroke versus diameter ratio (L/D), the generated flow field consists of a leading vortex ring followed by a trailing jet. They observed that for a large range of flow parameters there is a limiting stroke length that imposes an upper bound on the circulation that a vortex ring can acquire. Furthermore, they observed that the maximum circulation is achieved for a narrow range of formation numbers, between 3.6 and 4.5, for a variety of exit diameters and orifice geometries. Using experimental data, they obtained a nondimensional energy of 0.33 for the pinched off leading vortex ring.

A model for the pinch-off process was developed that predicts the range of observed formation numbers. The model is based on two assumptions: that the circulation, impulse and energy delivered by the cylinder-piston mechanism can be approximated by a slug model (which we extended to the time varying diameter and exit velocity), and that the properties of the pinched off leading vortex ring can be approximated by a vortex ring in the Norbury family. A simple dimensional analysis showed that there are only two universal nondimensional numbers governing the pinch-off process, namely the nondimensional energy

E_{nd} (previously defined by Gharib *et al.* [46]) and a new nondimensional circulation Γ_{nd}. Our model predicts that $0.4 \gtrsim E_{nd} \gtrsim 0.27$ and $1.77 \lesssim \Gamma_{nd} \lesssim 2.07$, which matches with experimental data.

Our approach in modeling the pinch-off phenomena was of relaxational type. The unstable shear layer exiting the cylinder initiates a strong mixing that results in the creation of a vortex ring. The shear layer feeds more circulation, impulse and energy to the leading vortex ring as long as the shear layer velocity adjacent to the vortex ring exceeds the local velocity around the vortex ring. When the two velocities are equal, the shear layer cannot feed any more circulation to the leading vortex ring, causing it to pinch-off and move away from the cylinder. In other words, the leading vortex ring grows larger as long as the invariants of motion provided by the shear layer generator are compatible with the invariants of motion for a steadily translating vortex ring. To this end, an important question is: what is the fate of an axisymmetric ideal fluid? In other words, if an axisymmetric flow starts from a given initial condition, what is the final equilibrium state?

The thermodynamics of the vorticity density field (ω/r) is considered, and the statistical equilibrium theory of Miller, Weichman, and Cross [81, 82] and Robert and Sommeria [115] for 2-D flows in Cartesian coordinates was extended to axisymmetric flows. An assumption made in the theory is that viscous effects in the formation process may be neglected since the viscous timescale is much larger than the relaxation timescale. Apart from this assumption, the statistical equilibrium theory is exact. All the invariants of motion are accounted for, and the mean field equations derived from the statistical equilibrium theory provide equations for deriving the equilibrium state of an axisymmetric flow from its initial condition without resorting to dynamics. The mean field equations do not have the filamentation problem of Euler equations in axisymmetric flows, and can be accurately solved on a coarse grain, meaning that they are computationally much cheaper than integrating Euler equations toward the equilibrium state. It is shown that the resulting mean field satisfies a maximization principle similar to Kelvin's variational principle. We need to develop a numerical scheme for solving the mean field equations in the statistical equilibrium theory, and to examine in detail what type of initial conditions (or rate of providing invariants of motion) correspond to the pinched off cases.

Vortex pinch-off process is a general phenomena, and is not limited to the piston cylinder-mechanism. In order to asses the universality of the invariants of the leading vortex ring, vortex formation by another mechanism, a nonconservative forcing term in the momentum equation, was studied. For applied forces of long duration (simulating experimental vortex ring generation with large stroke ratios), a leading vortex ring is separated from the trailing jet. The results confirm that the formation process in this case is also governed by the same two nondimensional parameters, a normalized energy and normalized circulation, as was suggested in chapter 2. Limiting values of the normalized energy and circulation were found to be about 0.3 and 2.0, respectively, in agreement with experiments [46] and theory [89]. It was shown that by varying the spatial extent of the forcing and the forcing amplitude during the formation process, rings with larger nondimensional circulation can be generated. This corresponds to cylinder-piston mechanism with time varying diameter or accelerating piston velocity during the stroke. The nondimensional energy and circulation of the leading vortex rings were compared with the same properties for vortices in the Norbury family, confirming the assumptions in the model.

It appears that a similar type of universality may exist in some other vortex phenomena. One example is vortex shedding behind bluff bodies, where it is shown by Mohseni [86] that the von Karman ratio for the relative distance between the vortex patches in a Karman street and the universality of the shedding Strouhal number (in the frame of reference of invariants of motion, f U_{tr}/h, where $h \approx$cylinder diameter) can be viewed as manifestations of Kelvin's variational principle. Furthermore, using the new scalings these two numbers were shown to be identical. A possible extension to this work would be estimating the nondimensionalized drag coefficient in this model. Shusser and Gharib [127] obtained the same pinch-off behavior in a starting plume. Another example is the vortex formation at the end of a shock tube, where a similar type of pinch-off process is observed. An important application of vortices is in flow control strategies, *e.g.*, synthetic jets [128]. The limits on circulation and energy of the leading vortex ring may set the maximum gain available for modifying flow characteristics by synthetic jets. These applications require more detailed investigations.

Part II

Evaluation of Mach Wave Radiation in a Supersonic Jet

Chapter 6

Introduction

6.1 Motivation

Ever since the beginning of jet aircraft technology, noise created by jet exhausts has been an important issue. The development of turbojet engines for aeronautical transport in the sixties dramatically increased noise pollution around the airports. The age of civil aviation jets started in the United States in 1958 with the beginning of transoceanic and transcontinental flight operations by DC-8 and Boeing-707 turbojet aircrafts. The takeoff noise of these airplanes was almost 20 dB more than that of the propeller aircrafts that they replaced. The strong public opposition to increase in aircraft noise is the major factor that has prevented most development of new airports. The subject of aerodynamically generated noise is also attracting more interest recently by the continuing efforts to develop a high-speed civil transport plane. Consequently, supersonic jet noise has received much attention in recent years mainly due to a more viable generation of supersonic transport aircrafts. The United States' national effort to reduce the noise around airports is led by FAA (Federal Aviation Administration). The new FAR 36 Stage 3 noise regulations, FAA [33], focused the attention of aircraft industries toward quiet propulsion systems. These rules provide the de facto design requirements for takeoff noise. The FAR Part 36 Stages 1 and 2 have already made major improvements in noise radiation from civil aircrafts [35]. Consequently, the FAA has amended FAR Part 91 [34] to regulate an orderly phaseout of most of the stage 2 aircraft from the civil fleet by the year 2000. The success of the new technologies is contingent upon reducing their jet exhaust noise. To meet the low level

noise requirements in international standards around airports, more research is needed to understand the physics of sound generation in turbulent jets, which is vital for improvement of jet noise suppression methods, and needs to be advanced beyond current levels.

The pioneering work of Sir M.J. Lighthill in the 1950's paved the road for theoretical investigation on jet noise problems. In Lighthill's analogy the problem of noise radiation in a turbulent flow is replaced by an acoustic radiation problem in a fluid at rest with equivalent acoustic sources. He manipulated the fundamental equations of fluid motion to isolate terms that represent the fluctuating stresses created in a localized region of space in a moving fluid. These unsteady stresses become the source terms in a wave equation for the sound that propagates into the surrounding medium at rest. Lighthill's acoustic analogy is exact, *i.e.*, there is no special assumption or any linearization. The main aeroacoustic processes, such as sound generation by inhomogeneities in the flow, sound dissipation by viscosity or heat conduction, are all accounted for. The main victory of Lighthill's theory was the correct prediction of a scaling law for sound generation in a free jet. The theory predicted that the total power radiated by the jet would be proportional to the eight power of the jet velocity, U_j^8. The Lighthill approach applies to both subsonic and supersonic jets. When the convection velocity of the eddies becomes supersonic (around $M_j \approx 1.5$), the total acoustic power changes its proportionality from U_0^8 to U_0^3, and there is a continuous transition from the U_0^8-law for subsonic jets to the U_0^3-law for supersonic jets. While eddies need to be unsteady in a convected frame of reference in order to radiate noise at convective Mach number $M_c < 1$, even "frozen" turbulence may contribute to the noise for $M_c > 1$.

6.2 Mach Wave Radiation

Supersonic jet noise is usually broadband, and consists of three major elements: turbulent mixing noise (lower frequencies), screech tone, and shock noise (higher frequencies). For a perfectly expanded jet only turbulent mixing noise exists. If the jet is not perfectly expanded, quasiperiodic shock cells will form in the jet. In this case interaction of turbulent eddies with the shock waves is responsible for the shock noise generation, and acoustic feedback between the shocks and the nozzle lips results in discrete tones. In this study we

focus only on the noise generation in a perfectly expanded jet. For a review of shock noise and screech tone and related references, we refer to Tam [141] and Raman [114].

In the last three decades one of the important developments in turbulent research was the recognition of large scale turbulent structures in shear flows (see Brown and Roshko [11]). These structures have a central role in the spreading of shear layers, and the dynamics of such structures was observed to control the mixing process. There is theoretical and experimental evidence [143, 152] that suggests the noise generated by large structures constitutes the principal part of the supersonic turbulent mixing noise. These sound sources originate from the convection of large scales at supersonic speed relative to ambient and thus generate intense Mach wave radiation. Crudely speaking, the eddies behave like a supersonic projectile that emits Mach waves in the direction

$$\theta \approx \cos^{-1}\left(\frac{1}{M_c}\right) \tag{6.1}$$

First Phillips [110], and later on Ffowcs Williams [161], described this noise mechanism through the development of a convected wave equation, which is based on the Lighthill acoustic analogy approach. This approach was difficult to implement both experimentally and computationally. On the other hand, when the large scale structures are phase locked to external excitation, there is some experimental evidence to support models based on the linear stability analysis for predicting the local distribution of amplitude and phase of these structures (*e.g.*, Gaster *et al.* [45] and Petersen and Samet [109]).

This growing recognition of large scale structures in shear flows [11] and their interpretation as instability waves [25] in the early seventies led to alternative theories for noise generation in supersonic jets. An early attempt by Liu [68] was made to represent sound sources as instability waves. He found that some of these instability waves travel supersonically with their peak amplitude inside the shear layer and decay in the radial direction away from the jet. Liu [67], then, used these remnants of the instability waves outside the jet to calculate the near field jet noise. Tam and Morris [147] and Tam and Burton [142, 143] used these ideas in the context of Mach wave radiation by linear stability waves, which was more tractable at the time. Their approach is considered in detailed in the next chapter.

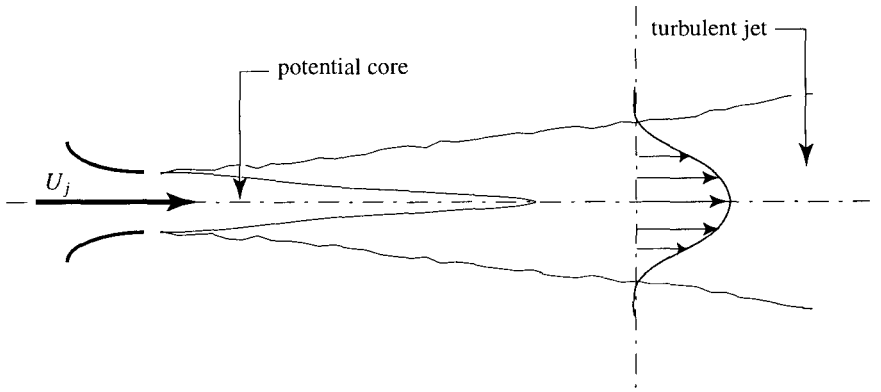

Figure 6.1 Schematics of a turbulent jet.

In Tam and Morris' analysis the large scale structures of the flow are modeled locally as linear stability waves, using the integral analysis proposed by Stuart [130]. In this wave envelope approach the local distribution of the finite amplitude fluctuations is described by linear theory. At low Reynolds numbers experimental measurements [98] supported the idea that the rapid growth and decay of instability waves near the end of the potential core (see figure 6.1) made a major contribution to the radiated sound from the jet. Initial growth rates of the instability waves and their phase velocities agreed with the linear theory, and the peak Strouhal numbers agreed with the predictions of the instability theory. As Reynolds numbers increased (see experiments at moderate Reynolds numbers [152]) the spectra broadened but still showed reasonable agreement with the Strouhal numbers of the predicted most amplified waves.

There is a large class of articles that are mainly concerned with the noise generation in fully expanded jets and shear layers by instability waves. We refer to the followings and the references therein: Tam [136, 137, 138, 139, 140], Tam and Burton [142, 143] Tam and Chen [144], Tam, Chen, and Seiner [145], Tam and Morris [147], McLaughlin, Seiner, and Liu [77], Chan and Westley [13], Sedelnikov [122], Morris [93], Morris and Bhat [94, 95, 96], Dahl and Morris [26, 27, 28], Moore [92], Merkine and Liu [80]. Their observations provided evidence for linear mechanism of Mach wave radiation. However, as we mentioned before, one should realize that any supersonic structure that is moving by the mean flow will radiate

Mach waves with the appropriate radiation angle approximated by equation (6.1). Now, since the visually observed large-scales in a turbulent flow (*e.g.*, [11]) are usually moving with a convective velocity M_c, in the range of $0.6M_j \lesssim M_c \lesssim 0.7M_j$ (*e.g.*, [108]) they will radiate Mach waves at an angle that is approximately predicted by equation (6.1). Therefore, any model that can represent some of the dynamics of large scale turbulent structures will be convecting downstream with the convective velocity that is dictated by the mean flow, and consequently radiate Mach waves. Thus, it is not surprising that representing the large scale turbulent structures with instability waves does a reasonable job in predicting Mach wave directivity. The main factor in setting the directivity of a jet is the mean velocity profile and the main convective velocity. To this end, the mean flow is clearly established in a *nonlinear* process. Given this mean flow, however, an important question is this: are the linear Mach wave generation mechanisms dominant sound sources or does the sound generation by nonlinear interaction of large scale structures contribute significantly to the far field noise?

Another important assumption in Tam and Burton's theory [143] is that at each frequency they consider only a *single* instability wave as the representative of the major energy carrying wave component. In this respect the stochastic model of the instability waves that was developed by Tam and Chen [144] makes use of the single instability solution to construct a broadband jet noise theory. They have argued that the instability wave spectrum of the jet may be regarded as being generated by the stochastic white noise excitation at the nozzle lip region. Their justification for the white noise spectrum of the excitations is that near the nozzle lip region the flow in the jet mixing layer has no intrinsic time and length scales.

Thus, our principal objective in this study is to evaluate the validity of the assumptions in Tam and Burton's theory by direct comparison of the results for LNS (Linearized Navier-Stokes) calculations with the corresponding DNS (Direct Numerical Simulation) data.

6.3 Computational Tools

Most fluid problems are governed by nonlinear partial differential equations for which closed form solutions are difficult to obtain. The development of high-speed computers opened new possibilities for applying the principles of science to engineering problems in fluid mechanics. Computational Fluid Dynamics (CFD) is considered as a new approach, complementing experimental and theoretical methods in improving our understanding of fluid problems. Computational Aeroacoustics (CAA) is concerned with sound generation by aerodynamic forces through computational means. It combines the traditional disciplines of aeroacoustics and CFD. While CAA is a part of CFD, its particular requirements make it different from many classical approaches in CFD.

In recent years simultaneous direct simulations of flow field as well as its radiated sound offer the most detailed description of sound generation process in aeroacoustics [21, 23, 83, 43, 40, 17]. Some of the computational issues relevant to jet noise are discussed below. Acoustical signals are often orders of magnitude smaller than the flow field generating the sound and can be easily contaminated by inaccuracy in the numerical schemes or boundary conditions. Sound is a small amplitude by-product of flows which needs special algorithms to be resolved accurately. Large disparity between the sound levels and the unsteady flow fluctuations presents a severe challenge to direct numerical simulation. Extreme care needs to be taken so that the acoustic pressure fluctuations do not get lost in the inherent numerical errors of the calculations. Well-separated length scales between the thickness of the shear layer that controls the instability waves and the acoustic wavelength, which is many times the jet radius, demands extreme computational powers.

Regardless of the application, all CFD codes are subject to numerical error. Any propagating wave will always suffer from accumulating amplitude and phase errors; there is an intimate coupling of time and space in an acoustic wave. These undesirable effects can be limited by increasing the number resolution of the computation, but this leads to enormous memory and computational requirements. An acoustic wave has a frequency $\omega = 2\pi f$ in time and a wavelength λ in space that are related by $\lambda f = c$, where c is the sound speed in the medium (assumed quiescent). Thus, to resolve an acoustic wave one needs to accurately resolve the wave length as well as its frequency; special care must be taken in

choosing the spatial and temporal discretization of aeroacoustics problems. Highly accurate time integrations are usually advised in aeroacoustic computations. When an open domain problem such as jet noise is solved computationally, one needs to prescribe numerical boundary conditions at the computational boundary. These boundary conditions are usually dubbed as nonreflecting boundary conditions. An accurate nonreflecting boundary condition is essential to the overall performance of CAA (see appendix C).

6.4 Approach

To investigate the physics of Mach wave radiation and to answer the questions addressed in the previous sections, we have adapted a computational approach. Direct simulation of both hydrodynamic fluctuations and acoustic field provide a detailed data base of the jet flow, and put us in a unique position to examine Mach wave radiation mechanisms.

When DNS data is available, in principal the questions at the end of section 6.2 can be addressed theoretically with linear stability theory (LST) and the method of matched asymptotic expansion. In particular, we tried to calculate the free scaling factor in LST by an adjoint analysis [24]. In this approach, we first obtain the adjoint equations of the linearized equations for the flow region. Subsequently, a biorthogonality relation provides the necessary mathematical tool for projecting any flow signals to the eigenfunctions of the linear stability equations. However, due to some technical difficulties in the matched asymptotic expansion analysis of the adjoint equations, we found it more appropriate to directly solve the linearized Navier-Stokes (LNS) equations. The LNS method does not have the simplifying assumptions of the LST, and an accurate evaluation of the linear stability predictions can be made.

Direct numerical solution of the linearized Navier-Stokes equations for jet flows are not something new. Hixon *et al.* [54] used a solution to linearized Euler equations for noise prediction in an axisymmetric supersonic jet. He used an analytic mean flow profile in his calculations. Morris *et al.* [97] solved the Reynolds average Navier stokes equations, with a simple algebraic turbulence model, for the mean flow quantities along with a with a nonlinear disturbance equation for the perturbation part.

Accurate computations of the flow and acoustic fields of two-dimensional mixing problems by Colonius *et al.* [20] and Mitchell *et al.* [83] paved the road for a full three-dimensional DNS of jet noise problem. Chyczewski and Long [17] performed a DNS solution of a rectangular jet that includes the jet plume and a small region of the acoustic near field. They have developed a set of unsteady conditions at the nozzle exit that can specify the disturbance spatial distribution, amplitude, temporal behavior and phase relation around the nozzle lip. These simulations rely on an *ad hoc* model of the unsteady flow at the exit of the nozzle. A more realistic inflow condition was developed by Freund *et al.* [42], where they provide the inflow boundary condition by feeding the result of a turbulence simulation of a periodic jet. His accurate calculation of the hydrodynamic fluctuations as well as the near field acoustics affords us an opportunity to investigate the specific agreement of linear theory with DNS of a realistic supersonic jet. To this end, we have developed a linearized Navier-Stokes solver that uses the mean flow quantities, grid distribution and inflow boundary conditions, including an identical specification of incoming turbulent disturbances, from Freund *et al.* [42] simulation. We then evaluate the Mach wave radiation mechanisms in a fully expanded supersonic turbulent jet by comparing the results of a Mach 1.92 direct numerical simulation (raw data for DNS calculations are provided by J. Freund [40]) with the numerical solution of the linearized Navier-Stokes equations, as well as LST (Linear Stability Theory) of Tam and Morris [147] and Tam and Burton [143]. This way a detailed analysis of the hydrodynamic flow and acoustic fields of a DNS data are contrasted with its exact linearized computation. This technique will answer some of the fundamental questions regarding the nature of noise generation in supersonic jets and, as we will demonstrate in chapter 8, sheds some light on the contributions of linear and nonlinear interactions of turbulent structures to the noise generation, and the role of instability waves in noise generation mechanisms.

We will show that the noise generation in the supersonic jet, considered in this study, is dominated by the first two azimuthal modes. Their contributions are equally important in the DNS calculation. However, the LNS or LST predicts more contributions from the azimuthal mode $n = 1$. The sound generation directivity of the azimuthal mode $n = 1$, matches well with the predictions by linearized equations. The same agreement was not

observed for $n = 0$. The noise generated by the first two modes in the linearized computation is substantially weaker than in the DNS. For example, in the near acoustic field, at a distance of 6 jet diameters from the jet center line, the sound pressure level in the linearized computation is as much as 8 db smaller than the DNS results, which is argued to be due to nonlinear interactions among turbulent scales. Therefore, nonlinear mechanisms in Mach wave radiation are strong noise sources that cannot be ignored in a complete theory of Mach wave radiation. A comprehensive noise generation theory will include Mach wave radiation by linear and nonlinear mechanisms, as well as small scales turbulence.

On the numerical development side of our study we have developed an effective strategy for treating the geometrical singularity in finite difference, and pseudo-spectral methods in polar coordinates. This technique is quite effective in reducing the spurious reflections from the coordinate singularity in jet noise calculations. The treatment is based solely on the geometry of the coordinate system and manipulation of grid point locations, and is independent of the equations under consideration. The technique is shown to be very general and applicable to a wide range of problems in cylindrical coordinates.

Chapter 7

Computational Techniques

This chapter presents the simulation techniques adopted in this study for evaluation of noise generation in a fully expanded supersonic jet. In the first section the governing equations of full DNS and LNS calculations are presented. The computational issues in LNS calculations are discussed in section 7.2. The raw DNS data in our study, including mean flow and inflow data, were provided by Professor J. Freund [40, 42]. Discussions on the linearized theory of supersonic jet noise and its numerical issues are covered in section 7.3. Finally the signal processing techniques implemented in this study are presented in section 7.4.

7.1 Governing Equations

In this section we review the governing equations implemented in DNS and LNS computations.

7.1.1 Compressible Navier-Stokes Equations

The flow field of a supersonic jet is governed by the compressible Navier-Stokes (NS) equations. These equations of motion, which are the continuity, momentum and energy equations along with an equation of state, are considered in this section. The physical quantities are nondimensionalized based on the jet radius, R_0, and density and sound speed at infinity,

ρ_∞ and a_∞. Hence,

$$\boldsymbol{x} = \frac{\boldsymbol{x}^d}{R_0}, \qquad \boldsymbol{v} = \frac{\boldsymbol{v}^d}{a_\infty}, \qquad t = \frac{t^d a_\infty}{R_0},$$
$$\rho = \frac{\rho^d}{\rho_\infty}, \qquad p = \frac{p^d}{\rho_\infty a_\infty^2}, \qquad T = \frac{T^d c_p}{a_\infty^2}, \qquad e = \frac{e^d}{\rho_\infty a_\infty^2},$$

where $\boldsymbol{x}$ is a position vector; t, time; $\boldsymbol{u}$, velocity vector; ρ mass density; p, pressure; T, temperature; and e, total energy per unit volume. In cylindrical coordinates (x, r, θ) the governing equations are:

$$\frac{\partial \rho}{\partial t} + \frac{\partial (\rho u)}{\partial x} + \frac{1}{r}\frac{\partial (r\rho v_r)}{\partial r} + \frac{1}{r}\frac{\partial (\rho v_\theta)}{\partial \theta} = 0, \tag{7.1}$$

$$\frac{\partial (\rho u)}{\partial t} + \frac{\partial (\rho u u)}{\partial x} + \frac{1}{r}\frac{\partial (r\rho u v_r)}{\partial r} + \frac{1}{r}\frac{\partial (\rho u v_\theta)}{\partial \theta} = -\frac{\partial p}{\partial x} + V_x, \tag{7.2}$$

$$\frac{\partial (\rho v_r)}{\partial t} + \frac{\partial (\rho v_r u)}{\partial x} + \frac{1}{r}\frac{\partial (r\rho v_r v_r)}{\partial r} + \frac{1}{r}\frac{\partial (\rho v_r v_\theta)}{\partial \theta} - \frac{\rho v_\theta^2}{r} = -\frac{\partial p}{\partial r} + V_r, \tag{7.3}$$

$$\frac{\partial (\rho v_\theta)}{\partial t} + \frac{\partial (\rho v_\theta u)}{\partial x} + \frac{1}{r}\frac{\partial (r\rho v_\theta v_r)}{\partial r} + \frac{1}{r}\frac{\partial (\rho v_\theta v_\theta)}{\partial \theta} + \frac{\rho v_r v_\theta}{r} = -\frac{1}{r}\frac{\partial p}{\partial \theta} + V_\theta, \tag{7.4}$$

$$\frac{\partial e}{\partial t} + \frac{\partial [u\,(e+p)]}{\partial x} + \frac{1}{r}\frac{\partial [r v_r\,(e+p)]}{\partial r} + \frac{1}{r}\frac{\partial [v_\theta\,(e+p)]}{\partial \theta} = \frac{\partial q}{\partial x} + \frac{1}{r}\frac{\partial r q}{\partial r} + \frac{1}{r}\frac{\partial q}{\partial \theta} + + u V_x + v_r V_r + v_\theta V_\theta + \Phi, \tag{7.5}$$

where u is the axial velocity; v_r, the radial velocity; and v_θ, the azimuthal velocity. The total energy per unit volume e is the sum of the internal energy and the kinetic energy and is given by

$$e = \frac{p}{\gamma - 1} + \frac{\rho}{2}\left(u^2 + v_r^2 + v_\theta^2\right).$$

The heat flux q in the energy equation (7.5) is modeled by Fourier's law. The viscous terms in cylindrical coordinates are given by

$$V_x = \frac{\partial \tau_{xx}}{\partial x} + \frac{1}{r}\frac{(r\tau_{xr})}{\partial r} + \frac{1}{r}\frac{\tau_{x\theta}}{\partial \theta}, \tag{7.6}$$

$$V_r = \frac{\partial \tau_{xr}}{\partial x} + \frac{1}{r}\frac{\partial (r\tau_{rr})}{\partial r} + \frac{1}{r}\frac{\partial \tau_{r\theta}}{\partial \theta} - \frac{1}{r}\tau_{\theta\theta}, \tag{7.7}$$

$$V_\theta = \frac{\partial \tau_{x\theta}}{\partial x} + \frac{1}{r}\frac{\partial (r\tau_{\theta r})}{\partial r} + \frac{1}{r}\frac{\tau_{\theta\theta}}{\partial \theta} + \frac{1}{r}\tau_{r\theta}, \tag{7.8}$$

$$\begin{aligned}\Phi = {} & \tau_{xx}\frac{\partial u}{\partial x} + \tau_{xr}\frac{\partial v_r}{\partial x} + \tau_{x\theta}\frac{\partial v_\theta}{\partial x} + \tau_{xr}\frac{\partial u}{\partial r} + \tau_{rr}\frac{\partial v_r}{\partial r} + \tau_{\theta r}\frac{\partial v_\theta}{\partial \theta} \\ & + \frac{1}{r}\left(\tau_{x\theta}\frac{\partial u}{\partial \theta} + \tau_{r\theta}\frac{\partial v_r}{\partial \theta} + \tau_{\theta\theta}\frac{\partial v_\theta}{\partial \theta} + v_r\tau_{\theta\theta} - v_\theta\tau_{r\theta}\right).\end{aligned} \tag{7.9}$$

To specify the viscous stress tensor, we assume a Newtonian fluid and so its components are linearly related to the fluid strain rates by the viscosity $\mu = \mu(T)$. Consequently, the viscous terms can be written as

$$\begin{aligned}ReV_x = {} & (\mu^* + \lambda^*)\frac{\partial \Theta}{\partial x} + \mu^*\Delta u + 2\frac{\partial \mu^*}{\partial x}\frac{\partial u}{\partial x} + \frac{\partial \lambda^*}{\partial x}\Theta \\ & + \frac{\partial \mu^*}{\partial r}\left(\frac{\partial v_r}{\partial x} + \frac{\partial u}{\partial r}\right) + \frac{1}{r}\frac{\partial \mu^*}{\partial \theta}\left(\frac{\partial v_\theta}{\partial x} + \frac{1}{r}\frac{\partial u}{\partial \theta}\right),\end{aligned} \tag{7.10}$$

$$\begin{aligned}ReV_r = {} & (\mu^* + \lambda^*)\frac{\partial \Theta}{\partial r} + \mu^*\left[\Delta v_r - \frac{1}{r^2}\left(v_r + 2\frac{\partial v_\theta}{\partial \theta}\right)\right] \\ & + \frac{\partial \mu^*}{\partial x}\left(\frac{\partial v_r}{\partial x} + \frac{\partial u}{\partial r}\right) + 2\frac{\partial \mu^*}{\partial r}\frac{\partial v_r}{\partial r} \\ & + \frac{\partial \lambda^*}{\partial r}\Theta + \frac{1}{r}\frac{\partial \mu^*}{\partial \theta}\left[\frac{\partial v_\theta}{\partial r} + \frac{1}{r}\left(\frac{\partial v_r}{\partial \theta} - v_\theta\right)\right],\end{aligned} \tag{7.11}$$

$$\begin{aligned}ReV_\theta = {} & (\mu^* + \lambda^*)\frac{1}{r}\frac{\partial \Theta}{\partial \theta} + \mu^*\left[\Delta v_\theta + \frac{1}{r^2}\left(-v_\theta + 2\frac{\partial v_r}{\partial \theta}\right)\right] \\ & + \frac{\partial \mu^*}{\partial x}\left(\frac{\partial v_\theta}{\partial x} + \frac{1}{r}\frac{\partial u}{\partial \theta}\right) + \frac{\partial \mu^*}{\partial r}\left[\frac{\partial v_\theta}{\partial r} + \frac{1}{r}\left(\frac{\partial v_r}{\partial \theta} - v_\theta\right)\right] \\ & + \frac{2}{r^2}\frac{\partial \mu^*}{\partial \theta}\left(\frac{\partial v_\theta}{\partial \theta} + v_r\right) + \frac{1}{r}\frac{\partial \lambda^*}{\partial \theta}\Theta,\end{aligned} \tag{7.12}$$

$$\begin{aligned}Re\Phi = {} & \frac{2\mu^*}{Re}\left[\left(\frac{\partial u}{\partial x}\right)^2 + \left(\frac{\partial v_r}{\partial r}\right)^2 + \frac{1}{r^2}\left(\frac{\partial v_\theta}{\partial \theta} + v_r\right)^2\right] \\ & + \frac{\mu^*}{Re}\left[\left(\frac{\partial v_r}{\partial x} + \frac{\partial u}{\partial r}\right)^2 + \left(\frac{1}{r}\frac{\partial u}{\partial \theta} + \frac{\partial v_\theta}{\partial x}\right)^2 + \left(\frac{1}{r}\frac{\partial v_r}{\partial \theta} + \frac{\partial v_\theta}{\partial r} - \frac{v_\theta}{r}\right)^2\right] + \frac{\lambda^*}{Re}\Theta^2,\end{aligned} \tag{7.13}$$

where the acoustic Reynolds number and Prandtle numbers are defined as

$$Re = \frac{\rho_\infty a_\infty R_0}{\mu_\infty}, \qquad Pr = \frac{\mu c_p}{\kappa}.$$

Θ is the dilatation and is defined as the divergence of the velocity field, and in cylindrical coordinates can be represented by

$$\Theta = \nabla \cdot \mathbf{V} = \frac{\partial u}{\partial x} + \frac{1}{r}\frac{\partial (r v_r)}{\partial r} + \frac{1}{r}\frac{\partial v_\theta}{\partial \theta} = \frac{\partial u}{\partial x} + \frac{\partial v_r}{\partial r} + \frac{1}{r}\left(\frac{\partial v_\theta}{\partial \theta} + v_r\right).$$

The state equation for a perfect gas is given by $p = \dfrac{\gamma - 1}{\gamma}\rho T$.

The bulk viscosity μ_B (nondimensionalized by viscosity at infinity, μ_∞) is defined by $\mu_B = \lambda + \frac{2}{3}\mu$ where λ is a second coefficient of viscosity. For a low density monoatomic gas $\mu_B = 0$, and is probably not very important in dense gases and liquids. It is usually assumed that bulk viscosity is related to shear viscosity by a constant ratio $\mu_B = C_\mu \mu$. The value given for air by Thompson [150] is $C_\mu = 0.6$, which was used in the direct numerical simulations [42] and our linearized Navier-Stokes calculations.

In most direct simulations a power relation of the form $\mu(T) \sim T^\alpha$ is used to specify the functional dependence of viscosity upon temperature. The popularity of power law in DNS is due to it not requiring a reference temperature T_0 or the constant S defined below. However, in this study we use Sutherland's law [160] which is more accurate and is consistent with what is used in the available DNS data [43]. Sutherland's law can be represented as

$$\mu^* = \frac{\mu}{\mu_0} = \left(\frac{T}{T_0}\right)^{\frac{3}{2}} \frac{T_0 + S}{T + S}. \tag{7.14}$$

We set $T_0 = T_\infty$ and $S = 0.4 T_\infty$ which corresponds to air at atmospheric conditions.

Equations (7.1-7.5) are implemented in the DNS computations [42]. Numerical issues in solving these equations are discussed by Freund, Lele, and Moin [42, 43], and are not repeated here.

7.1.2 Linearized NS Equations

We linearize the governing equations around the mean flow in conservative form to obtain (assuming constant viscosity)

$$\frac{\partial \boldsymbol{Q'}}{\partial t} + \frac{\partial \boldsymbol{E'}}{\partial x} + \frac{\partial \boldsymbol{F'}}{\partial r} + \frac{1}{r}\frac{\partial \boldsymbol{G'}}{\partial \theta} + \boldsymbol{H'} = \boldsymbol{I'}, \tag{7.15}$$

where

$$\boldsymbol{Q'} = \begin{pmatrix} \rho' \\ \rho'\bar{u} + u'\bar{\rho} \\ \rho'\bar{v_r} + v_r'\bar{\rho} \\ \rho'\bar{v_\theta} + v_\theta'\bar{\rho} \\ e' \end{pmatrix}, \qquad \boldsymbol{E'} = \begin{pmatrix} \rho'\bar{u} + u'\bar{\rho} \\ \rho'\bar{u}\bar{u} + u'\bar{\rho}\bar{u} + u'\bar{\rho}\bar{u} + p' \\ \rho'\bar{v_r}\bar{u} + v_r'\bar{\rho}\bar{u} + u'\bar{\rho}\bar{v_r} \\ \rho'\bar{v_\theta}\bar{u} + v_\theta'\bar{\rho}\bar{u} + u'\bar{\rho}\bar{v_\theta} \\ u'(\bar{e} + \bar{p}) + \bar{u}(e' + p'), \end{pmatrix}$$

$$\boldsymbol{F'} = \begin{pmatrix} \rho'\bar{v_r} + v_r'\bar{\rho} \\ \rho'\bar{u}\bar{v_r} + u'\bar{\rho}\bar{v_r} + v_r'\bar{\rho}\bar{u} \\ \rho'\bar{v_r}\bar{v_r} + v_r'\bar{\rho}\bar{v_r} + v_r'\bar{\rho}\bar{v_r} + p' \\ \rho'\bar{v_\theta}\bar{v_r} + v_\theta'\bar{\rho}\bar{v_r} + v_r'\bar{\rho}\bar{v_\theta} \\ v_r'(\bar{e} + \bar{p}) + \bar{v_r}(e' + p'), \end{pmatrix} \qquad \boldsymbol{G'} = \begin{pmatrix} \rho'\bar{v_\theta} + v_\theta'\bar{\rho} \\ \rho'\bar{u}\bar{v_\theta} + u'\bar{\rho}\bar{v_\theta} + v_\theta'\bar{\rho}\bar{u} \\ \rho'\bar{v_r}\bar{v_\theta} + v_r'\bar{\rho}\bar{v_\theta} + v_\theta'\bar{\rho}\bar{v_r} \\ \rho'\bar{v_\theta}\bar{v_\theta} + v_\theta'\bar{\rho}\bar{v_\theta} + v_\theta'\bar{\rho}\bar{v_\theta} + p' \\ v_\theta'(\bar{e} + \bar{p}) + \bar{v_\theta}(e' + p'), \end{pmatrix}$$

$$\boldsymbol{H'} = \frac{1}{r}\begin{pmatrix} \rho'v_r' + v_r'\bar{\rho} \\ \rho'\bar{u}\bar{v_r} + u'\bar{\rho}\bar{v_r} + v_r'\bar{\rho}\bar{u} \\ \rho'\bar{v_r}\bar{v_r} + 2v_r'\bar{\rho}\bar{v_r} - (\rho'\bar{v_\theta}^2 + 2v_\theta'\bar{\rho}\bar{\theta}) \\ 2(\rho'\bar{v_\theta}\bar{v_r} + v_\theta'\bar{\rho}\bar{v_r} + v_r'\bar{\rho}\bar{v_\theta}) \\ v_r'(\bar{e} + \bar{p}) + \bar{v_r}(e' + p'), \end{pmatrix}$$

$$\boldsymbol{I}' = \begin{pmatrix} 0 \\ V_x' \\ V_r' \\ V_\theta' \\ \frac{1}{RePr}\Delta T' + u'\bar{V}_x + + v_r'\bar{V}_r + v_\theta'\bar{V}_\theta + \bar{u}V_x' + \bar{v}_r V_r' + \bar{v}_\theta V_\theta' + \Phi'. \end{pmatrix}$$

Note that

$$\begin{aligned} e' &= \frac{p'}{\gamma - 1} + \frac{\rho'}{2}\left(\bar{u}^2 + \bar{v_r}^2 + \bar{v_\theta}^2\right) + \bar{\rho}\left(u'\bar{u} + v_r'\bar{v}_r + v_\theta'\bar{v}_\theta\right), \\ T' &= \frac{\gamma}{\gamma - 1}\left(\frac{p'}{\bar{\rho}} - \frac{\bar{p}}{\bar{\rho}}\rho'\right). \end{aligned}$$

Since V_x, V_r, V_θ, and Θ are linear quantities, their mean or perturbation values are calculated by simply replacing the mean or perturbation variables in their definitions for total quantities in equations (7.10-7.12) and (7.1.1), respectively. Φ, on the other hand, is a nonlinear quantity. While its mean value is calculated by replacing the total quantities by their mean variables in equation (7.13), its perturbation value is given by

$$\begin{aligned} Re\Phi' &= 4\mu^*\left[\frac{\partial u'}{\partial x}\frac{\partial \bar{u}}{\partial x} + \frac{\partial v_r'}{\partial r}\frac{\partial \bar{v_r}}{\partial r} + \left(\frac{\partial v_\theta'}{\partial \theta} + v_\theta'\right)\left(\frac{\partial \bar{v}_\theta}{\partial \theta} + \bar{v_r}\right)\right] \\ &+2\mu^*\left[\left(\frac{\partial v_r'}{\partial x} + \frac{\partial u'}{\partial r}\right)\left(\frac{\partial \bar{v_r}}{\partial x} + \frac{\partial \bar{u}}{\partial r}\right) + \left(\frac{1}{r}\frac{\partial u'}{\partial \theta} + \frac{\partial v_\theta'}{\partial x}\right)\left(\frac{1}{r}\frac{\partial \bar{u}}{\partial \theta} + \frac{\partial \bar{v}_\theta}{\partial x}\right)\right. \\ &\left. + \left(\frac{1}{r}\frac{\partial v_r'}{\partial \theta} + \frac{\partial v_\theta'}{\partial r} - \frac{v_\theta'}{r}\right)\left(\frac{1}{r}\frac{\partial \bar{v_r}}{\partial \theta} + \frac{\partial \bar{v}_\theta}{\partial r} - \frac{\bar{v}_\theta}{r}\right)\right] + \lambda^*\Theta'^2. \end{aligned}$$

Alternatively one can linearize the governing equations in the primitive variables. The difference between these two methods of linearization is of second order in perturbation quantities.

7.2 Numerical Simulation of Linearized NS Equations

One of the main characteristics of an efficient aeroacoustic algorithm is its ability to accurately predict the phase velocity and the direction of propagation of a traveling wave. To ensure that the wave characteristics of the system of discretized equations are (nearly) iden-

tical to those of the continuous equations, it is necessary that both systems have (nearly) identical dispersion relation. On the other hand, the numerical scheme for such unsteady problems must have minimal dissipation to resolve the amplitude of perturbations over many orders of magnitudes of spatial scales. To this end, we use a combination of sixth order compact Pade scheme in axial and radial direction, a Fourier spectral method in the azimuthal direction, and a fourth order Runge-Kutta time advancement is used to advance the solution to the next time step. This combination of spatial and temporal algorithms has very good dispersion properties and minimal dissipation required for accurate calculation of both far field noise and near field disturbances. This combination of high-order-accurate compact finite difference schemes and explicit Runge-Kutta time advancements has now been used in many codes developed for solving problems in compressible turbulence and aeroacoustics (*e.g.*, [23, 40, 83, 84]). A detail description of the numerical method for solving the LNS equations is given in this section.

The flow parameters in the LNS calculations are set to their corresponding values in the DNS calculation. These are:

$$
\begin{aligned}
Pr &= 0.7, \\
\frac{T_\infty}{T_j} &= 0.89, \\
Re_j &= \frac{\rho_j U_j D_j}{\mu_j} = 2000, \\
M &= \frac{U_j}{a_\infty} = 1.92.
\end{aligned}
$$

The isentropic convective Mach number [107] for these conditions is $M_c = 0.99$.

Numerical Discretization in Axial and Radial Directions

Various compact Pade schemes considered in [64] revealed a significant reduction of dispersion error compared to their centered difference counterparts. In this study we implement a sixth order compact Pade scheme for calculation of spatial derivatives in axial and radial

directions. For a grid of N points with spacing Δs, the first derivative is approximated by

$$f'_{i-1} + 3f'_i + f'_{i+1} = \frac{1}{12\Delta s}\left((f_{i+2} - f_{i-2}) + 28(f_{i+1} - f_{i-1})\right), \tag{7.16}$$

and the second derivative is given implicitly as

$$2f''_{i-1} + 11f''_i + 2f''_{i+1} = \frac{4}{(\Delta s)^2}\left(3(f_{i+2} - 2f_i + f_{i-2}) + 48(f_{i+1} - 2f_i + f_{i-1})\right), \tag{7.17}$$

for $2 < i < N - 1$. At the two points nearest to the boundary, one needs to use special schemes to close the set of equations. At the second closest point to the boundary, i=2, it is recommended to use the 4th order Pade scheme

$$f'_1 + 4f'_2 + f'_3 = \frac{3}{\Delta s}\left(f_3 - f_1\right), \tag{7.18}$$

$$f''_1 + 10f''_2 + f''_3 = \frac{12}{(\Delta s)^2}\left(f_1 - 2f_2 + f_3\right), \tag{7.19}$$

and at the closet point to the boundary, i=1, a one-sided third order scheme is used

$$2f'_1 + 4f'_2 = \frac{1}{\Delta s}\left(-5f_1 + 2f_2 + f_3\right), \tag{7.20}$$

$$f''_1 + 11f''_2 = \frac{1}{(\Delta s)^2}\left(-13f_1 - 27f_2 + 15f_3 - f_4\right). \tag{7.21}$$

Similar relations are used for points $i = N - 1$, and N. These equations for the first and second derivatives represent systems of N tridiagonal equations that can be solved for the corresponding derivatives. Each system was LDU decomposed and was solved by the Thomas tridiagonal solver. The computational cost is of order $O(N)$.

Note that since the coordinate singularity is not treated as a computational boundary and there is no grid point at the singular point, there is no need for a special closure scheme for grid points near the coordinate singularity. Sixth order Pade is used at all grid points except the two points closest to the boundary.

Numerical Discretization in Azimuthal Direction

Since the azimuthal grids are periodic, a Fourier spectral method is used in this direction. All the flow quantities are stored in the physical space. Flow quantities are transformed into the Fourier space, where azimuthal derivatives are easily calculated by a multiplication by ik_θ, where k_θ is the azimuthal wave number.

The computational code that we developed is capable of solving both linearized and fully nonlinear Navier-Stokes equations, and is designed for full three-dimensional calculations with many azimuthal grids. The maximum allowable time-step for convective problems is usually controlled by the Courant-Friedrichs-Lewy (CFL) number. A conservative estimate for the CFL number will depend on the minimum mesh spacing in any of the three coordinate directions. In cylindrical coordinates a severe time step restriction is imposed by a very fine grid distribution in the azimuthal direction around $r = 0$.

It is possible to alleviate this constraint by explicitly filtering the results in the θ direction, as has been suggested by many investigators (*e.g.*, [12] and references therein). Since the solution is periodic in the θ direction, it is possible to employ a sharp spectral filter at a particular cutoff wavenumber. A detailed description of filtering using this approach was presented by Mohseni and Colonius [88] and reproduced in the appendix A. In summary, by appropriate filtering, one can make the CFL constraint depend on Δr alone and not $\Delta r \Delta\theta$. Another issue is the nonlinear multiplications in the governing equations for full Navier-Stokes equations lead to aliasing errors, and require a straightforward de-aliasing procedure. However, this will not be an issue for linearized equations. In any case, in our linearized calculations we focus only on the first two azimuthal modes. Consequently, only four points in the azimuthal direction are used. Therefore, the azimuthal concentration of grid points near $r = 0$ or aliasing errors will not be an issue.

7.2.1 Computational Grid

To optimize the computational resources, a grid stretching scheme is implemented in the axial and radial directions so that the grids are more concentrated in the regions where the spatial structures are smaller.

Our computational grid is the same as the grids used in the DNS calculations by J.

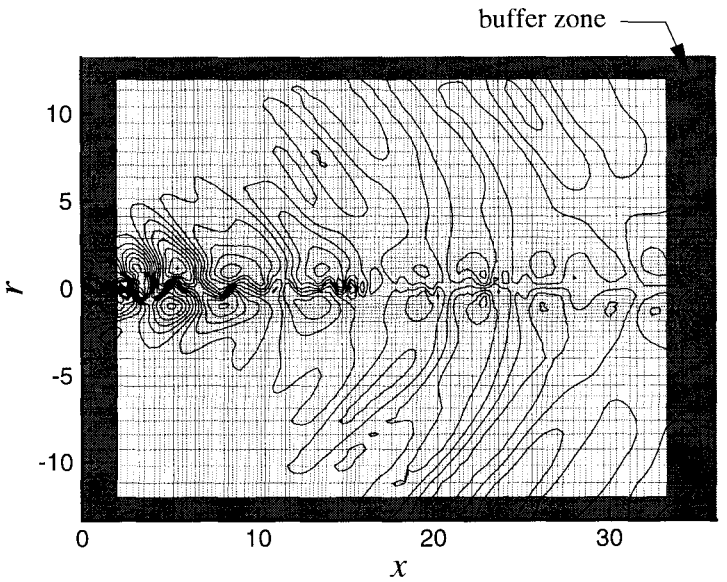

Figure 7.1 Computational domain and buffer zones.

Freund *et al.* [40], and are repeated here for completeness. The computational domain extends 13.3 jet radii in the radial direction and 36 jet radii in the axial direction; see figure 7.1. The DNS calculations were performed in a computational domain with 270 grid points in the radial direction, 640 points in the axial direction and 128 points in the azimuthal direction. In LNS calculations we focus only on the first two azimuthal modes only. Therefore, if the inflow boundary conditions are filtered to retain only the first two azimuthal modes on the inflow conditions, we need only 4 points in the azimuthal directions for LNS calculations. The grid spacing in the radial and axial directions are not as severe as the DNS calculations. This is due to the fact that there is no nonlinear convective term in the LNS equations, or cascade of energy to smaller scales. Therefore, the dominant smallest scales in the LNS calculations are coming from the inflow boundary and not from energy cascade to smaller scales in the DNS calculations. The computational mesh for the DNS calculation had $640 \times 270 \times 128$ points in the axial, radial, and azimuthal directions, respectively. We found that a full resolution calculation in the axial direction and a half resolution calculation in the radial direction provides accurate results without noticeable

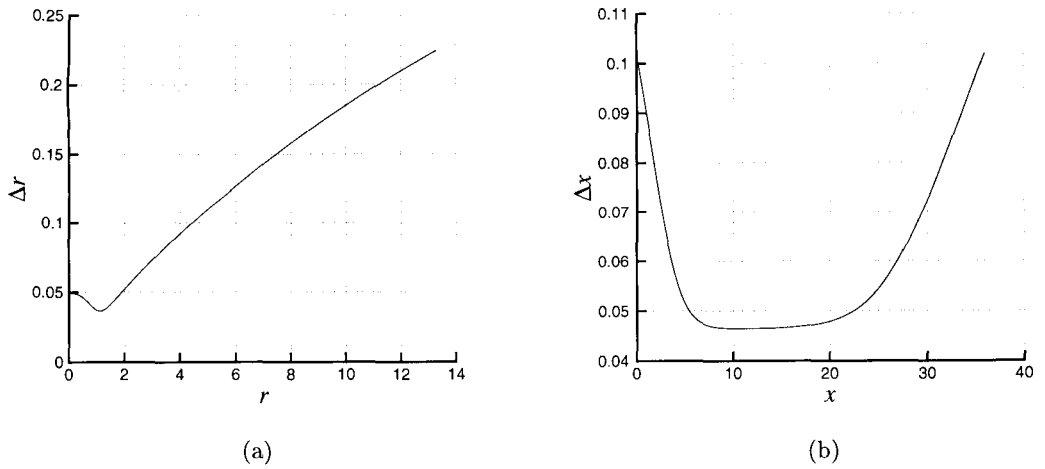

Figure 7.2 (a) radial grid spacing versus radial location, (b) axial grid spacing versus axial location.

reflection or saw-tooth wave errors. Calculations with half of the DNS resolutions in both axial and radial directions produce almost the same result. Therefore, in this study we report results in a computational domain with 640 points in the axial direction, 135 points in the radial direction, and 4 points in the azimuthal direction.

Radial Grid Stretching

The highest gradient in the flow quantities occur in the shear layer. Therefore, higher grid resolution is required in this region. The radial grid spacing distribution is shown in figure 7.2(a). The point-to-point change in mesh spacing is less than 2%, and the highest grid concentration occurs at $r = 1.15R$. In this direction (radial) the resolution is half of the DNS resolution. Since no physical vortex stretching is present in the linear calculations, the minimum scale size is limited to what is convected from the inflow boundary condition. Therefore, the minimum required resolution for the LNS calculations is less severe than for the DNS calculations. Insensitivity of our results to the adopted grid distribution was verified computationally.

Axial Grid Stretching

Since the mean flow gradients in the axial direction are not as high as is the radial direction, the axial grid spacing may be coarser than the radial grid spacing. In the axial buffer zones, particularly in the exit buffer zone, the axial grid spacing is rapidly increased. The axial grid spacing distribution is shown in figure 7.2(b). Similar to the radial direction the point-to-point change in mesh spacing was kept under 2%.

7.2.2 Coordinate Singularity Treatment

The treatment of the geometrical singularity in cylindrical coordinates has been a difficulty for many years in the development of accurate finite difference and pseudospectral schemes. A variety of numerical procedures for dealing with the singularity have been suggested. For comparative purposes, some of these are discussed in the appendix A, but the reader is referred to several books and review papers [12, 38, 50] for more detailed references.

Generally, methods discussed in the literature use pole equations, which are akin to boundary conditions to be applied at the singular point. The treatment of the pole as a computational boundary can lead to numerical difficulties. These include the necessity of special boundary closures for FD schemes (*e.g.*, [51]), undesirable clustering of grid points in PS schemes (*e.g.*, [57]), and, in FD schemes, the generation of spurious waves which oscillate from grid point to grid point (so-called two-delta or sawtooth waves, see [18, 155]).

In this study a method is used for numerical treatment of coordinate singularity, whereby singular coordinates are redefined so that data is differentiated smoothly through the pole, and we avoid placing a grid point directly at the pole. This eliminates the need for any pole equation. This technique is independent of the equations under consideration and was tested for several representative model problems. Despite the simplicity of the present technique, it appears to be an effective and systematic way to treat many scalar and vector equations in cylindrical and spherical coordinates.

A general description of this technique is given by Mohseni and Colonius [88] and in the appendix A at the end of this thesis, where solutions to compressible Navier-Stokes equations are compared with the techniques used in [83, 84, 43] (superposing a Cartesian coordinate system at the singularity). While we observed no detectable reflection in our

method from the coordinate singularity, the error in the Cartesian coordinate superposition method was dominated by reflections from the coordinate singularity. In all of the LNS calculations in this study we use this coordinate singularity treatment.

Transformation between the DNS and LNS Radial Grids

In the LNS calculations the coordinate singularity treatment of Mohseni and Colonius [88] was implemented. Therefore, the locations of radial grids in LNS calculations are different than in the DNS calculations. For this reason, one needs to transform all the flow data, inflow boundary conditions and mean flow distributions in the DNS calculations to the radial grids of the LNS calculations. This was done by using a fourth order compact Pade mid-point interpolation formula given by (see [64])

$$\frac{3}{10}f_{i-1} + f_i + \frac{3}{10}f_{i+1} = \frac{1}{20}\left((f_{i+\frac{3}{2}} + f_{i-\frac{3}{2}}) + \frac{3}{4}(f_{i+\frac{1}{2}} + f_{i-\frac{1}{2}})\right). \tag{7.22}$$

7.2.3 Boundary Conditions and Buffer Zones

The physical domain in a jet noise problem extends all the way to infinity. Therefore, an ideal computational domain should extend to infinity in all directions. Since an infinite computational domain is not possible, one needs to devise a different strategy. One approach is to employ a transformation that maps the infinite domain to a finite domain. However, this approach is not appropriate in traveling wave problems due to the lack of resolution for waves approaching infinity. A more practical technique is to truncate the computational domain at some distance away from the jet, which requires a boundary condition to close the numerical scheme at the boundary. The boundary condition at this artificial boundary is usually referred to as "nonreflecting" boundary conditions, as if there is no boundary.

Nonreflecting boundary conditions for acoustic waves and linearized Euler and Navier-Stokes equations have been considered by many authors, see for instance Giles [47], Thompson [149], Enquist and Majda [31, 32], Givoli [49], Tam and Webb [148], and Colonius *et al.* [22, 18]. A study of the performance of some of these nonreflecting boundary conditions are presented in the appendix C. For two-dimensional problems exact non-reflecting boundary conditions may be derived in Fourier space. This is done by modifying the dis-

persion relation so that any traveling wave with an incoming group velocity is prohibited. Since this modified dispersion relation is nonlinear, the nonreflecting boundary conditions in the physical domain are usually non-local in time and space. To obtain a local boundary condition, another level of approximation is required. If the original differential equation is nonlinear, a new set of approximations are introduced.

The performance of these boundary conditions is usually poor for the outflow boundary conditions of shear flows where the large vortical structures (as well as acoustic perturbations) are exiting the computational domain. Therefore, direct applications of the above mentioned boundary conditions would not work satisfactorily.

In order to reduce the acoustic reflections due to the passage of large vortical structures, Rai and Moin [113] and later on Colonius *et al.* [22] used an exit zone, where the grid spacing becomes coarse in the downstream direction, and filtering of the high frequency components or artificial viscosity is used to damp all the disturbances. However, excessive stretching produces spurious waves that might travel downstream into the main computational domain and contaminate the results.

A slightly different approach is to modify the governing equations in a non-physical buffer zone so that the outgoing disturbances are damped (cf [22, 56, 41]). With this technique one can add a convective term [135, 41] to equations in the buffer zone to accelerate the flow and make it supersonic. The advantage of a supersonic inflow/outflow boundary condition is that all the characteristics are incoming/outgoing and there would be no need to decompose any disturbance into incoming and outgoing parts. Freund [41] proposes a combination of basic techniques developed by Taasan and Nark [135] (adding a convective term) and Hu [56] (adding a damping term) that applies to both inflow and outflow boundary conditions. This technique is used in both DNS and LNS calculations.

The equations for the entire domain is written as

$$\frac{\partial \boldsymbol{Q}'}{\partial t} + U_x(x)\frac{\partial \boldsymbol{Q}'}{\partial x} + \frac{\partial \boldsymbol{E}'}{\partial x} + U_r(r)\frac{\partial \boldsymbol{Q}'}{\partial r} + \frac{\partial \boldsymbol{F}'}{\partial r} + \frac{1}{r}\frac{\partial \boldsymbol{G}'}{\partial \theta} + \boldsymbol{H}' = \boldsymbol{I}' - (\sigma_x + \sigma_r)\boldsymbol{Q}', \quad (7.23)$$

where U_x and U_r are the artificial convective velocities in the axial and radial directions, and σ_x and σ_r are the artificial axial and radial damping coefficients. Note that the target

U_{x0}	$1.15\ U_{r0}$	1.15			
σ_l	0.05	σ_r	2	σ_t	0.7
W_l	2.5	W_r	2.5	W_t	1.3
W_{σ_l}	2	W_{σ_r}	2.5	W_{σ_t}	1.3
β_{σ_l}	3	β_{σ_r}	3	β_{σ_t}	3
β_l	0.01	β_r	0.01	β_t	0.01

Table 7.1 Parameters for buffer zones

state for the LNS solver is the state of zero perturbation. A form with compact support in the buffer zone is chosen for U_x, U_r, σ_x and σ_r. We choose

$$U_x = U_{x0}\left(2 + \tanh(-f_l x) + \tanh(f_r(x - X_{max}))\right), \tag{7.24}$$

$$U_r = U_{r0}\left(2 + \tanh(-f_t(r + R_{max}) + \tanh(f_t(r - R_{max}))\right), \tag{7.25}$$

$$\sigma_x = \begin{cases} \sigma_r \left(\dfrac{x - (X_{max} - W_{\sigma_r})}{W_{\sigma_r}}\right)^{\beta_{\sigma_r}} & \text{if } \ x > X_{max} - W_{\sigma_r}, \\ \sigma_l \left(\dfrac{W_{\sigma_l} - x}{W_{\sigma_l}}\right)^{\beta_{\sigma_l}} & \text{if } \ x < W_{\sigma_l}, \end{cases} \tag{7.26}$$

$$\sigma_r = \left(\frac{r - (R_{max} - W_{\sigma_t})}{W_{\sigma_t}}\right)^{\beta_{\sigma_t}}, \tag{7.27}$$

where

$$f_l = \frac{\tan^{-1}\left(\frac{\beta_l}{U_{x0}} - 1\right)}{-W_l}, \qquad f_r = \frac{\tan^{-1}\left(\frac{\beta_r}{U_{x0}} - 1\right)}{-W_r}, \qquad f_t = \frac{\tan^{-1}\left(\frac{\beta_t}{U_{x0}} - 1\right)}{-W_t}. \tag{7.28}$$

The corresponding coefficients used in our computations are given in table 7.1. Spatial distribution of convective velocities and damping terms in the buffer zones are depicted in figures 7.3 and 7.4.

Inflow Boundary Condition

It is currently not computationally feasible to simultaneously simulate the nozzle flow as well as the small scale turbulence and the far-field acoustic waves by DNS of Navier-Stokes equations. Therefore, inflow conditions are used to mimic the essence of the shear layer

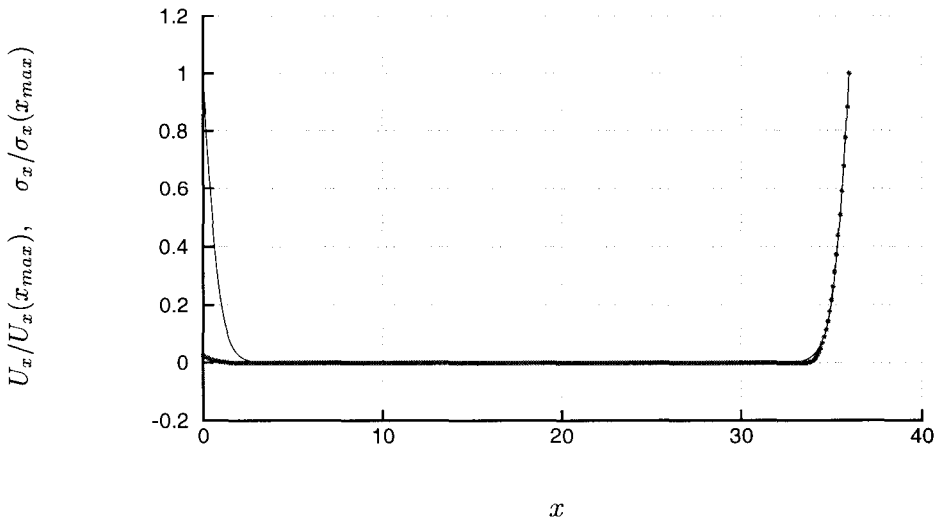

Figure 7.3 The axial distribution of axial convective velocity (———) and damping terms (•) in the buffer zones.

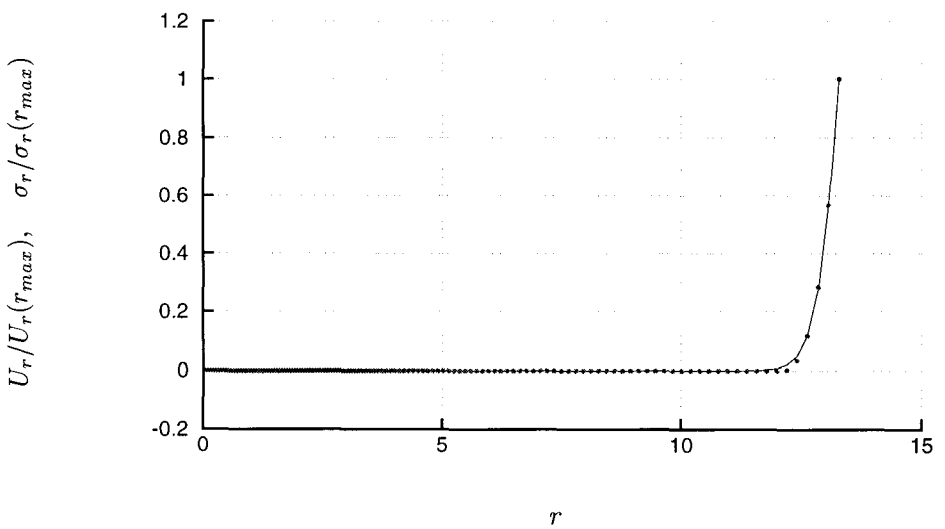

Figure 7.4 The radial distribution of radial convective velocity (———) and damping term (•) in the buffer zone.

right after it detaches from the nozzle. These conditions are the unsteady flow perturbation conditions prescribed at the nozzle exit and are implemented at every computational time step. In the simulations the inflow data is fed from a streamwise periodic jet simulation in [43]. This simulation had a streamwise period of $21R$. In order to decorrelate the turbulence of the incoming flow, the amplitude of the two-dimensional spectral components of the incoming waves were randomly jittered by up to 5% of their amplitude. The small scale turbulence statistics of DNS data are completely decorelated in our computational domain. While at high frequencies the flow statistics rapidly decorelates from the inflow forcing, we could still track the trace of $21R$ periodicity in our LNS calculations as well as DNS data at low frequencies (large scales). This is expected in free shear layers that are known to be sensitive to initial conditions, and will take them a long distance for large scales to decorelates in flow direction. The momentum thickness of the incoming flow is $\delta_m = 0.1R$.

To minimize the transitional calculations and reflections due to abrupt imposition of inflow boundary conditions at the beginning of the LNS calculation, the inflow condition was applied gradually through the application of a ramping function. In most of our calculations the applied inflow condition was at 99% of its original value after one acoustic time unit. Therefore, the inflow boundary conditions are turned on gradually by multiplying them by the factor $erf(2\frac{t}{T_r})$ where T_r is the time that 99.5% of the total inflow boundary conditions are on. In our calculations we choose $T_r = 1$.

To obtain the inflow boundary conditions at the calculational times of the LNS solver, the time sequence of the inflow data was interpolated in time by a cubic spline.

7.2.4 Mean Flow

The mean flow quantities are calculated from the DNS data. The mean axial velocity at $r = 0$ is shown in figure 7.5. It is clear that the potential core closes at around $x = 14$. Figures 7.6(a)–7.6(c) show the contour plots of the mean density, and the axial and radial velocities, respectively. The contour plots show the slow spreading of the jet. There are evidence of weak compression and rarefraction structures inside the jet before the potential core closes.

Profiles of the mean density, and the axial and radial velocity at different streamwise positions, are presented in figures 7.7(a)–7.7(c). The radial mean velocity is much smaller than the axial velocity. It is usually positive near the jet axis and it becomes negative at the upper edge of the shear layer where the entrainment process is active and for larger r it decays like $1/r$. The axial mean velocity in figure 7.7(b) shows the spreading of the jet from an almost top-hat profile to an almost Gaussian profile after the closing of the potential core.

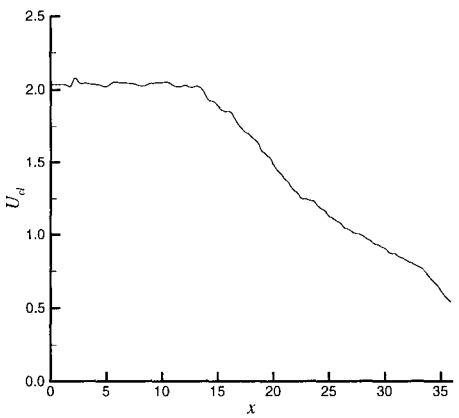

Figure 7.5 Mean flow axial velocity at $r = 0$.

7.3 Linear Theory of Supersonic Jet Noise

Following Liu [67], jet flow can be decomposed into three parts: mean flow, instability waves, and fine scale turbulence. The relative interaction between these modes are fully captured by the Navier-Stokes equations. Most of the linear theories attempt to capture the interaction between the instability waves and the mean flow. As the instability waves grow, they extract energy from the mean flow. But this energy transfer could happen in both directions. The growth of linear modes modifies the mean flow, and as the shear layer thickens, the instability wave growth rate decreases. Eventually, the shear layer is too thick to support unstable modes and the wave amplitude decreases until it dissipates.

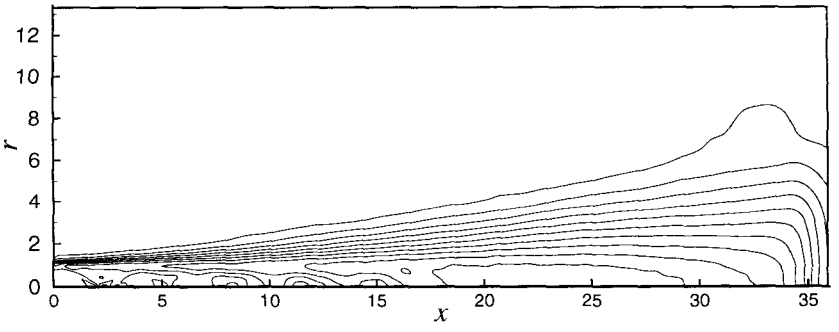

(a)

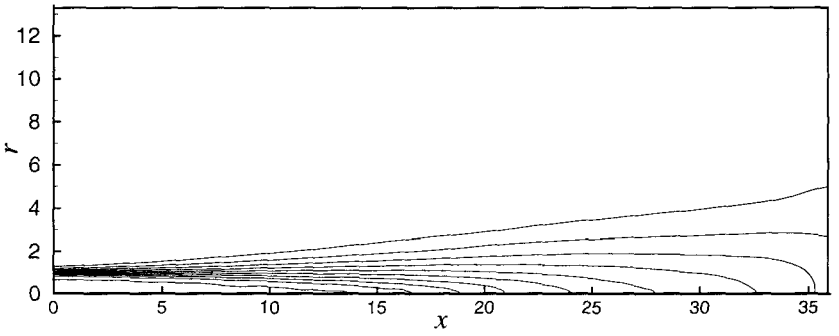

(b)

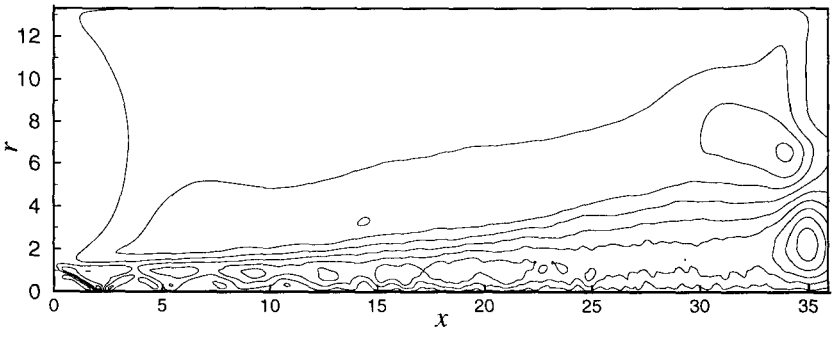

(c)

Figure 7.6 (a) Mean flow density contours: 11 contours between $0.8\rho_\infty$ and ρ_∞, (b) mean flow axial velocity contours: 10 contours between $0.2a_\infty$ and $2.0a_\infty$, (c) mean flow radial velocity contours: 9 contours between $-0.035a_\infty$ and $0.045a_\infty$.

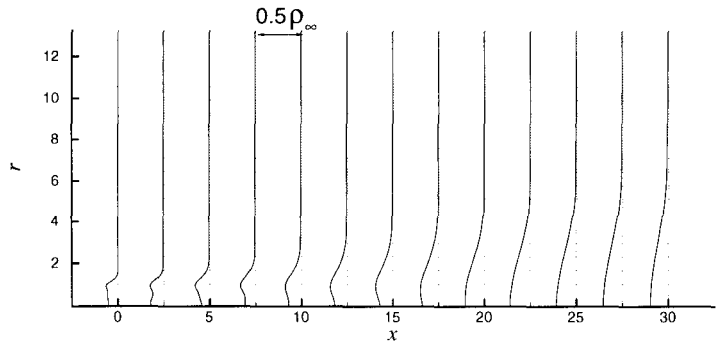

(a)

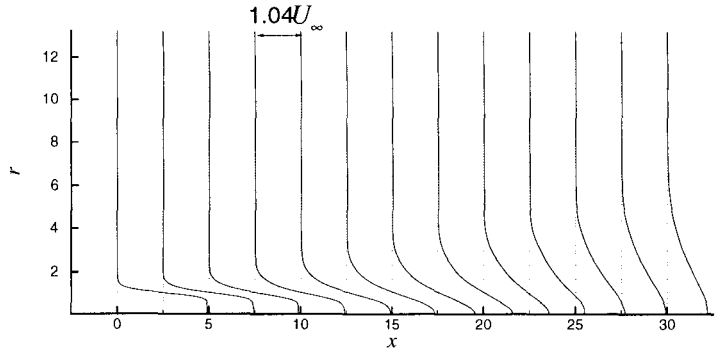

(b)

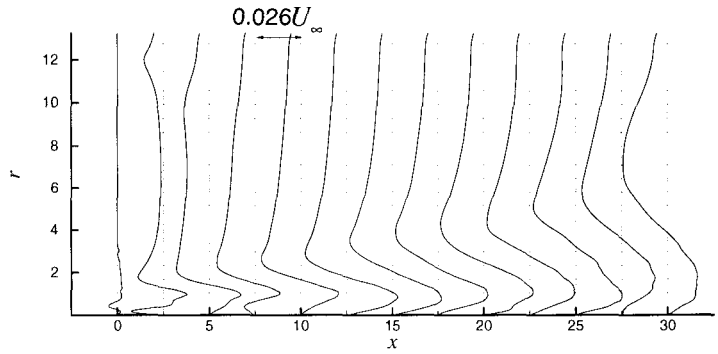

(c)

Figure 7.7 (a) Mean flow density profiles, (b) mean flow axial velocity profiles, (c) mean flow radial velocity profiles.

The linearized theory of high speed flows indicates that there are three distinct fluctuation modes with different characteristics: acoustic modes that are solutions of wave type equations, and vorticity and entropy modes which are simply convected by the flow. Entropy and vorticity modes are of parabolic type, while the acoustic modes are of hyperbolic type. The entropy and vorticity waves are convected downstream as a frozen pattern at the mean flow speed. Acoustic waves, on the other hand, propagate in all directions with sound relative to the mean flow velocity. If the disturbance level is very small and the base flow is at rest or in uniform motion, these modes may exist independently (see examples in appendix C). If the base flow is inhomogeneous or the disturbance levels are high, these modes are coupled and it is very difficult to separate them. Many approximate methods have been developed by neglecting some of these higher interactions. Their physical merits is a question that can be answered by comparison with direct numerical simulations or detailed experimental results. For larger fluctuation amplitudes, or in the presence of solid boundaries, one needs to account for the fluctuations produced by the interaction of the basic modes.

The classical stability theory of fluid problems is usually formulated as a set of eigenvalue problems. By assuming that the wave solutions decay exponentially to zero away from the jet, one ensures that the homogeneous boundary conditions are satisfied. However, this requirement of classical stability theory prevented the prediction of acoustic radiation. Tam and Morris [147] recognized that the classical solution based on the locally parallel flow approximation is only the first term in a multiple-scale expansion of the solution of a more rigorously formulated instability wave theory. Their method is similar to the method developed by Nayfeh and El-Hady [100] for non-parallel compressible boundary layers.

The multiple expansion of Tam and Morris [147] is the appropriate asymptotic expansion inside the jet. However, it is not uniformly valid in a region outside the jet. Subsequently, the method of matched asymptotic expansions was used to develop a uniformly valid instability solution for supersonic jets (see Tam and Burton [143]). Tam and Burton divided the physical domain into two regions: the jet flow and the near field around it, and the acoustic field outside the jet. While the slow variation of mean flow inside the jet in the axial direction (as compared to the radial direction) provides a natural small parameter for

a multiple-scale expansion, outside the jet there is no preferred direction and the multiple-scale solution would not be appropriate. Therefore, to obtain a uniformly valid instability solution to the supersonic jet noise problem, they constructed two independent asymptotic expansions of the linearized equations of motion. The slow spreading rate of the jet is considered as the small parameter in the expansion. Inside the jet and in the adjacent region outside it (inner solution), a multiple-scale asymptotic expansion is valid. In the region outside the jet all the way to the acoustic far field (outer solution), an outer expansion is constructed by the method of Fourier transform. In the outer solution the acoustic wave equations are used. Since these two expansions are the asymptotic expansions of the same solution but valid over different regions of the physical domain, there must be an overlapping region where both expansions are valid. Consequently, matching the expansions to the lowest order and the first order terms give the eigenvalue of the classical stability theory and the non-parallel flow corrections, respectively. This way the inner solution determines the pressure and velocity fluctuations associated with the instability waves inside the jet, while the acoustic near field outside the jet and the radiated noise in the far field are calculated from the outer solution. Subsequently, Tam *et al.* [145] argued that if the large-scale instability waves are the dominant sound sources of high speed jets, the frequency of the peak of the sound spectrum must be nearly equal to the frequency of the most amplified instability wave of the jet. Furthermore, the direction of the peak noise radiation must also be nearly equal to the direction of the Mach wave radiation of the most amplified instability wave.

In this section a review of the inviscid linear stability theory of compressible jets, as described by Tam and Burton [142, 143], is presented. The compressible Rayleigh equation is written as

$$\frac{\partial^2 \hat{p}}{\partial r^2} + \frac{\partial \hat{p}}{\partial r}\left[\frac{2\alpha}{\omega - \alpha\bar{u}}\frac{\partial \bar{u}}{\partial r} + \frac{1}{r} - \frac{1}{\bar{\rho}}\frac{\partial \bar{\rho}}{\partial r}\right] + \left[\bar{\rho}M_j^2(\omega - \alpha\bar{u})^2 - \frac{n^2}{r^2} - \alpha^2\right]\hat{p} = 0, \qquad (7.29)$$

where $\bar{\rho}$ and $\bar{u}$ are the mean density and velocity, respectively, M_j is the jet Mach number, α is the axial wave number, ω is the circular frequency, and n is the azimuthal mode number. The other perturbation eigenfunctions can be easily related to the pressure eigenfunction $\hat{p}$

through the following relations.

$$\bar{\rho}\hat{u} = -\frac{1}{(\alpha\bar{u}-\omega)^2}\frac{d\hat{p}}{dr}\frac{d\bar{U}}{dr} - \frac{\alpha\hat{p}}{\alpha\bar{u}-\omega}, \tag{7.30}$$

$$\rho\hat{v_r} = \frac{i}{\alpha\bar{u}-\omega}\frac{d\hat{p}}{dr}, \tag{7.31}$$

$$\rho\hat{v_\theta} = -\frac{n\hat{p}}{r(\alpha\bar{u}-\omega)}, \tag{7.32}$$

$$\hat{\rho} = -\frac{1}{(\alpha\bar{u}-\omega)^2}\frac{1}{\bar{\rho}}\frac{d\hat{p}}{dr}\frac{d\bar{\rho}}{dr} + \frac{\bar{\rho}\hat{p}}{\gamma p_0}. \tag{7.33}$$

Note that $\bar{c}^2 = \dfrac{\gamma p_0}{\bar{\rho}}$.

Equation (7.29) and its boundary conditions constitute an eigenvalue problem whose solution is the inviscid dispersion relation $\Omega(\omega, \alpha) = 0$. It is evident from this equation that the analytic nature of the solution depends on $\omega - \alpha\bar{u}$. $\alpha = \dfrac{\omega}{\bar{u}}$ defines a critical layer. For decaying modes there may not exist any continuous solution to the inviscid equations of parallel flow (see Betchov and Criminale [10], p. 80), and this is true for slowly diverging flows as well. Special treatment is required to continue the computations in this case, which will be discussed later.

Since the mean flow of the jet is assumed to be axisymmetric, the instability waves can be decomposed into the azimuthal modes. We assume that the flow is locally parallel and that the fluctuating pressure takes the form

$$p(r, \phi, x, t) = Re\left(A(x)\hat{p}(r)exp\left[i(\alpha x + n\phi - \omega t)\right]\right), \tag{7.34}$$

where $A(x)$ is the amplitude function. In the instability wave theory the assumption is that the noise characteristics of supersonic jets in the peak radiation direction are related to those of the most amplified instability waves. The growth rate of any wave is functionally dependent on the imaginary part α_i of the axial wave number α. The total amplification of an instability wave of azimuthal mode n and frequency ω is given by

$$G(x_N, \omega, n) = \int_0^{x_N} -\alpha_i(\omega, n)dx, \tag{7.35}$$

where x_N is the axial location at which $\alpha_i = 0$, *i.e.*, the wave becomes neutral. Therefore, by

calculating the growth rates for various frequencies and azimuthal modes, one can determine the most amplified wave.

The large scale velocity gradient across the shear layer causes the amplitude of the instability wave to grow. As the instability waves propagate downstream, the shear layer thickness increases, which leads to a reduction in mean velocity gradient and hence the growth rate. Eventually, at some point downstream the growth rate of the wave becomes zero. On propagating further downstream the wave becomes damped.

In comparing the predictions from the linear stability theory with the DNS data, experimental data or LNS data, it is important to recognize that the real flow data contain contributions from all scales of turbulence, including those from the small-scale structures, convective disturbances, and nonlinear interactions. The numerical predictions based on the linearized stability theory only calculates the noise associated with the linear interaction of large-scale coherent structures. It should be noted that at each frequency and azimuthal mode it is assumed that all the flow energy is captured by the most unstable instability wave. Therefore, the initial amplitude of the various modes is not known. These assumptions will be examined in later sections of this study.

The mean flow of a real jet is slowly diverging and is non-parallel. In the non-parallel case the inner solution to the stability equation can be represented as

$$p_{in}(r,\phi,x,t) = A(x)\hat{p}(r)exp\left[i(\theta x + n\phi - \omega t)\right], \tag{7.36}$$

where the slowly varying phase function is given by

$$\theta(x,\omega,n) = \int_0^x \alpha(x,\omega,n)dx, \tag{7.37}$$

and α, the local wave number, is the eigenvalue of the instability wave problem. Now if $\lambda_o(\alpha,\omega) = \sqrt{\alpha^2 - \rho_\infty M_j^2 \omega^2}$, then the pressure eigenfunction is normalized such that

$$\hat{p}(r,x,\omega,n) \rightarrow H_n^{(1)}(i\lambda_o r) \qquad \text{as} \quad r \rightarrow \infty. \tag{7.38}$$

In this boundary condition the branch cut corresponding to $-\pi/2 \leq arg\,\lambda_o \leq \pi/2$ should

be taken in the square root in the definition of λ_o to insure decaying solutions or outgoing waves as $r \to \infty$. The boundary condition around the axis of the jet is

$$\hat{p}(r, x, \omega, n) \to J_n(\lambda_j r) \qquad \text{as} \quad r \to 0, \tag{7.39}$$

where $\lambda_j(\alpha, \omega) = \sqrt{\rho_\infty M_j^2 \omega^2 - \alpha^2}$. J_n is the Bessel function of the first kind and order n.

In Tam and Burton's analysis [143] the non-parallel correction factor β is defined as

$$\beta(x, \omega, n) = \int_0^x \frac{I_2}{I_1} dx,$$

where I_1 and I_2 are defined in [143]. Subsequently, the amplitude of the instability wave A is related to β by

$$A(x, \omega, n) = \hat{A}(\omega, n) e^{-\beta(x,\omega,n)}. \tag{7.40}$$

We note that the amplitude of the wave at each frequency and azimuthal mode at the nozzle exit is still arbitrary.

Using the inverse Fourier transform the outer solution to the lowest order can be represented as

$$p_{out}(r, x, \phi, t, \omega, n) = \int_{-\infty}^{\infty} e^{i(\eta x + n\phi - \omega t)} \hat{A}(\omega, n) \hat{g}(\eta, \omega, n) H_n^{(1)}\left(i\lambda(\eta, \omega) r\right) \, d\eta, \tag{7.41}$$

where

$$\hat{g}(\eta, \omega, n) = \frac{1}{2\pi} \int_{-\infty}^{\infty} e^{i(\theta(x,\omega,n) - \eta x) - \beta(x,\omega,n)} \, dx. \tag{7.42}$$

Note that

$$\hat{g}(-\eta, -\omega, -n) = \hat{g}^*(\eta, \omega, n).$$

Since the inner and outer solutions are solutions to the same physical problem, although valid in different parts of the physical domain, we can properly match them to get a uni-

formly valid solution everywhere.

7.3.1 Stochastic Wave Model

An important assumption in Tam and Burton's theory [143] is that at each frequency they consider only a *single* instability wave as the representative of the major energy carrying wave component. However, in supersonic turbulent jets, particularly in high Reynolds numbers, there is a wide spectrum of instability waves. The interactions between instability waves generates harmonics. In Tam and Burton's theory these harmonics are neglected. In their theory where the growth and decay of a single frequency wave is followed, at maximum growth its harmonics are assumed to be small and have little impact on the noise generation.

In the stochastic wave model theory, the large scale turbulent structures are represented by a linear combination of instability waves of all frequencies and azimuthal modes. These large scale turbulent structures are assumed to be random. Therefore, the initial wave amplitude was taken as an appropriately normalized stochastic random function. This assumption was motivated by the argument that for high Reynolds number supersonic jets the turbulent flow near the nozzle exit has no intrinsic length or time scales. Consequently, the mean velocity profiles and turbulence statistics have self-similar characteristics. This lack of intrinsic scales may suggest that the spectrum of instability waves of the jet is generated by random excitation having no characteristic length or time scales. Therefore, the statistical properties of the random amplitude functions are determined by the no intrinsic length or time scale constraint on the instability wave spectrum at the nozzle exit. Then, the acoustic solution can be calculated for regions away from the jet using the Fourier transform. Application of the method of matched asymptotic expansions connect this acoustic solution to the instability wave solution. It was hoped that the dominant part of the turbulent mixing noise due to large scale structures would be determined by this method.

In summary, Tam and Chen [144] extended the single instability wave matched asymptotic expansions solution of Tam and Burton [143] to include a broad frequency spectrum in a stochastic model of supersonic jet noise from the large scale turbulent structures. Their calculated noise directivities for Mach 2 jets at different temperatures were in good agree-

ment with the measurements of Seiner *et al.* [123]. In their theory the large scale structures are represented by a superposition of its normal modes. It was assumed that the most important normal modes of jet flows were the instability wave modes. However, the small scale turbulence and nonlinear interaction of instability waves are usually not represented by these modes. Thus, there is still no inclusion of the small scale turbulence or nonlinear noise sources in the theory and its predicted sound field. Consequently, if $\mathfrak{E}_n$ is the n-th order eigenfunction of the instability waves, the pressure fluctuations associated with the large scale turbulent structures may be represented as

$$p(r,\theta,x,t) = \sum_{n=-\infty}^{\infty} \int a_n(\omega)\mathfrak{E}_n e^{i(n\phi-\omega t)} d\omega, \tag{7.43}$$

where n is the azimuthal mode number, ω is the angular frequency of the wave, and $a_n(\omega)$ is the relative amplitude of the instability wave. It was argued that since the large scale structures are not fully deterministic, $a_n(\omega)$ is taken to be a stochastic random function. Even though the relative order of different modes or frequencies are calculated in this theory, there was still an arbitrary scaling factor for the absolute amplitude of the disturbances.

7.3.2 Numerical Issues

We solve the Rayleigh equation (7.29) for the operating conditions of the DNS jet and for each azimuthal mode number and frequency. A fourth order Runge-Kutta scheme is used to integrate equation (7.29) from the outer edge of the jet shear layer inward and from the jet axis outward. The numerical solutions are matched somewhere in the shear layer (usually very close to $r = 1$) to find the unknown scaling coefficients. We set the determinant of the matrix equation for the coefficients equal to zero to get a nontrivial solution. This process is repeated iteratively for the wave number α until this condition is met. For damped supersonic waves (with $\alpha_i > 0$) we need to deform the integration contour in the complex r plane to avoid the critical point of the Rayleigh equation and its branch cuts. To continue the computations we need to evaluate the mean flow quantities away from the real axis into the complex r plane. In doing so we use the analytic continuation of the mean flow quantities into the complex plane. This might raise some difficulties when the mean flow

from the experimental data or the DNS data is used. It is not clear, in this case, how to accurately extend the mean flow away from the real axis. We have tried some different approaches (*e.g.*, cubic spline curve fit) to remedy this problem. However, we found that the mean flow quantities fitted to a simple equation is most reliable. In either case, one must correctly account for the branch cuts of the curve fitted equations.

7.3.3 Mean Flow Used in LST Calculations

It is well known that if the inviscid linear theory is implemented for calculating the instability waves in a developed region of a jet where the instability waves are damped, the calculation cannot be carried out completely in the physical plane along the real r-axis. Therefore, for disturbances that are neutrally stable or are decaying, when $\alpha_i \geq 0$, the numerical procedure described in the previous section must be modified due to the critical layer where the term $1/(\alpha\bar{u} - \omega)$ becomes singular. This happens when the disturbances become neutrally stable and the location of the critical layer in the complex r plane crosses from the lower-half plane into the upper-half plane (see figure 7.8). For an inviscid damped wave the value of the eigenfunction on the two sides of the branch cut along the real axis will not be the same, *i.e.*, the eigenfunction is not continuous at the branch cut. This branch cut for the inviscid flows represents a critical layer of infinitesimal thickness that can be smoothed out by introducing viscosity or any other diffusion mechanism. In order to avoid the critical point, the integration contour must be deformed into the complex r plane to pass over the critical point [147]. The indentation of the integration contour in the complex r plane lies on three straight lines joining the points $(Re(r_c) - r_s, 0)$, $(Re(r_c) - r_s, Im(r_c) + r_s)$, $(Re(r_c) + r_s, Im(r_c) + r_s)$, and $(Re(r_c) + r_s, 0)$.

Note that the mean flow is given only on the real axis. Consequently, we need to evaluate the mean flow for complex values of r to continue the integration along the deformed integration contour in the complex r plane. When the mean flow is given analytically, one can use the analytic continuation to obtain the mean flow away from the real axis. This is feasible for weakly damped waves. However, Tam and Chen [144] pointed out that for mean flows that are known only for tabulated points (experimentally or computationally), it is not clear how to reliably continue the mean flow to the complex r plane. Therefore,

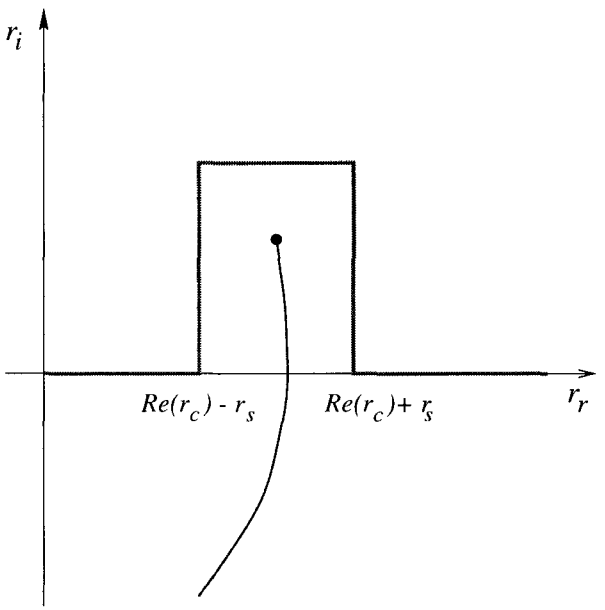

Figure 7.8 Deformed integration contour in the complex r plane for supersonically damped instability waves.

they recommended adding a turbulent eddy viscosity term to the instability wave equation. With turbulent viscosity terms added, the integration can be carried out completely along the real r-axis. However, we found that a reliable method is to fit an appropriately regular function to the computational mean flow. Branch cuts (for log function in our case) may then be evaluated in a straightforward way by using the appropriate Riemann sheet. To this end, we use

$$\bar{u} = \frac{U_{cl}}{\cosh^2\left(\frac{f}{1.15}\right)}, \tag{7.44}$$

where

$$f = \frac{r + 0.2 \log\left(\dfrac{\cosh\left(\frac{r}{0.2} - s\right)}{\cosh(s)}\right)}{2\delta},$$

$$s = 5\left(1 - \frac{\delta}{1.1}\right),$$

and

$$U_{cl} = 2.12757 - 0.02257x - 0.09559\log(\cosh(7.1 - 0.5x)) + 0.05046\log(\cosh(11 - 0.5x)),$$
$$\delta = 0.274284 + 0.08095x - 0.006102x^2 + 0.0003769x^3 - 5.64384 \times 10^{-6}x^4.$$

The mean density and the mean sound field are usually connected through the Crocco-Busemann relation

$$\bar{\rho} = \left[\frac{T_\infty}{T_0} + \left(1 - \frac{T_\infty}{T_0}\right)\frac{\bar{u} - u_\infty}{1 - u_\infty} + \frac{\gamma - 1}{2}M_0^2\left(\bar{u} - u_\infty\right)\left(1 - \bar{u}\right)\right]^{-1}, \tag{7.45}$$

where

$$M_0 = \frac{U_0}{c_0} = M_j\left(\frac{T_\infty}{T_0}\right)^{1/2},$$

and u_∞ is the nondimensionalized free stream velocity, *i.e.*, $u_\infty = U_\infty/U_0$, and density is only a function of the axial velocity.

7.3.4 Other Instability Modes

In the early eighties Oertel [103, 102, 104] studied the instability waves of hot supersonic jets. He found three families of instability waves, each having a distinct propagation characteristics and distinct wave pattern. Tam and Hu [146] considered the dispersion relation for compressible Rayleigh equation that indicates the existence of the same family of waves for high-temperature jets. They named them the Kelvin-Helmholtz (KH) instability waves, supersonic instability waves (SIW) and subsonic instability waves. The familiar KH insta-

bilities have a strong near field acoustic. The SIW observed by Oertel has a near acoustic field with an almost normal wavefront to the jet boundary. While the propagation speed (phase speed) of these waves is less than the KH instability waves, they still remain supersonic with respect to the ambient gas (hence, the near acoustic field). The subsonic instability waves are mainly confined inside the jet and they appear to have no near field acoustics. These waves are characterized by their cross-hatched pattern inside the jet and their subsonic propagation speed. Therefore, only the KH and the SIW are capable of generating noise. Tam and Hu's numerical studies [146] showed that for jet Mach numbers up to 2 and for jet-to-ambient temperature ratios up to 2.5, the Kelvin-Helmholtz instability waves are the dominant sources of jet mixing noise.

When the condition $u_j > a_j + a_\infty$ is not satisfied, there is no supersonic instability wave mode. While the KH instability waves have a single wave mode for each azimuthal wave number, the SIWs consist of a family of wave modes for the same azimuthal wavenumber.

An important difference between the KH and SIW is that the KH instabilities are of the inflexional type while the SIWs are not. Therefore, the KH instability waves are analytically continued into a corresponding family of damped waves, whereas the supersonic instability waves are continued into a family of neutral waves. That is, without adding the viscous effects (*e.g.*, adding eddy viscosity) the SIWs would not become damped as they propagate downstream. Therefore, to identify the most amplified wave it is essential to include eddy viscosity in the analytical model.

7.4 Signal Processing Techniques

It is useful in studies of acoustic far field to view the waves in frequency space. It is also interesting to view the growth and decay of individual instability waves in the near field. The signal processing issues of the DNS and LNS are considered in this section.

The inflow boundary conditions in Freund, Lele, and Moin's DNS calculations [42], used in this study, are generated by feeding data from a turbulent streamwise periodic jet simulation [43], with $21R$ periodicity. The amplitude of the two-dimensional spectral components of the incoming waves were randomly jittered by up to 5% of their amplitude

to suppress this periodicity. In our LNS simulation the same inflow boundary conditions are implemented.

Since the inflow boundary conditions are almost periodic we expect that the flow field of the LNS calculations will approach an asymptotically periodic state. The expectation is that this scenario would not occur for the DNS calculation, and the nonlinearity eliminates (decorrelates) any periodicity in the inflow conditions. For high frequencies and small scales statistics of the DNS data is decorrelated from the inflow periodicity. However, our calculations show that a periodic computational domain with $21R$ periodicity is not long enough to completely decorrelate low frequencies and large scale correlations. This is expected because shear layers are very sensitive to initial conditions and large scales and low frequency components need large computational domains to be completely decorrelated. In this section methods for extracting frequency spectra from the LNS and DNS data are considered. Due to the different nature of data in each case, different methods are used, and are discussed in the following sections.

Discrete Fourier Transform

Since the quasi-periodicity is quite evident in the LNS calculations, the Fourier spectra was calculated from the definition of Fourier integrals. Apart from the aperiodicity imposed on the inflow boundary condition (see section 7.2.3), nonperiodic behavior of the data can be caused by many other factors, including existence of signals with frequencies lower than that can be resolved over a specific duration of signal and also signals with frequencies higher than the Nyquist frequency of the sampled data.

The Fourier transform of a function $h(t)$ is calculated by

$$H(\omega_j) = \frac{1}{nT} \int_{t_s}^{t_s+nT} h(t) e^{i\omega t} dt, \tag{7.46}$$

and the inverse transform is computed by

$$h(t) = \sum_j H(\omega_j) e^{-i\omega_j t} \tag{7.47}$$

where $\omega_j = 2\pi j/T$, N is the number of samples in each period, and computations were

continued for n more periods after the numerical solution reaches a periodic state at $t = t_s$. We approximated the integral in equation (7.46) by a trapezoidal rule.

In signal processing of nearly periodic signals, extreme care must be taken to avoid the three main issues arising during the transformation. These are sufficient sampling intervals to represent the lowest existing frequency in the data, high sampling rate to represent the highest frequencies, and finally windowing techniques (or averaging techniques with same effects) required to compensate for the non-periodicity at the end of each period.

The spatial periodicity of the inflow data can be translated into temporal periodicity with a period $T = 21$. The total duration of the LNS data was limited to $3T$. The LNS calculations are at an almost periodic state after the first flow through the entire computational domain. Our numerical experiments show that even one period of the LNS data is enough to accurately calculate the spectra at the smallest frequency $1/21$ and increasing the period T does not affect the results significantly.

The LNS data is sampled with the time step of the LNS calculation. The sampling rate must be chosen higher than the maximum frequency in the data to compensate for the aliasing effect, that is the energetic part of the spectrum should be well below the sampling frequency to suppress aliasing effects. The sufficiency of the sampling rate can be checked a posteriori. The sampling rate of the LNS computations are $100\ \frac{R_0}{t^d a_\infty}$, which is well above the maximum frequency considered in this study.

Lomb-Scargle Periodogram

While the direct Fourier transform was quite accurate for calculating the frequency spectra of the evenly sampled data from the LNS computations, it was not reliable in the case of DNS data. This was due to several computational issues. Firstly, the DNS data is only quasi-periodic very near the inflow. Thus, truncation of the data at the end of the computational time interval leads to contamination of frequency spectra. Secondly, the DNS data were computed with a variable timestep, and there were a few patches of missing DNS data. The time interval between consecutive DNS data are plotted in figure 7.9. There are 2496 sampled data between computational times 156 and 352. Therefore, more than 9 periods of the inflow forcing is available for signal processing. This information is enough

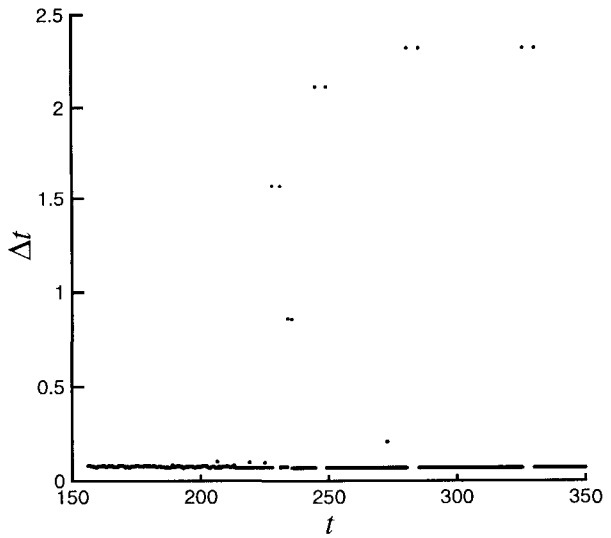

(a)

Figure 7.9 Time interval between consecutive DNS data.

to put limits on the minimum and maximum frequencies that can be extracted from the available data.

Many of the methods for evenly sampled data can still be employed in missing data problem after placing the data on an even-spaced grid, and interpolating or simply clamping the missing values at the last points. However, since the interpolation of an unevenly sampled data is equivalent to low-pass filtering, interpolation leads to an underestimation of high frequency components in a spectrum independent of the employed interpolation scheme (see, *e.g.*, Schulz and Stattegger [121]). Thus, an algorithm that restricts all calculations to actually measured values while at least yielding a similar resolution and efficiency of period detection would clearly be preferable.

An efficient technique that can be applied to unequally sampled data, which also includes regular time-series with missing values is the Lomb-Scargle periodogram (Lomb [69] and Scargle [120]). While in a Fourier decomposition of a data one can decompose the time-

series into a fundamental periodicity and a number of harmonics, a periodogram shows the power of each of these periodicities. The Lomb-Scargle periodogram was developed to detect weak periodic signals in noisy data obtained from astrodynamical observations. In fact, this algorithm was originally developed to overcome the problems caused by missing data and uneven sampling, resulting from restricted times for astronomical observations, planetary movements, and weather conditions. The Lomb-Scargle method also has the benefit of providing an easy way to calculate the levels of statistical significance of peaks in the periodogram (Scargle [120] and Horne and Baliunas [55]).

The rational underlying the Lomb-Scargle periodogram is very straightforward: the maximum in the Lomb-Scargle periodogram occurs at the same period of a sinusoidal wave that minimizes the sum of squares in a fit of the data. The Lomb-Scargle periodogram is based on the general transform theory which shows that the projection of a signal $y(t)$ onto an element of an orthogonal base $b_i(t)$ is the coefficient c that minimizes the mean squared error energy, defined as the integral over the definition interval of the squared differences between $y(t)$ and $c \cdot b_i(t)$. The Lomb-Scargle method implements this minimization over unevenly distributed sampled data of $y(t)$ considering the basis functions are the Fourier kernel.

For a time series of n data points $y_j = t(t_j)$ at times t_j; $j = 1, 2, \cdots n$, with mean $\bar{y}$ the Lomb-Scargle periodogram was computed from:

$$P(\omega) = \frac{1}{\sigma^2} \left\{ \frac{\left(\sum_j (y_j - \bar{y}) \cos \omega(t_j - \tau)\right)^2}{\sum_j \cos^2 \omega(t_j - \tau)} + \frac{\left(\sum_j (y_j - \bar{y}) \sin \omega(t_j - \tau)\right)^2}{\sum_j \sin^2 \omega(t_j - \tau)} \right\}, \tag{7.48}$$

where τ, introduced to adjust for phase-shifts caused by unequally spaced data [69] and to ensure time invariance of the periodogram, is defined by

$$\tau = \frac{1}{2\omega} \tan^{-1} \left\{ \frac{\sum_j \sin 2\omega t_j}{\sum_j \sin 2\omega t_j} \right\}. \tag{7.49}$$

For all periods T, P gives the normalized power as a function of angular frequency $\omega = 2\pi/T$. Note that this power is normalized with respect to the total variance of the data, $\sigma^2 = \sum_j y_j^2/(n-1)$, which allows determination of the statistical significance of peaks in the

periodogram. The dimensionless power P is proportional to the total power of a sinusoid at angular frequency ω that best fits the time series in the least-squares sense. A fast algorithm for calculations of the Lomb-Scargle spectrum was presented by [111, 112] and was used in our calculations.

To increase the resolution in computations of the height and position of peaks, the program allows oversampling of periods at intervals smaller than the average sampling interval of the input data. In all of our calculations an oversampling factor in the range from 4 to 5 was used.

Another problem might arise from the spreading of power from strong periodic components to other frequencies (leakage of power). A way to check for this problem is to remove the dominant peak from the data and repeat the Lomb-Scargle periodogram. If peaks in the original periodogram are highly affected by side-lobes, they should vanish if only residuals are used as new data points.

Since the sampling theorem applies only to evenly sampled data, the Nyquist frequency cannot be given for unevenly sampled data. In this situation, an average Nyquist frequency can be defined as

$$\bar{f}_N = \frac{1}{2\overline{\Delta t}}, \tag{7.50}$$

where $\overline{\Delta t}$ is the average sampling interval. Usually choosing the maximum studied frequency to be this average Nyquist frequency results in a conservative choice of frequency range. The average Nyquist frequency for the available DNS data is almost 13, and is well above the frequencies considered in this study.

Chapter 8

Results

In this chapter we analyze Mach wave radiation mechanisms in a fully expanded supersonic jet. Our primary goal is to quantify the relation between linear stability modes and Mach wave radiation, thereby elucidating the importance of nonlinear mechanisms in noise generation. A detailed comparison of the fully nonlinear (Navier-Stokes) along with the corresponding linear equations (LNS) is presented in this chapter. The sound pressure level (SPL) of the DNS and LNS data are reported in the next section. Instantaneous Fields are considered in section 8.2. In section 8.3 the possible contamination of the data by low frequency drift in DNS calculation is investigated. Amplification rates and mode shapes for particular frequencies from the DNS data is contrasted with the LNS and LST results in section 8.4.

LST calculations suggest that for cold jets the first two azimuthal instability waves dominate the acoustic field. This is verified for the DNS data in the following section, where the sound contributions of all other azimuthal modes was observed to be a small fraction of the sound fields of modes zero ($n = 0$) and one ($n = 1$). For this reason, in what follows we focus our calculations on these two azimuthal modes.

8.1 Sound Pressure Level

We begin by computing the sound pressure level (SPL) of the DNS and LNS data in the near acoustic field ($r = 12$) which is the maximum radius from the jet centerline for which the DNS results are available. The result of this computations are presented in figures 8.1 and

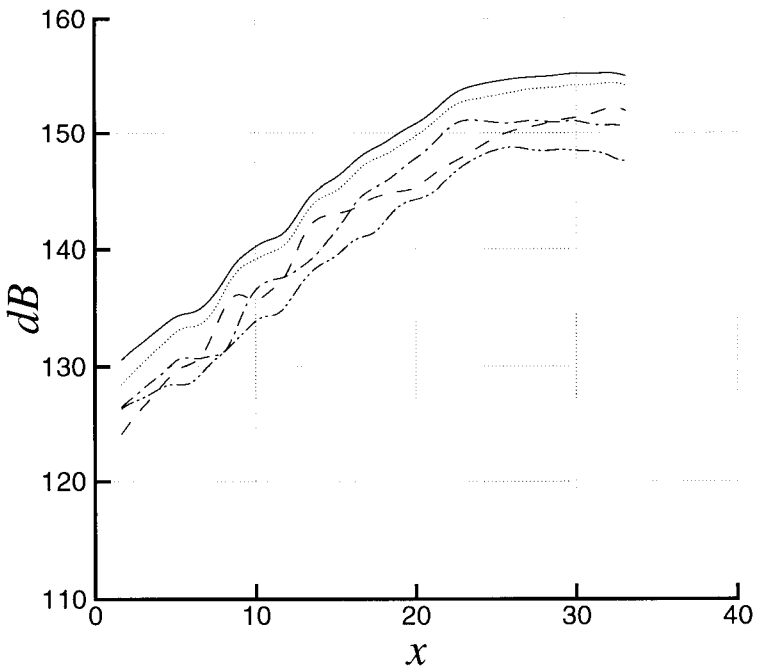

Figure 8.1 SPL of DNS at $r = 12$. (———) total; (- - - -) azimuthal mode zero; (—·—) azimuthal mode one; (·····) modes zero and one; (—··—) total minus modes zero and one.

8.2 for both DNS and LNS. As discussed in section 8.3, low frequency "drift" in the DNS data can potentially contaminate the calculation of SPL and frequency spectra. For the DNS data presented in this section, any drift for each individual mode was approximated by a fifth order polynomial in time at each spatial location and then subtracted from the data prior to SPL calculations. However, this procedure had negligible effect on the DNS results at $r = 12$.

There are several features to note in these figures. First, the acoustic field of the DNS data is dominated by modes zero and one, with contributions from the other azimuthal modes limited to at most 1.5 dB. This confirms the predictions from LST that the acoustic field of a cold jet (and relatively cold jets) is dominated by the first two modes [145]. Because of this, we limit our attention in what follows to only the first two modes. Second,

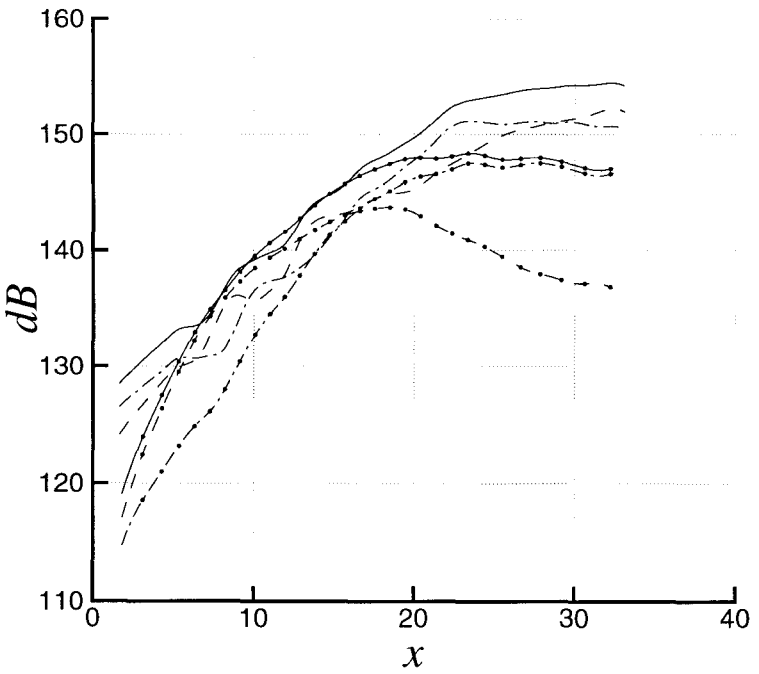

Figure 8.2 SPL at $r = 12$. For DNS: (———) sum of modes $n = 0$ and 1; (- - - -) $n = 0$; (— · —) $n = 1$, and for LNS: (—•—) sum of modes $n = 0$ and 1; (- -•- -) $n = 0$; (—•—) $n = 1$.

in agreement with predictions from LST, reported in the literature (*e.g.*, Tam *et al.* [145]), the azimuthal mode $n = 1$ in the LNS calculation contributes the most to the total SPL and is clearly the dominant part of the generated noise. However, the same trend is not observed in the DNS data. The maximum SPL of the DNS data for $n = 0$ is slightly higher than that of mode one, that is, mode zero is quite significant in the DNS calculation and cannot be ignored, while in the LNS calculations considering only $n = 1$ provides a good estimate for the maximum SPL by linear mechanisms. Third, one can observe that contrary to the LNS and LST calculations, the SPL of the DNS data for $n = 0$ peaks farther downstream than that for $n = 1$. This can be interpreted to mean that the location of the sound sources of mode zero of the DNS calculation is concentrated further away from the nozzle. Since the inflow data for both LNS and DNS are exactly the same, this effect cannot be attributed

to any artificiality of the inflow forcing.

In both LNS and DNS, the acoustic field is highly directional. For $n = 1$ the general directivity profile is well captured, while its SPL is underestimated by 4 dB. The agreement deteriorates significantly for $n = 0$, where LNS data represents a poor model for the maximum SPL as well as the directivity profile. Nevertheless, since the azimuthal mode one contributes the most to the SPL of the LNS calculations, the total directivity of the LNS data follows the trend of the total SPL of the DNS calculation. Thus, while the directivity of the sound field is captured well, the maximum SPL of the sum of modes $n = 0$ and 1 is underestimated by as much as 8 dB in the LNS calculation. This indicates that there are strong sound sources that are not captured in by linear equations. Sound sources due to nonlinear effects must apparently be included for a complete model of Mach wave radiation.

Note that the comparison of SPLs of the DNS and LNS data is performed outside the jet, *i.e.*, in the near acoustic field at $r = 12$, where the role of nonlinear effects is limited to steepening of the Mach waves. Such steepening produces an enhanced dissipation that acts to attenuate the sound. The Mach wave radiation in the present flow was, in fact, observed to involve significant wave steepening [42]. Therefore, one might expect a somewhat better agreement between DNS and LNS ate larger distance from the jet. Nevertheless, an 8 db difference at $r = 12$ indicates strong differences in the sources of sound between the DNS and LNS, and these will persist into the far acoustic field.

The jet considered in this study is at a low Reynolds number, where the inertial range of scales is limited to a small band of wavenumbers. Evidence from frequency spectrum will be provided later that shows that the difference for $n = 0$ cannot be attributed to the lack of small scale turbulence in the LNS, and we conclude that the 8 dB difference between LNS and DNS calculations can be attributed to nonlinear noise generation mechanisms acting on the large scales.

Now that we found the total SPL to be underestimated to some extent by the LNS computations, in the next three sections we compare the instantaneous pressure fields and the individual eigenfunctions and amplification rates at various locations in the LNS calculations with the DNS data to analyze in more detail the extent of validity of linear approximation.

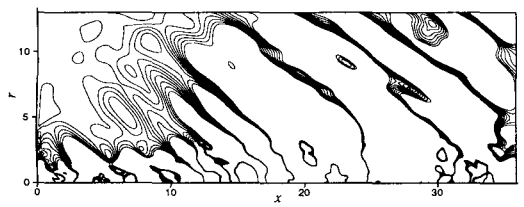

(a) DNS, $n = 0$

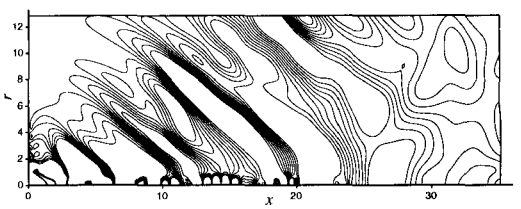

(b) LNS, $n = 0$

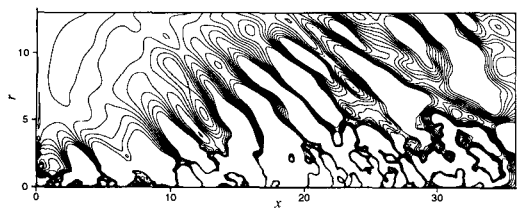

(c) DNS, real part of $n = 1$

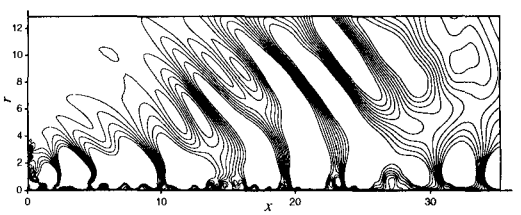

(d) LNS, real part of $n = 1$

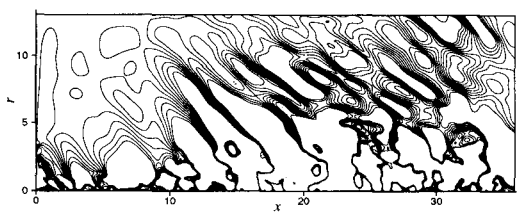

(e) DNS, imaginary part of $n = 0$

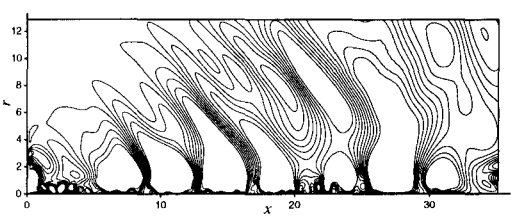

(f) LNS, imaginary part of $n = 1$

Figure 8.3 Instantaneous perturbation pressure field from DNS and LNS at time 222. No attempt was made to remove the drift in the DNS data. 10 contour levels between -0.00225 and 0.00225.

8.2 Instantaneous Fields

Instantaneous pressure fields of the DNS and LNS data for $n = 0$ and 1 are shown in figure 8.3. There is a clear region of agreement between DNS and LNS perturbation fields for both modes very close to the inflow boundary. A reasonable correlation over the entire acoustic region is observed for $n = 1$, which matches the results of the SPL given in the previous section. The correlation between the near field of LNS and DNS data is more persistent for

$n = 1$ than it is for $n = 0$, and in both cases gradually deteriorates as we move downstream in the jet. In the near field, especially, this is to be expected, since we are instantaneously observing all frequencies all together, and clearly DNS data has a much richer spectrum. This is evident in the DNS data of figures 8.3(a,c,e) as more moderate and smaller scales are observed that are absent in the LNS calculations of figure 8.3(b,d,f). Consequently, around the end of the potential core the LNS calculation is not a good representative of the rapid hydrodynamic fluctuations in the DNS data, which are not simulated by the LNS equations. However, it seems that the LNS computations capture some of the Mach wave radiations that mainly originate from the early stages of the shear layer (away from the end of the potential core).

It seems that the highest amplitude Mach wave radiation for $n = 0$ of the LNS data in figure 8.3 originates from an area close to the inflow boundary (close to the nozzle exit) while for $n = 1$ it radiates from a region around $x \approx 7$ and extends beyond the end of the potential core. This clearly affects the directivity of the near acoustic field for $n = 0$ and 1. While a far-field observer will not distinguish this small shift in the location of the apparent source, an observer at $r = 12$ would clearly sense it, as is evident in figure 8.2, where the SPL of the zero azimuthal mode of the LNS data at $r = 12$ saturates earlier that that of mode one.

LNS computations give the expected picture from the linear stability theory. The radiated Mach waves appear to be more localized for LNS. On the other hand, the DNS appears to have contributions from several regions, for both modes. We suspect that if we compared SPL for $n = 1$ further downstream (beyond the presently available computational region) it would start to disagree substantially from the DNS, and shows similar behavior as mode $n = 0$.

In figure 8.4 spacetime plots of the perturbations pressure fields at the radial coordinate $r = 1$ are shown for azimuthal modes zero and one. For both azimuthal modes, there are many structures traveling with a preferred convective velocity that can be predicted from the figure to be around one. This is consistent with the isentropic convective Mach number calculated from [107] for the flow conditions of this study.

The supersonic nature of the convective velocity of these structures is responsible for

Mach wave radiation. It is interesting to note that the breakdown of these organized structures in the shear layer around the end of the potential core in DNS data corresponds to the strongest regions of acoustic sources (see figures 8.13 and 8.14). This is in agreement with the theoretical predictions that the strongest noise sources are from this region where convective structures break down. The level of noise sources drops rapidly after the end of the potential core. However, the convective Mach number appears to be constant.

So far we have only compared the LNS and DNS data for quantities that have the accumulative effects over all frequencies. It is quite possible that for both modes, the linear stability modes do exist in the DNS data and correctly predict the sound radiation from the instability waves near the shear layer region. But in both cases, it appears that there are additional sources downstream (these may occur fairly far downstream) and thus it is hard to make any conclusions, since all the data is truncated around $x = 33$. To pursue this idea one really needs to look at individual frequencies. The reason for this is that it could be that the frequencies that are most amplified in DNS are well predicted by LNS, but that other frequencies (primarily higher frequencies) are contaminating the picture because we have only looked at root mean square values and instantaneous views so far. In section 8.4 we decompose the data in the frequency domain to characterize the agreement between the DNS and LNS data at each frequency component.

8.3 Low Frequency Artifacts of Individual Frequency Components

A drift (or trend) is defined as an amplitude variation in the time series which has a periodicity much longer than the time interval of the available data, normally with a frequency below $1/2(t_{max} - t_s)$. If there is a drift in the time-series the mean level of data changes over time, and the time-series would be non-stationary. In order to compute accurate frequency spectra, any drift in the data must be removed before using the discrete Fourier transform or the Lomb-Scargle periodogram techniques discussed in section 7.4.

While the DNS calculations were performed in the same computational domain as the LNS calculations, the results were not saved as frequently for the whole domain and only the

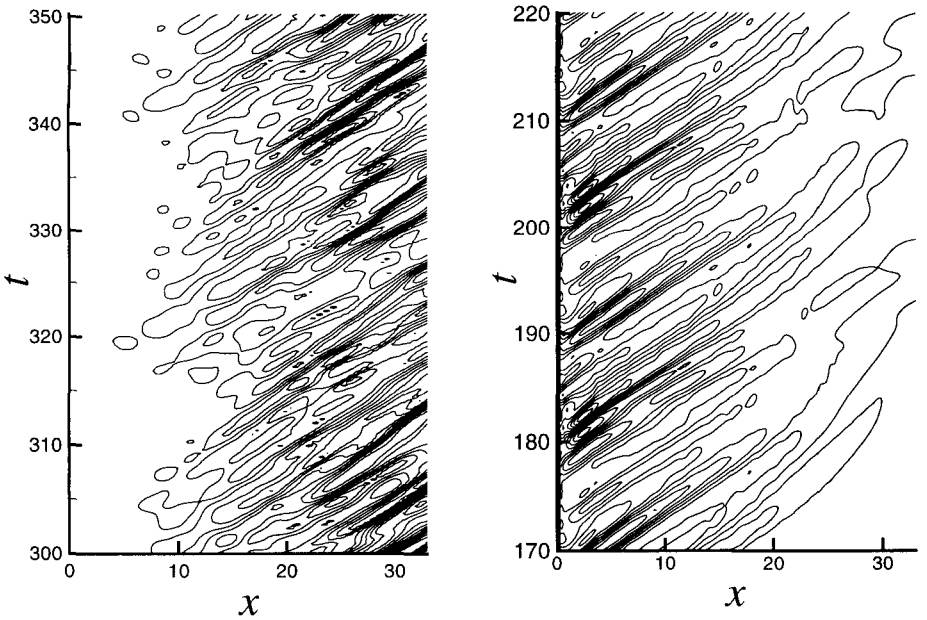

(a) DNS, $n = 0$

(b) LNS, $n = 0$

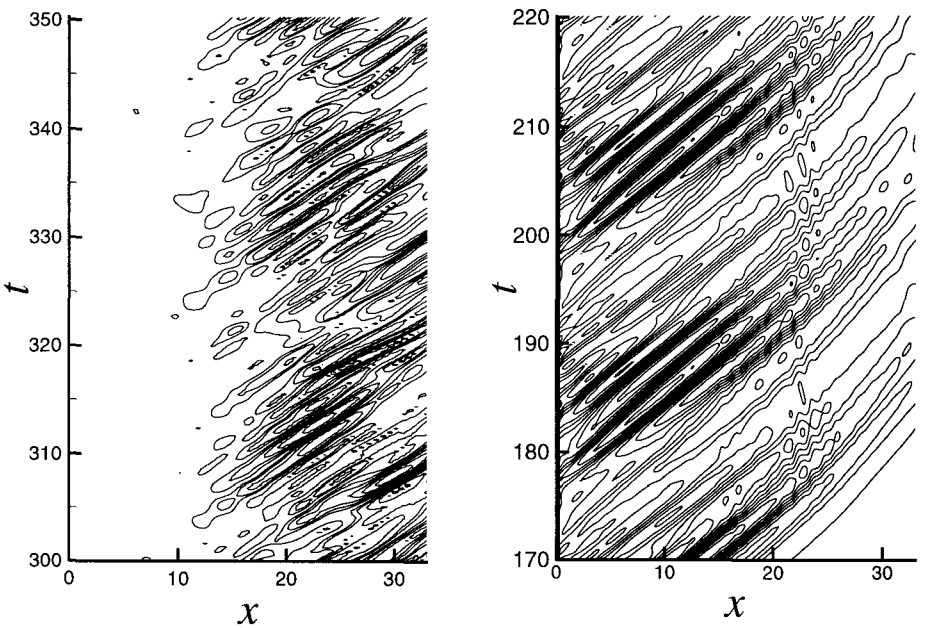

(c) DNS, $n = 1$

(d) LNS, $n = 1$

Figure 8.4 Space-time diagram showing the convection of large structures for azimuthal modes zero and one.

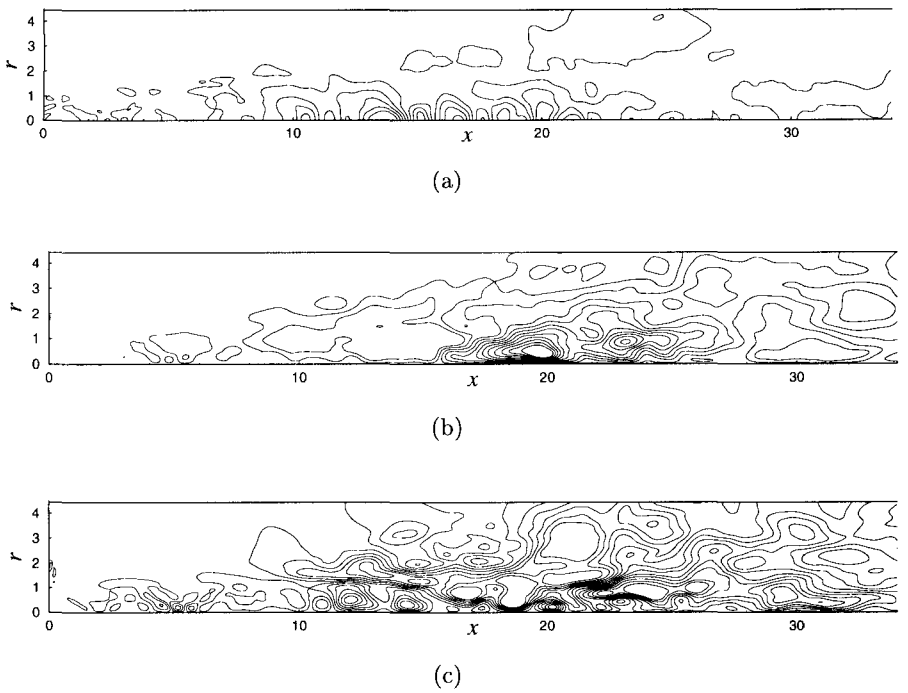

Figure 8.5 Drift in the DNS data at time 222. (a) $n = 0$; 8 contour levels between -0.0125 and 0.0225, (b) real part of $n = 1$; 12 contour levels between -0.0015 and 0.0095, (c) imaginary part of $n = 1$; 12 contour levels between -0.0015 and 0.0095.

part of the computational domain with $r \lesssim 4.4$ and $r = 12$ was saved regularly. To calculate the mean flow or possible drift in the data we need a time history of the flow quantities at each point. Therefore, we could only calculate the drift in the flow quantities for the part of the computational domain where the data was saved regularly, *i.e.*, for $r \lesssim 4.4$, and $r = 12$. In order to eliminate drift, a fifth order polynomial in time is fitted to each azimuthal mode at all spatial locations for the pressure field. Then this drift is subtracted from the original data, and the result is used in SPL and frequency spectra calculations. The drift calculated for the DNS data for $n = 0$ and 1 are presented in figure 8.5 at time 222. While the level of the drift in the data is small for both modes, $n = 0$ has considerably larger drift. It appears that the drift has its maximum effect around the end of the potential core. It is clear from figure 8.5 that the drift does not have a strong effect on the near acoustic field, consistent

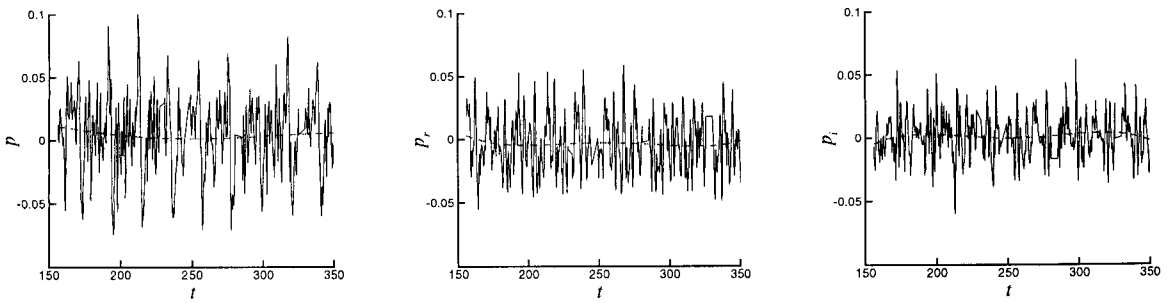

(a) (b) (c)

Figure 8.6 Drift in the pressure disturbance of the DNS data at $x = 15$ and $r = 1$, (a) $n = 0$, (b) real part of $n = 1$, (c) imaginary part of $n = 1$. (———) disturbance; (----) drift.

with our results in section 8.1 for $r = 12$. The time history of the drift at a typical point at the end of the potential core and inside the shear layer ($x = 15$ and $r = 1$) is shown in figure 8.6.

To remove the contaminating effect of the drift, particularly for $n = 0$, we subtract the calculated drift at time $t = 222$ from the DNS results in figure 8.3 to obtain the new near field in figure 8.7. Note that the level of the existing drift at time 222 in the DNS data is much smaller than the maximum acoustic level depicted in figure 8.7. In the rest of this chapter all the calculated results from the DNS data are reported after subtracting the appropriate drift from the original data.

8.4 Amplification Rates

So far we have only compared the LNS and DNS data for quantities that have the accumulative effects over all frequencies. In this section we decompose the data in the frequency domain to characterize the agreement between the DNS and LNS data at each frequency component.

Frequency spectra of pressure perturbations of the DNS data inside the shear layer at

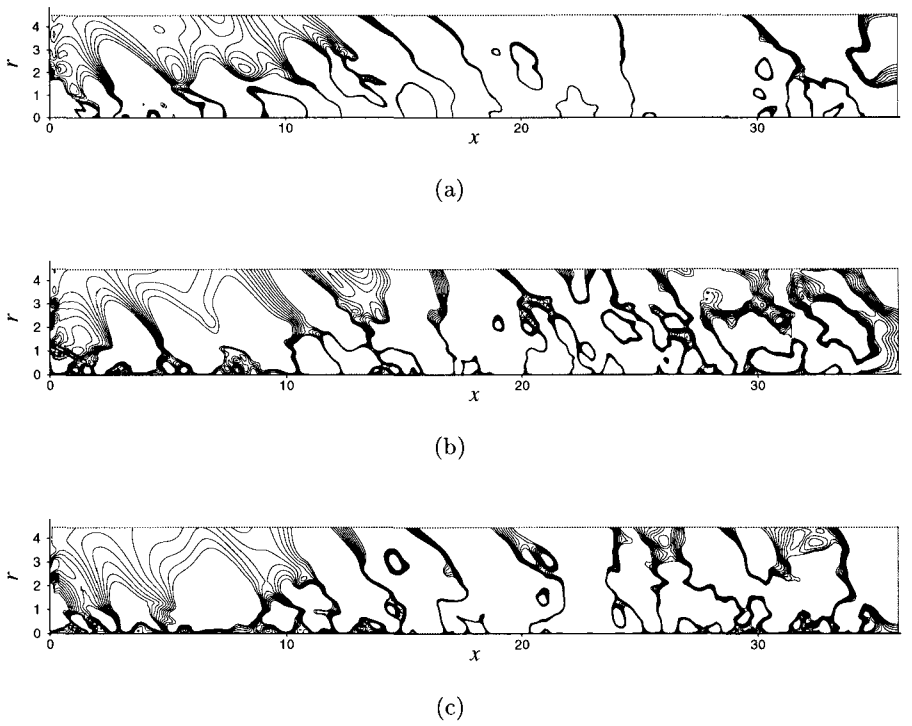

Figure 8.7 Instantaneous perturbation pressure field from DNS at time 222. Drift in the data was calculated by fitting a fifth order polynomial in x to the data and then subtracting it from the data. 10 contour levels between -0.009 and 0.009. (a) azimuthal mode zero, (b) real part of azimuthal mode one, (c) imaginary part of azimuthal mode one.

$r = 1$ and axial locations $x = 2, 10$, and 20 are shown in figure 8.8. The frequency spectra at $x = 2$ is dominated by intermediate frequencies around $St \approx 0.25$. These spectra show that while the overall amplitude of the spectra increases in the downstream direction, there is a clear energy transfer to lower frequencies. The same continuous shift of perturbation fluctuations toward lower frequencies with downstream location was reported in experiments by Troutt and McLaughlin [152].

The spatial development of the pressure disturbances at various Strouhal numbers (fD/U_j) in the DNS calculation is compared with the instability waves of the LNS calculation in figure 8.9 and 8.10 for $r = 1$ and $r = 4$. A study of these figures reveals that

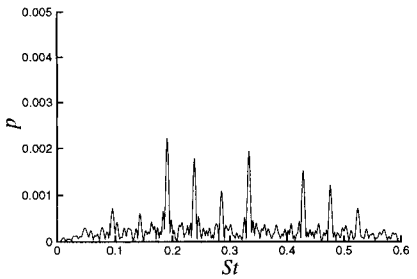

(a) $x = 2, n = 0$

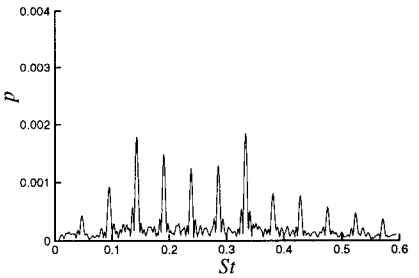

(b) $x = 2, n = 1$

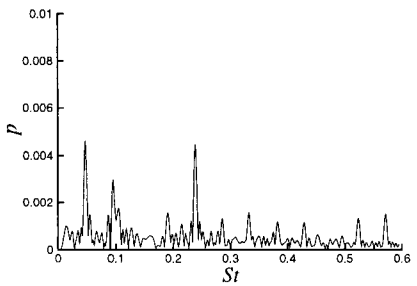

(c) $x = 10, n = 0$

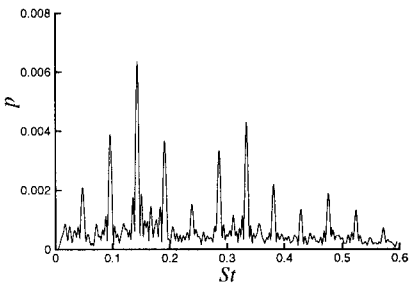

(d) $x = 10, n = 1$

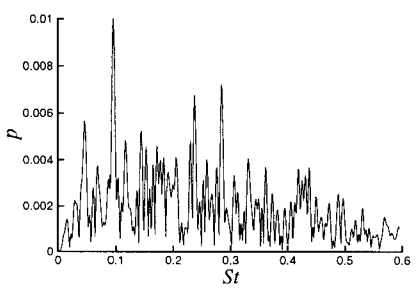

(e) $x = 20, n = 0$

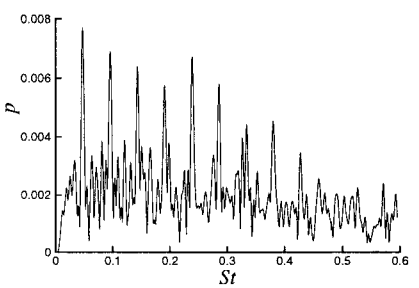

(f) $x = 20, n = 1$

Figure 8.8 Perturbation pressure spectra of DNS data at several axial locations in the jet shear layer at $r = 1$.

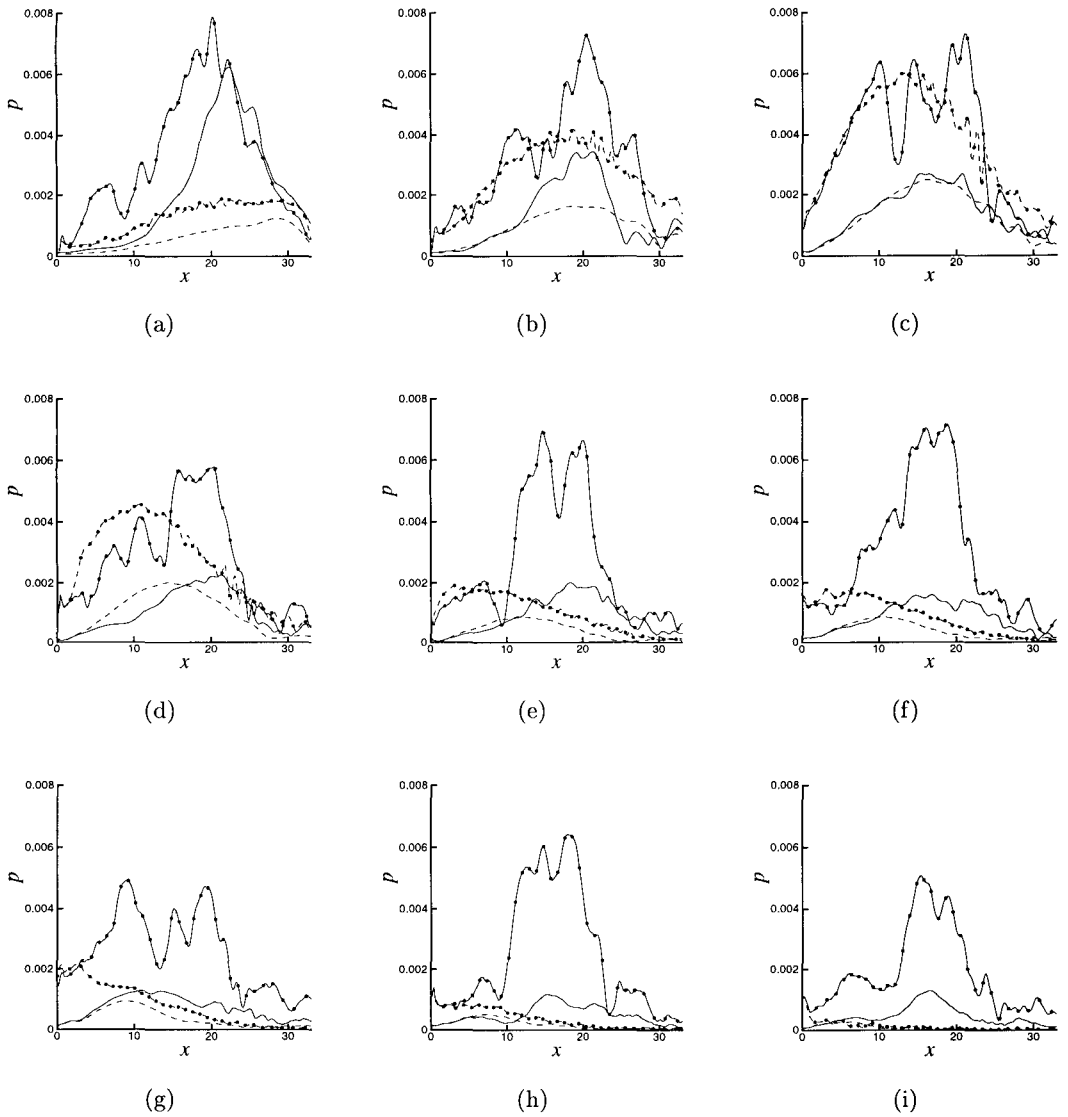

Figure 8.9 Perturbation pressure field for $n = 1$ for (a) $St = 0.048$ (b) $St = 0.095$ (c) $St = 0.143$ (d) $St = 0.191$ (e) $St = 0.238$ (f) $St = 0.286$ (g) $St = 0.333$ (h) $St = 0.381$ (i) $St = 0.429$. (—●—), DNS at $r = 1$; (- -●- -), LNS at $r = 1$; (——), DNS at $r = 4$; (- - - -), LNS at $r = 4$.

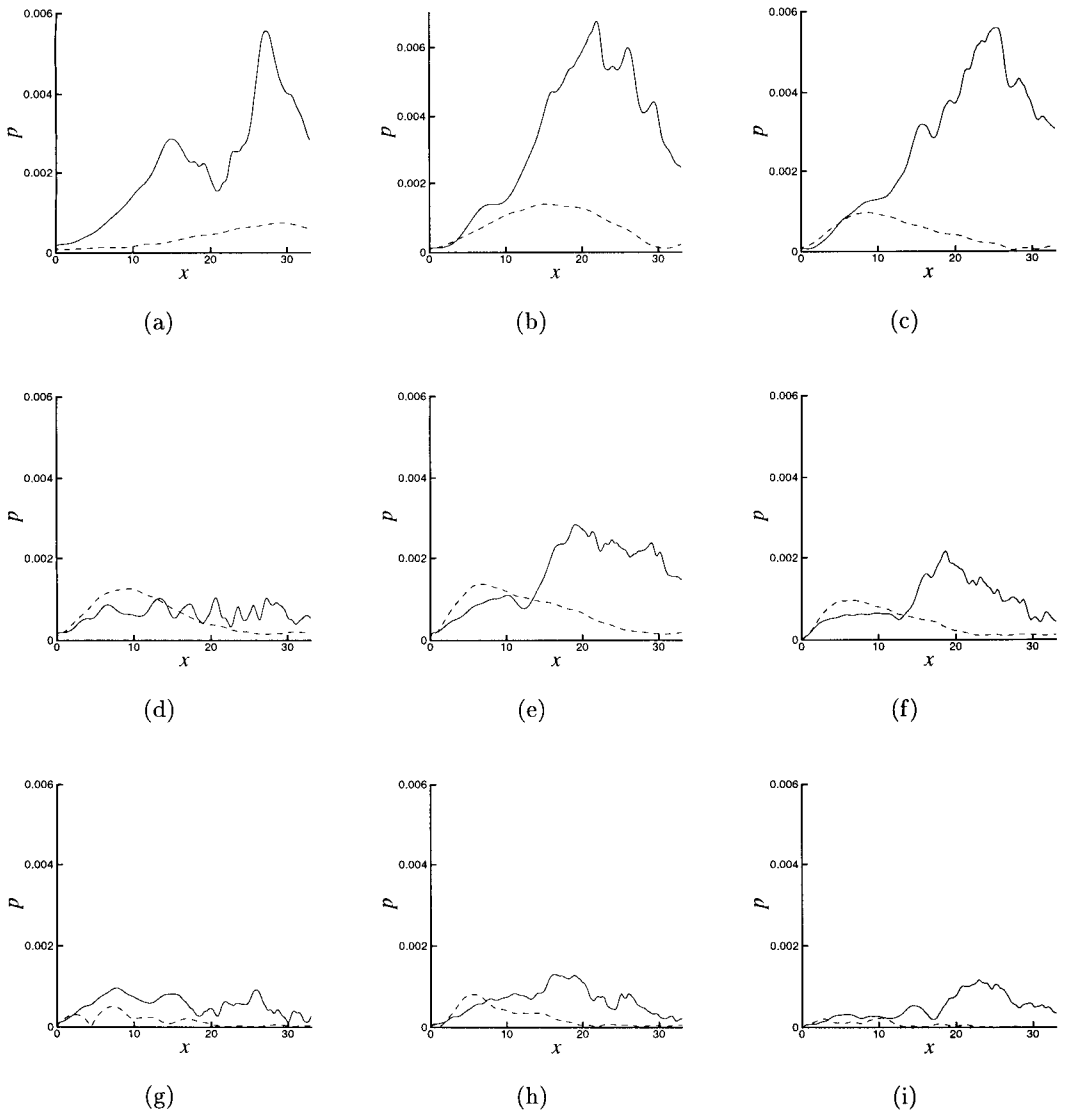

Figure 8.10 Perturbation pressure field for $n = 0$ at $r = 4$ for (a) $St = 0.048$ (b) $St = 0.095$ (c) $St = 0.143$ (d) $St = 0.191$ (e) $St = 0.238$ (f) $St = 0.286$ (g) $St = 0.333$ (h) $St = 0.381$ (i) $St = 0.429$. (——), DNS, and (----), LNS.

at all frequencies, the amplitudes of the modes are in agreement near the inflow boundary, which is really a check that identical inflow forcing was used in both calculations. In most cases, the modes from LNS saturate earlier, and with lower amplitude than the corresponding modes from DNS. In all cases, the agreement between DNS and LNS is better for $n = 1$ than it is for $n = 0$, which is consistent with our previous observation in section 8.1.

Another general trend in figure 8.9 is that the higher frequencies of the LNS calculation saturate earlier than the lower frequencies, an effect which is not evident in the DNS. The best agreement is observed for mode $n = 1$ around the peak Strouhal numbers (for $0.0952 \lesssim St \lesssim 0.1905$). For lower or higher frequencies the LNS calculations vastly underestimate the amplification of disturbances. This explains why the SPL of the LNS calculations is lower than the DNS calculations. For frequencies much higher than the peak frequency of the LNS equations, the linear instability waves do not grow and the amplification observed in the DNS data must be attributed to nonlinear sound sources.

The observation that turbulent flow, near and beyond the merging of the potential core, is responsible for a portion of the Mach wave radiation is not new, and was in fact observed by Troutt and McLaughlin [152]. In fact, it is interesting to observe that in their experiments, there is clear evidence in the near acoustic field that there are two distinct sources of waves at a given frequency, one originating from the shear layer region, the other further downstream. In the present low Reynolds number simulation, the shear layers are initially relatively thick and therefore higher frequencies, beyond $St = 0.4$ are damped immediately downstream of the inflow. We believe that this tends to somewhat obscure this effect, and at the frequencies that are amplified in the present shear layers, the source region from the shear layer and from further downstream cannot be clearly distinguished.

Unlike previous comparisons, however, the present comparison shows that Mach wave radiation due to nonlinear effects is not only present, but it can dominate the far acoustic field. While the present analysis is restricted to low Reynolds number, it can only be surmised that nonlinear effects, and the discrepancy between the far field Sound pressure level and linear stability predictions, would be of even greater importance at high Reynolds number.

In figures 8.11 and 8.12 the radial variation of the axial velocity and pressure distur-

bances for $n = 1$ are compared with the corresponding eigenfunctions of the LNS calculations for various frequencies, and at various axial locations. The agreement is again very good for regions close to the inflow boundary and gradually deteriorates as the turbulence develops along the jet. As is apparent from the figures, for higher frequencies the eigenfunctions of the LNS equations do not have a significant amplitude. For frequencies around the peak Strouhal number the amplitude of the eigenfunctions reduce significantly after the end of the potential core.

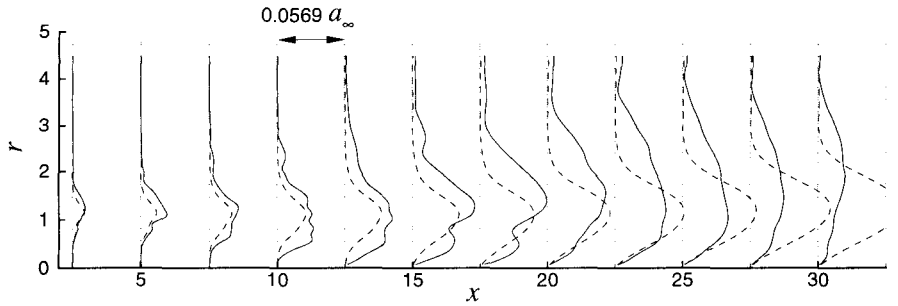

(a) $St = 0.0476$

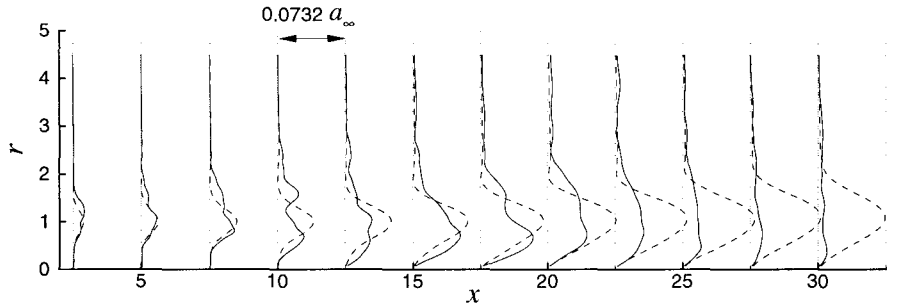

(b) $St = 0.0952$

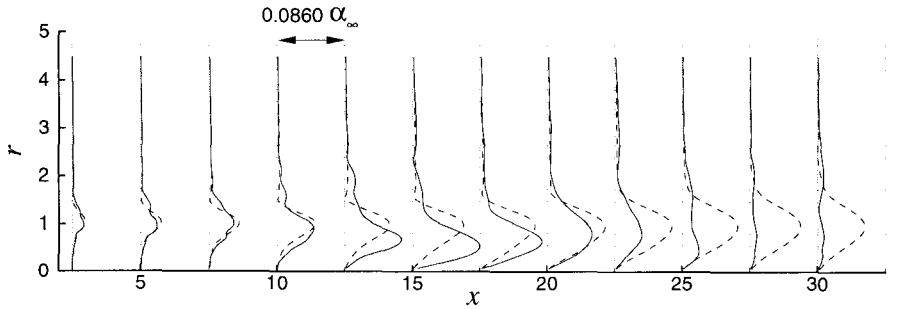

(c) $St = 0.1429$

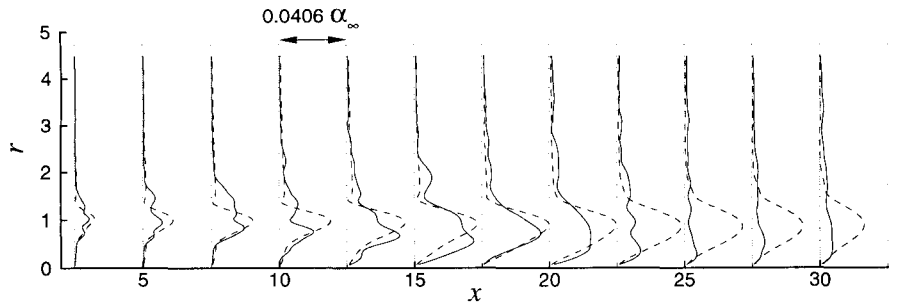

(d) $St = 0.1905$

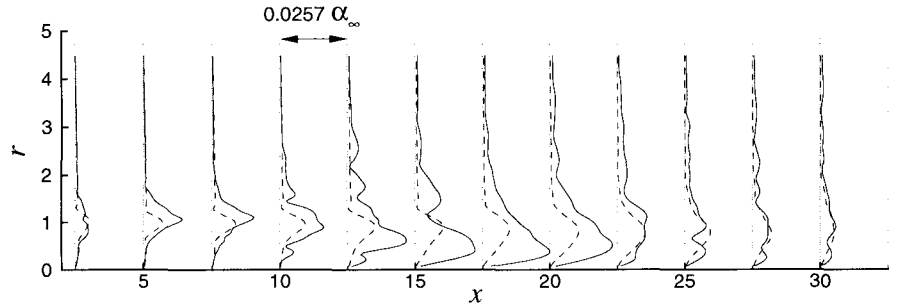

(e) $St = 0.2381$

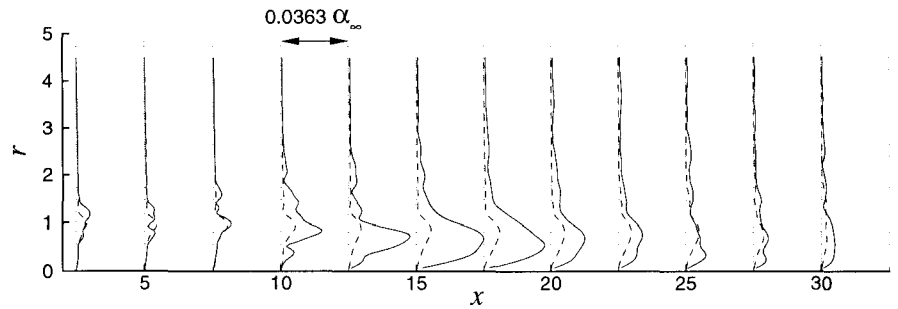

(f) $St = 0.2857$

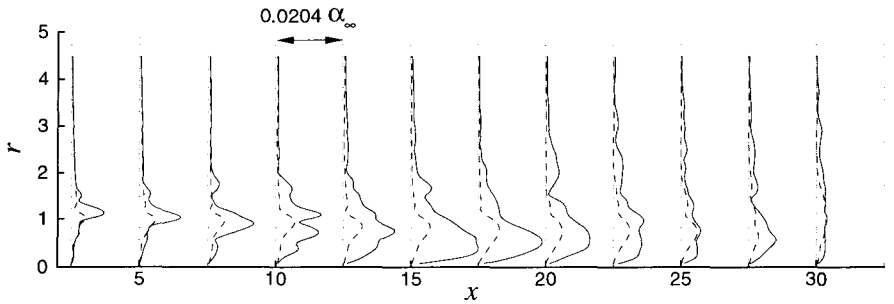

(g) $St = 0.3333$

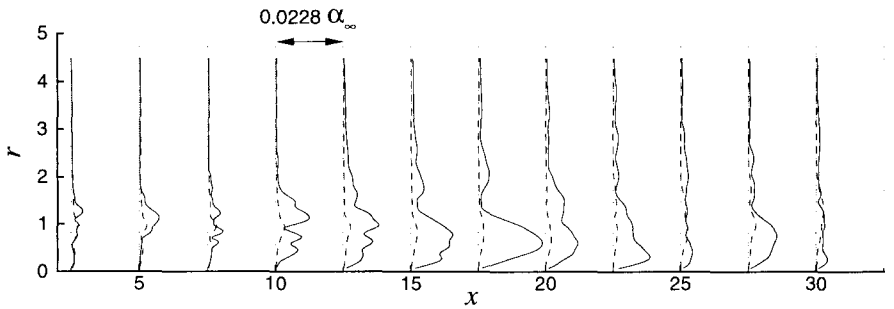

(h) $St = 0.3810$

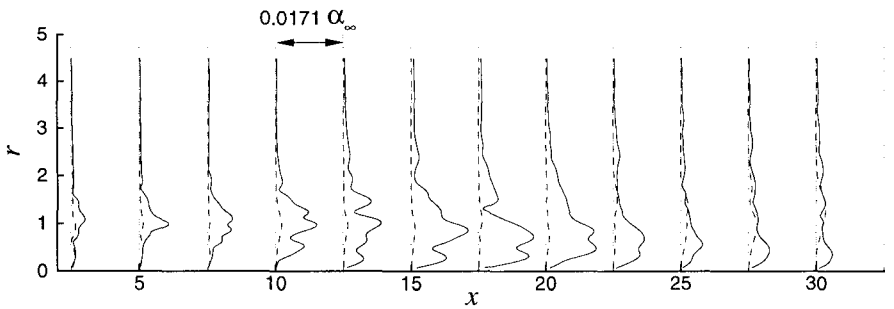

(i) $St = 0.4286$

Figure 8.11 Axial velocity eigenfunctions of LNS for (----) and DNS (———) calculations for $n = 1$ at various frequencies.

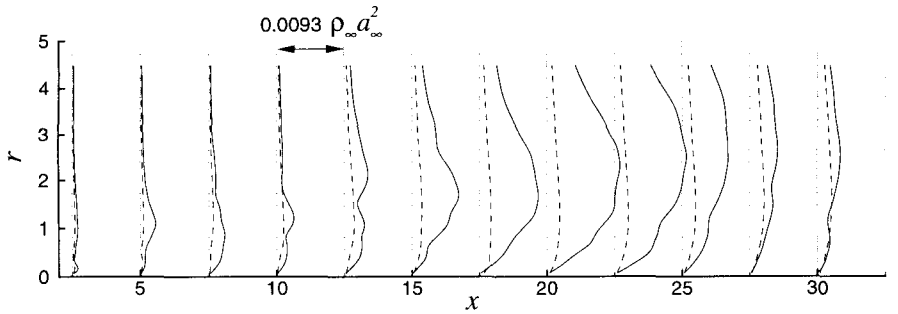

(a) $St = 0.0476$

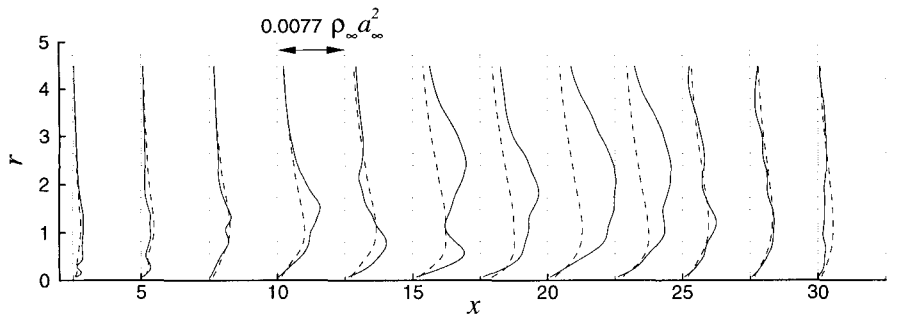

(b) $St = 0.0952$

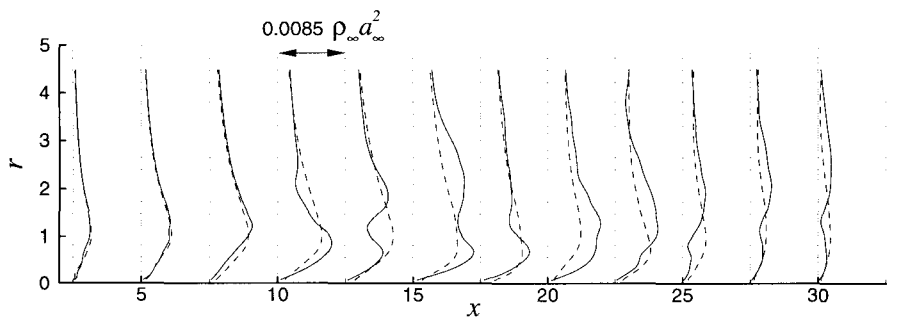

(c) $St = 0.1429$

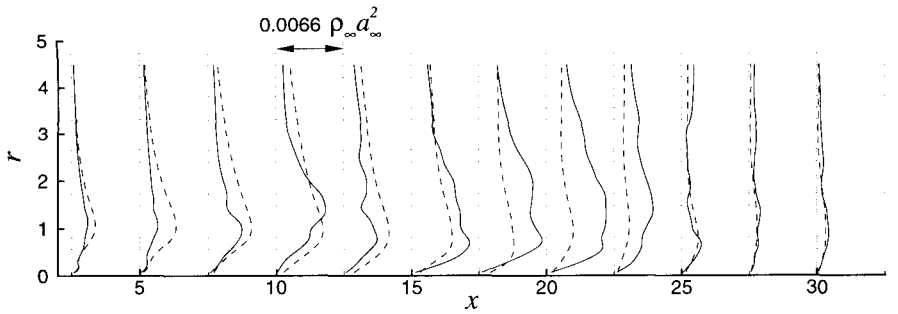

(d) $St = 0.1905$

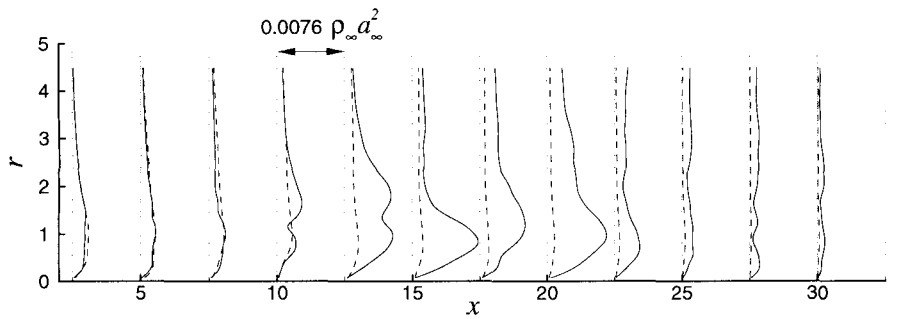

(e) $St = 0.2381$

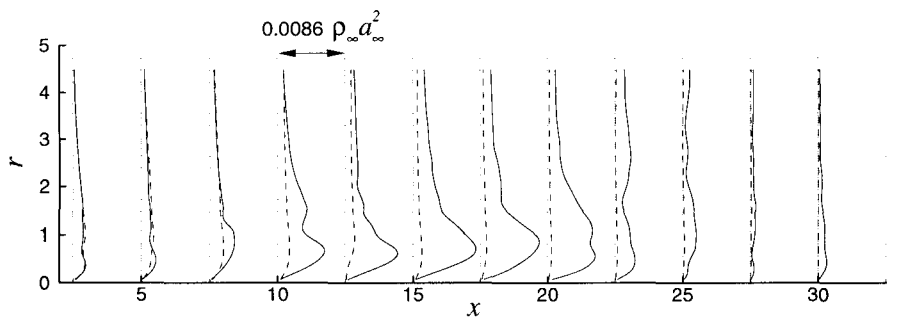

(f) $St = 0.2857$

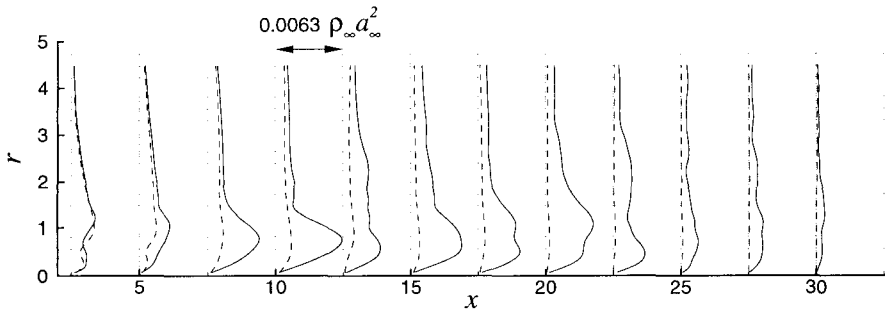

(g) $St = 0.3333$

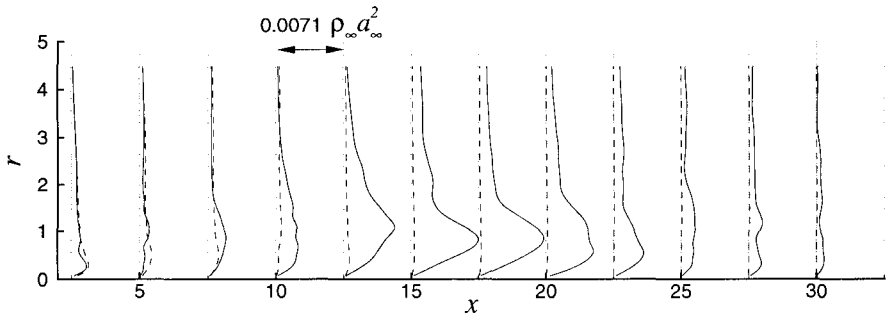

(h) $St = 0.3810$

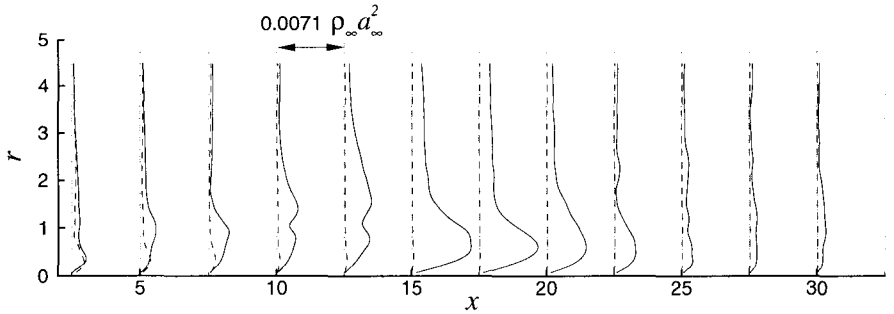

(i) $St = 0.4286$

Figure 8.12 Pressure eigenfunctions of LNS for (----) and DNS (———) calculations for $n = 1$ at various frequencies.

The amplification contours of various frequencies are shown in figures 8.13 and 8.14. The contour levels of the DNS data are intentionally set to be the same as in the LNS data. The saturated regions in the DNS data represent the regions that have louder sound sources that are not captured by the LNS calculations. Clearly, most of these saturated regions are around the end of the potential core, where the LNS calculations perform poorly. As is clear in the picture the LNS equations do not appropriately model the hydrodynamic fluctuations around the end of the potential core, where the nonlinearity and turbulence development dominates a large portion of the flow perturbations.

Another familiar scenario in turbulent mixing layers is the cascade of energy to smaller scales that feed energy to small scale eddies where they get dissipated by the action of viscosity. In linear theories the role of the small scale fluctuations is not described in detail. Instead it is argued that their role is primarily to dissipate the energy transferred to them from large scales and that the details of this process are unimportant to the flow development at the large scales, except through their contributions to the mean flow. Production of small scale turbulence depends on the Reynolds number, and noise generation by small scale turbulence is assumed to be more important in high Reynolds number flows where more energetic small scales are present. Therefore, for the relatively low Reynolds flow considered in this study and for the frequencies considered in this section we suspect that the differences between the acoustic field of the LNS and DNS data are mainly due to nonlinear effects, and sound field generated by the small scale turbulence, while exist, do not contribute significantly to the overall acoustic field at these frequencies.

We note in passing that there are some oscillations evident in the magnitude of the axial velocity and pressure disturbances in the LNS calculations for $n = 1$. Oscillations with similar characteristics were observed by Mitchell *et al.* [83] in computations of a supersonic axisymmetric jet. We investigated two possible causes for this effect. The first is a weak system of compression and expansion waves that exists in the mean core flow, as can be seen in figure 7.6(a). In order to gauge the effect of these waves on the modes, we calculated the spatial development of the instability waves for progressively smoothed mean flows (where the wave patterns are smoothed in the core) and found that these wave patterns were not responsible for the oscillations. The second possibility is the existence of

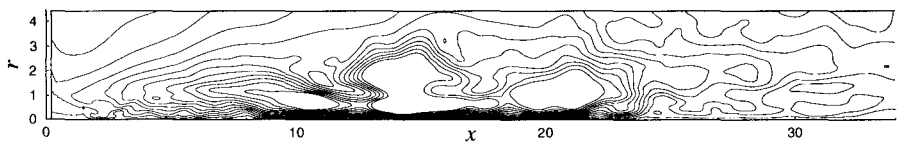

(a) DNS, $St = 0.1429$, 11 contour levels between 0.0005 and 0.0055

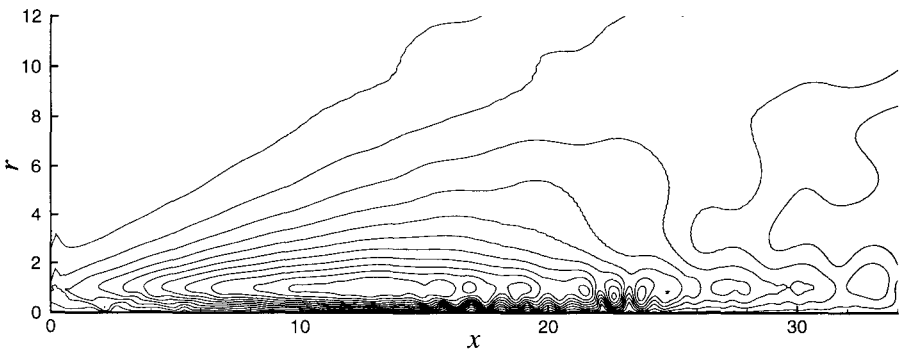

(b) LNS, $St = 0.1429$, 11 contour levels between 0.0005 and 0.0055

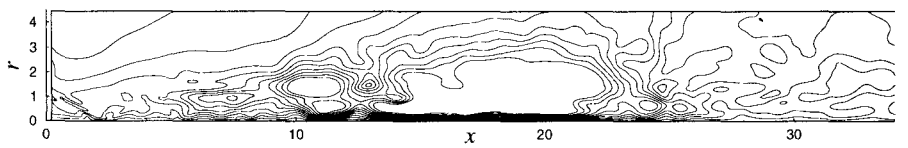

(c) DNS, $St = 0.1905$, 10 contour levels between 0.0004 and 0.004

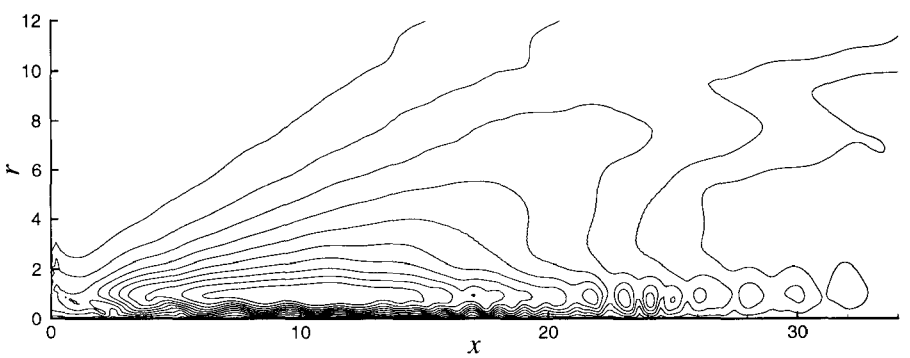

(d) LNS, $St = 0.1905$, 10 contour levels between 0.0004 and 0.004

Figure 8.13 Contours of the amplitude of perturbation pressure field for $n = 1$.

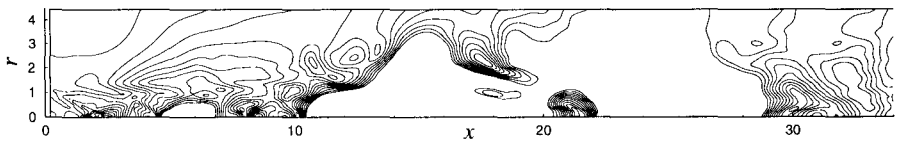

(a) DNS, $St = 0.1429$, 11 contour levels between 0.0004 and 0.0044

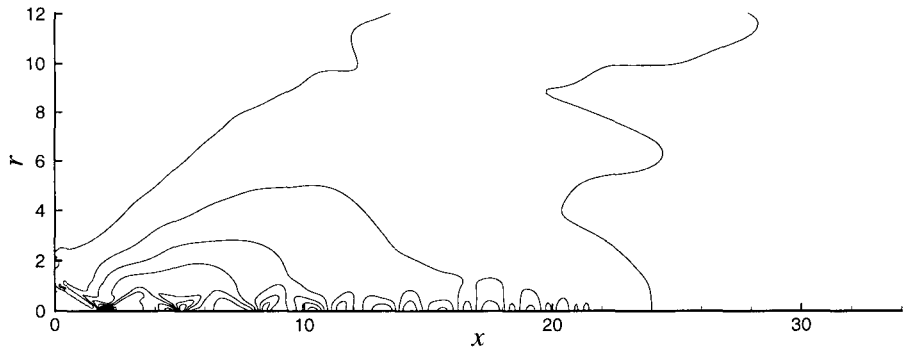

(b) LNS, $St = 0.1429$, 11 contour levels between 0.0004 and 0.0044

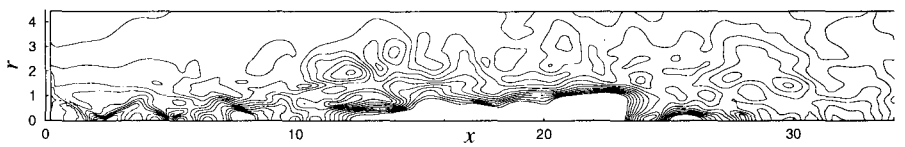

(c) DNS, $St = 0.1905$, 10 contour levels between 0.0004 and 0.004

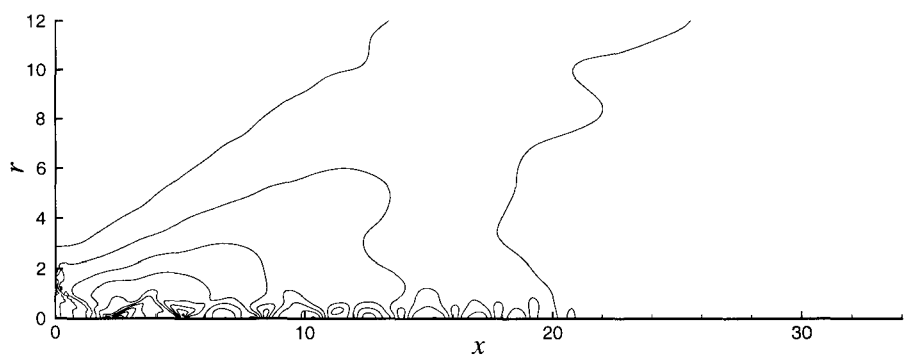

(d) LNS, $St = 0.1905$, 10 contour levels between 0.0004 and 0.004

Figure 8.14 Contours of the amplitude of perturbation pressure field for $n = 0$.

additional instability modes. The existence of multiple instability modes in supersonic jets is discussed by Oertel [103, 102, 104] and Tam and Hu [146]. Oertel's [104] experiments clearly show that both the supersonic instability waves and the Kelvin-Helmholtz instability waves are capable of sound generation. Subsonic waves radiate sound when their amplitude grows or decays. That is, the growth and decay of the wave causes its wavenumber spectrum to be broadband, leading to components with supersonic phase speed and therefore radiation. However, this Mach wave radiation mechanism would deteriorate for lower speed jets, as the instability waves with lower phase speed are less efficient in noise generation.

Our calculations based on the LST shows that at this Mach number (1.92) and temperature ratio (0.89) the Kelvin-Helmholtz instability waves are the dominant instability modes of the LNS equations, and the other type of instability waves, while present, do not amplify significantly.

The amplification rates of the LST are contrasted with LNS and DNS computations in figure 8.15. To find the free scaling factor in the LST calculations, the amplification rate of the LST calculations is matched with the LNS at $x = 2.5$, where the LST calculations starts.

The LNS and DNS calculations are both viscous, and have the same Reynolds number. On the other hand the LST of Tam and Burton [143] is an inviscid theory. Consequently, the eigenfunctions of the inviscid LST are discontinuous (at the critical layer) when the supersonic instability waves get damped. This discontinuity manifests itself in extreme peakiness of the axial velocity eigenfunction right before the waves damp. This is clear in figures 8.16 where the eigenfunctions of the LST calculations are compared with the LNS and DNS data for $n = 1$. Results for the azimuthal mode zero are not reported here, because the linear stability modes saturates and develops discontinuity very early in the development of the shear layer, usually before $x = 6$. For $n = 1$, the discontinuity develops at about $x = 11$. The amplitude of the pressure eigenfunction of the LST calculations is scaled appropriately to match the maximum amplitude of the corresponding pressure eigenfunction of the LNS calculations at the same axial location. Then, the same scaling factor is used to scale the velocity eigenfunction of the LST calculations. The agreement for the pressure eigenfunction is quite favorable, but the amplitude of the axial velocity

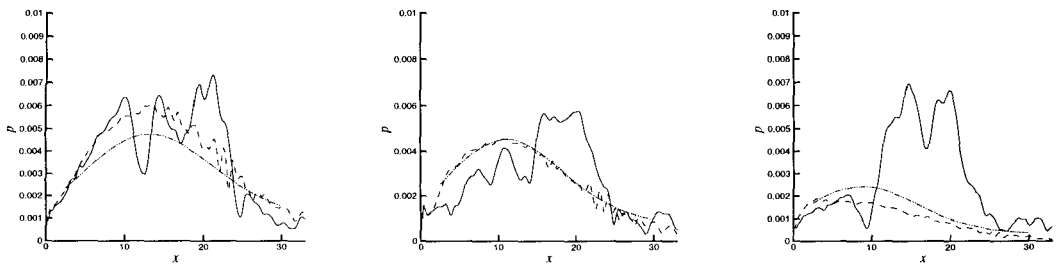

(a) $St = 0.1429, n = 1$ (b) $St = 0.1905, n = 1$ (c) $St = 0.2381, n = 1$

Figure 8.15 Pressure amplification at $r = 1$ for $n = 1$. (———) DNS; (- - - -) LNS; (—··—) LST.

eigenfunction is very sharp around the critical layer and develops a singularity further downstream. The peakiness in the amplitude of the axial velocity in the LST calculations is smoothed out by the viscous effects in the LNS computations.

Note that the pressure eigenfunctions of the LST do not behave according to the LNS data for large r. This is because for larger r the compressible Rayleigh equation must be asymptotically matched with the acoustic equations in the far field and the simple boundary condition in (7.38) will not capture the correct behavior for large r.

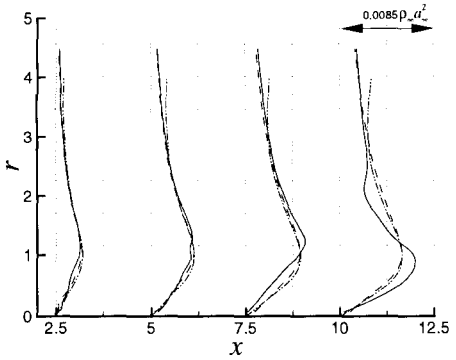

(a) $St = 0.1429$

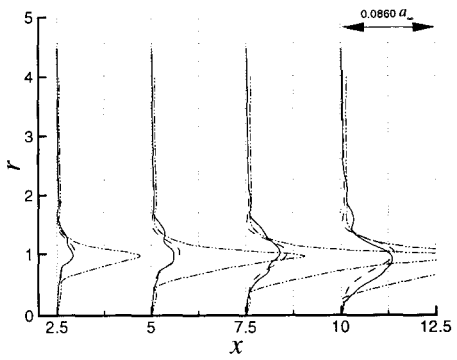

(b) $St = 0.1429$

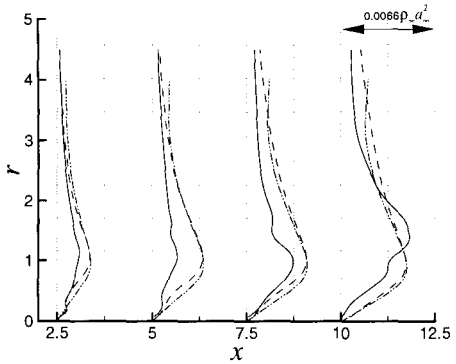

(c) $St = 0.1905$

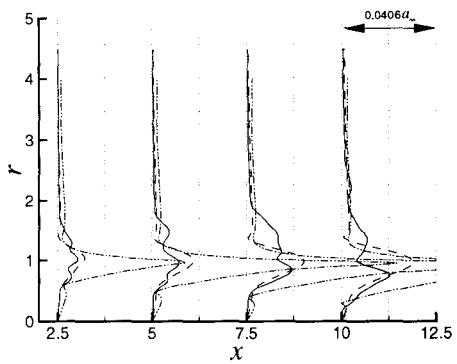

(d) $St = 0.1905$

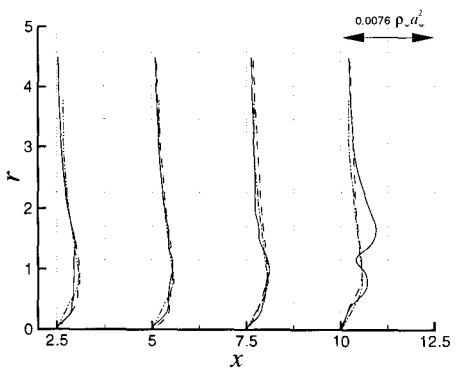

(e) $St = 0.2381$

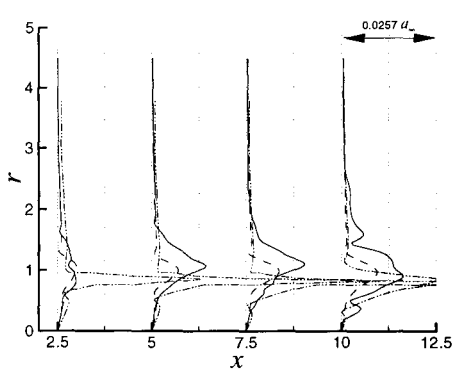

(f) $St = 0.2381$

Figure 8.16 Pressure (a,c,e) and velocity (b,d,f) eigenfunctions for $n = 1$ and for various frequencies. (———) DNS; (- - - -) LNS; (—··—) LST.

Chapter 9

Conclusions and Future Work

In this study we have critically evaluated the linear stability theory of Mach wave radiation in fully expanded supersonic jets. Until present, evidence supporting the theory has been restricted to a general agreement of the directivity of the Mach wave radiation, and its peak Strouhal number. In particular, the study of Troutt and MacLaughlin [152] showed that the initial growth rates of the jet instabilities and the wavelengths of the coherent disturbances are in good agreement with linear stability theory predictions. It is interesting to observe that in their experiments, there is clear evidence in the near acoustic field that there are two distinct sources of waves at a given frequency, one originating from the shear layer region, the other further downstream.

It is important to note here that the directivity of the acoustic field near the peak Strouhal number is not very sensitive to the details of the source process. Indeed, the growth and decay of any constant frequency convecting disturbance will produce such radiation, albeit at an amplitude which depends sharply on the growth and decay rates of the disturbance with streamwise distance. Nevertheless, the linear theory has been extensively used as a model of the sound generation process, and has formed the basis of a large number of attempts to control the sound either by direct forcing of the flow, geometrical changes to the nozzle, or modification of any co-flow. While some of the schemes lead to measurable changes in the sound radiation, they have not provided any conclusive data that such changes are related to alteration of instability waves.

Linear theory cannot predict the amplitude of the radiated sound without scaling the

data near the nozzle lip. As the turbulent fluctuations near the nozzle are very difficult to accurately measure, such scaling has never been rigorously performed. This would involve measuring the turbulent fluctuations (either from an experiment or a DNS), and decomposing that signal and projecting it onto a linear combination of the linear modes [24]. In fact, for compressible flow there remain technical details involving divergence of the inner products of the adjoint eigenvectors with the data that have not yet been resolved.

However, having access to DNS data from a 1.92 Mach jet [42], allows us to perform a direct comparison of sound generation by linear stability modes and noise generation by other mechanisms (*e.g.*, nonlinear sources or small-scale turbulence). Flow and acoustic informations from the available raw DNS data were extracted and compared with the results from a linearized Navier-Stokes computation. The numerical integration technique, inflow boundary conditions, and grid distributions were the same in both simulations. By keeping these and all other attributes the same, we were certain that we had captured all noise generated by linear stability waves in this flow.

The generated noise in the DNS calculation was dominated by the first two azimuthal modes, and contributions from all other azimuthal modes were limited to less than 1.5 dB in the acoustic field. This was consistent with predictions from linear theories. Therefore, we focused our linearized calculations on only the first two modes.

The total directivity of the sound field in the LNS matched reasonably well with the sound field of the DNS data. At the peak Strouhal frequency, particularly for n=1, the amplification of flow variables in the LNS closely matched that of the DNS data. However, for frequencies away from the peak Strouhal number the DNS data showed amplification rates comparable to those of the peak Strouhal number, while in the LNS data any disturbances away from the peak Strouhal number were highly damped. These extra noise sources in the DNS data were reminiscent of nonlinear interaction among various modes.

The noise generated by the first two modes in the linearized computation was substantially weaker than in the DNS. For example, in the near acoustic field, at a distance of 6 jet diameters from the jet centerline, the sound pressure level in the linearized computation was as much as 8 db smaller than the DNS results. This was in sharp contrast with the assumptions made in the linear stability theory that the Mach wave radiation in fully expanded

supersonic jets is dominated by the linear sound generation mechanisms. Therefore, one can conclude that while the linear sound generation by the large scale turbulent structures (or instability waves) constitute a large part of the turbulent mixing noise, an accurate account of sound generation in turbulent jets must include the other noise sources as well. We consider this as an evidence for the existence of relatively important noise sources apart from those *directly* related to the growth and decay of linear modes.

The maximum amplification for the DNS data occurred at an axial location further downstream than for the LNS data, which corresponds to regions around and beyond the end of the potential core. Our results indicated that the missing sound sources in the LNS computation at the frequencies considered in this study could be attributed to the non-linear sound generation. These non-linear sources were very effective sound sources, and a full theory of Mach wave radiation in fully expanded jets should take them into account. To gain insight into these interactions a more complex non-linear analysis technique is required.

It is unclear from the present work whether a better prediction for the evolution of the instability waves (say by accounting for nonlinear interactions amongst waves) would produce a more satisfactory prediction for their radiation sound. The Parabolized Stability Equation approach [53] offers a possible framework for such computations. Another possibility is that a genuinely nonlinear mechanism, such as Lighthill's quadrupole source, is needed to accurately predict the sound. It is interesting to note that Colonius and Freund [19] have found that the acoustic field from the present jet simulation was very well predicted by solving Lighthill's acoustic analogy equation with source terms computed from the DNS data. However, both linear and nonlinear interactions are present in Lighthill's source term and further work is necessary to distinguish them.

In order to complete the theory of Mach wave radiation from supersonic jets, and thereby produce a realistic model on which future noise control efforts could be based, future studies should concentrate on elucidating the precise mechanism by which nonlinear effects generate sound in the region near the end of the potential core.

Appendix A

Numerical Treatment of Polar Coordinate Singularities

The treatment of the geometrical singularity in cylindrical and spherical coordinates has for many years been a difficulty in the development of accurate finite difference (FD) and pseudospectral (PS) schemes. A variety of numerical procedures for dealing with the singularity have been suggested. For comparative purposes, some of these are discussed in the next sections, but the reader is referred to several books and review papers [12, 38, 50] for more detailed references.

Generally, methods discussed in the literature use pole equations, which are akin to boundary conditions to be applied at the singular point. The treatment of the pole as a computational boundary can lead to numerical difficulties. These include the necessity of special boundary closures for FD schemes (*e.g.*, [51]), undesirable clustering of grid points in PS schemes (*e.g.*, [57]), and, in FD schemes, the generation of spurious waves which oscillate from grid point to grid point (so-called two-delta or sawtooth waves, see [18, 155]).

In this section we investigate a method for treating the coordinate singularity whereby singular coordinates are redefined so that data is differentiated smoothly through the pole, and we avoid placing a grid point directly at the pole. This eliminates the need for any pole equation (see Mohseni and Colonius [87]). Despite the simplicity of the present technique, it appears to be an effective and systematic way to treat many scalar and vector equations in cylindrical and spherical coordinates. A similar technique was used by Merilees [79] for the south and north pole singularities of spherical coordinates, but appears not to have

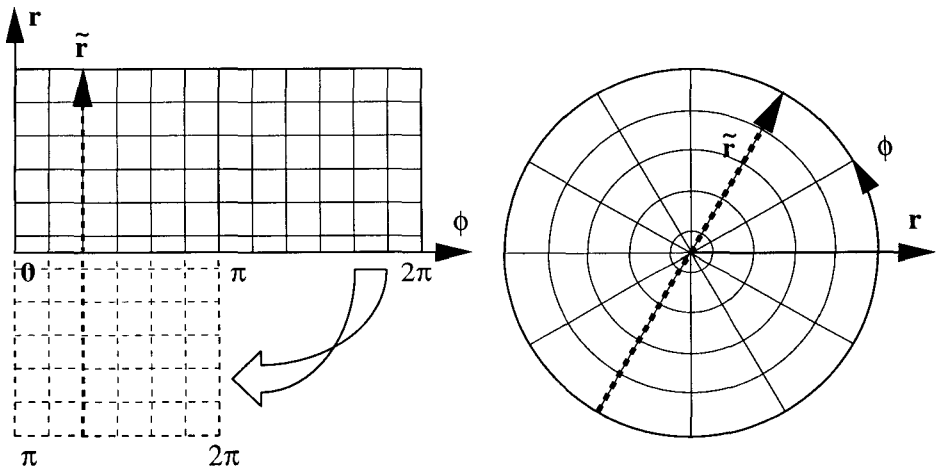

Figure A.1 Computational and physical domains.

been applied more generally. Here we show that the technique leads to excellent results for a number of model problems. The main application we consider is the compressible unsteady Euler and Navier-Stokes equations in cylindrical coordinates (section A.0.2) and Orr-Sommerfeld equation in cylindrical coordinates (section A.0.5). For comparison with other methods, we also treat the solution of Bessel's equation and scalar convection of a sphere in sections A.0.3 and A.0.4, respectively.

A.0.1 Approach

The present treatment of the $1/r^n$ singularities in the radial direction can be summarized as follows:

i. A new radial coordinate is defined over both positive and negative radius

$$\tilde{r}(r,\phi) = \begin{cases} r & \text{if } 0 \leq \phi < \pi \\ -r & \text{if } \pi \leq \phi < 2\pi \end{cases} \tag{A.1}$$

as depicted in figure A.1. This transformation has been already used in [38] to solve the Bessel's equation, but with a grid point at the pole and using the exact pole equation.

ii. Differentiation is performed with respect to the new coordinate, $\tilde{r}$, but on a set of nodes which avoids the singularity. For FD schemes (on a uniform mesh), for example, we have:

$$r_n = \frac{(2n+1)\Delta r}{2}; \qquad n = 0, 1, 2, \cdots \tag{A.2}$$

For PS schemes Chebyshev nodes (CN) with even number of points over $-1 \leq \tilde{r} \leq 1$:

$$r_k = -\cos(\pi k/2N_r + 1), \quad k = 0, 1, \cdots, 2N_r + 1 \tag{A.3}$$

will be suitable. These should be compared with, for example, the Chebyshev-Lobatto nodes (CLN) which are defined on $0 \leq r \leq 1$ as

$$r_k = \frac{1 - \cos(k\pi/N_r)}{2}, \quad k = 0, 1, \cdots, N_r \tag{A.4}$$

which give clustering around both $r = 0$ and 1 and have been recommended for PS solutions of problems with pole singularities by Huang and Sloan [57].

iii. Scalar and vector quantities must be transformed appropriately between the r to the $\tilde{r}$ coordinates. The following simple *transformation rule* holds: when $0 \leq \phi < \pi$ all quantities are the same in both coordinate systems. For $\pi \leq \phi < 2\pi$ we multiply any polar components of a vector quantity, radial derivative, and any r by -1. For example, the convective term $\partial(v_r v_\phi)/\partial r$ has exactly the same form and sign in both coordinates for $0 \leq \phi < \pi$ while it has opposite sign (because of multiplication by three negative signs) for $\pi \leq \phi < 2\pi$.

Note that this transformation is only used to calculate the radial derivatives. For the azimuthal derivatives the traditional definition of cylindrical coordinate is used. Thus the new singularity which is generated in the azimuthal direction by redefining the radial coordinate is avoided. Furthermore, in the axisymmetric case one need not carry the computations over $[-R, R]$, but instead symmetry conditions can be used to close FD schemes at the point adjacent to the pole and parity properties may be used in PS schemes to reduce the number of equations by half. However, we would like to emphasize that the general ap-

proach *does not* depend on any parity property of the equations and can be used to find non-axisymmetric solutions. An example is provided in section A.0.2.

Here we show that the rule of transformation (iii), applied to an arbitrary regular function f, is consistent with the constraints on the behavior of its Fourier series coefficients near the pole. Therefore, the transformation (iii) has no effect on the regularity of the function in the new coordinate. We take the Fourier series representation of an arbitrary function $f(r,\phi)$:

$$f(r,\phi) = \sum_{m=-\infty}^{\infty} a_m(r)\, e^{im\phi} \tag{A.5}$$

Now, if f is a regular scalar quantity, we must require that $a_m(r) = r^{|m|} b_m(r^2)$ as $r \to 0$, where $b_m(r^2)$ is a regular function of r^2 [65]. In the $(\tilde{r},\tilde{\phi})$ coordinates the same representation is valid for $0 \leq \phi < \pi$. If $\pi \leq \phi < 2\pi$ we substitute $\phi = \tilde{\phi} + \pi$ and $r = -\tilde{r}$. Hence

$$f(r,\phi) = \sum_{m=-\infty}^{\infty} a_m(-\tilde{r})\, e^{im(\tilde{\phi}+\pi)} = \sum_{m=-\infty}^{\infty} a_m(-\tilde{r})(-1)^m e^{im\tilde{\phi}} \tag{A.6}$$

But as $r \to 0$, we have $a_m(-\tilde{r})\,(-1)^m = a_m(\tilde{r})$ (see [65]), and thus the regularity of the function f is preserved in the new coordinate $(\tilde{r},\tilde{\phi})$. The rule of transformation (iii) can be justified by applying the preceding analysis to functions of the form $r^n f(r,\phi)$, radial derivatives of f, and vector quantities.

In spherical coordinates (r,ϕ,θ) the pole singularities are caused by two factors: $r \to 0$ and $\sin(\phi) \to 0$. The singularity of radial derivatives at $r = 0$ can be treated as described above for cylindrical coordinates, *i.e.*, by extending r to negative values and shifting the grid points in the radial direction by $\Delta r/2$ so that there is no grid point at $r = 0$. The singularities at $\phi = 0$ and π can be handled using a similar strategy (see Merilees [79]).

The maximum allowable timestep for convective problems is usually controlled by the Courant-Friedrichs-Lewy (CFL) number. The effect of grid distributions on the CFL number has been the subject of previous research [12, 3]. Here we compare the CFL requirements for the present and conventional grid distributions.

A conservative estimate for the CFL number will depend on the minimum mesh spacing in any of the three coordinate directions. To simplify the argument, in the rest of this section we assume that the CFL criteria are the same in all directions.

For axisymmetric problems, the conventional grid defined by: $r_n = n\Delta r;\ n = 0, 1, 2, \cdots$, gives a CFL constraint which is dependent on Δr. Despite the grid point at $\Delta r/2$ in the modified grid (equation A.2) numerical experiments confirm that the CFL number continues to scale with Δr. For *non-axisymmetric* problems, the situation is different. For N_ϕ Fourier or FD modes in the azimuthal direction, the minimum length of the mesh in the ϕ-direction is now $\pi\Delta r/N_\phi$, half of the value for a conventional grid with the first node at Δr. Thus with no further modification, the maximum time step in the present approach is a factor of two smaller than other approaches. In either case, the CFL constraint is *very restrictive* in non-axisymmetric cylindrical coordinates, the minimum time step being proportional to the product of the grid spacing in r and ϕ.

In both cases it is possible to alleviate this constraint by explicitly filtering the results in the ϕ direction, as has been suggested by many investigators (*e.g.*, [12] and references therein). Since the solution is periodic in the ϕ direction, it is possible to employ a sharp spectral filter at a particular cutoff wavenumber. For grids defined by $r_n = n\Delta r;\ n = 0, 1, 2, \cdots$, the effective mesh spacing in the ϕ direction becomes $\Delta x_\phi = 2\pi\Delta r/N_{f\phi}$ along the circle at $r = \Delta r$, where $N_{f\phi}$ is the number of nodes retained. Thus if 7 or fewer nodes are retained, the CFL constraint will be dictated by Δr. The maximal number of nodes of $N_{f\phi} \approx 2\pi n$ that should be retained at different radial locations r_n follows in an analogous way. For the present grid, the first node is placed at $\Delta r/2$, then we need merely retain fewer Fourier modes (at most $N_{f\phi} \approx \pi n$) at each r_n, so that the CFL constraint depends on Δr alone.

In PS methods, the clustering of node points near the boundaries also has an impact on the maximum CFL number. Since the pole is traditionally considered as a boundary point, the same clustering occurs at the poles (*e.g.*, [57]). Fornberg [38] noticed that it is possible to alleviate the quadratic clustering of nodes near the origin, by defining the radial coordinate as in equation (A.1). We observe the same property in our grid distribution, except that our grid points are shifted so that no grid point is located at the pole. Therefore, one

can choose the grid distribution in the $\tilde{r}$ coordinate to dramatically increase the maximum timestep required for stability around the centerline for PS methods compared to other grid distributions. In fact, using the distributions given above, it can easily be shown that the distance from the centerline to the first node away from the centerline is N_r/π times greater for the CN distribution than for the CLN distribution, in the limit of large N_r. Thus the maximum time step increases also by this factor.

Finally, we would like to point out that the present approach should not be confused with the idea of staggered grids (*e.g.*, [36]). Here, we use the co-located discretization where the nodes are chosen to avoid singularities.

A.0.2 Compressible Navier-Stokes Equations

We consider solution of the Navier-Stokes and Euler equations in cylindrical coordinates. One approach which has been used in the past is to superpose a Cartesian coordinate system at the singularity as was done, for example, in recent compressible jet calculations by Mitchell *et al.* [83, 84] and Freund *et al.* [40]. A different approach was used by Griffin *et al.* [51], where l'Hopital's rule was used to the singular terms in the NS equations to derive a new set of equations valid at the centerline. These equations are then solved by one-sided difference schemes at the centerline. They observed a significant loss of accuracy when the biased difference scheme used at the centerline was less accurate than the interior scheme. Various other schemes for the Navier-Stokes equations in cylindrical coordinates have been given in the literature [3, 72, 97, 126, 153].

Aside from the centerline treatment, the details of the numerical scheme used in this work are similar to the approach of Freund *et al.* [40]. At the outer radial boundary non-reflecting boundary conditions are implemented [47]. In the radial direction we use a sixth order accurate compact Padé scheme [64] and in the azimuthal direction a Fourier spectral method is used. For the purposes of this paper, only flows which are uniform in the axial direction are considered. Fourth order Runge-Kutta time advancement is used to advance the solution to the next time step. This combination of high-order-accurate compact finite difference schemes and explicit Runge-Kutta time advancements has now been used in many codes developed for solving problems in compressible turbulence and

aeroacoustics (*e.g.*, [23, 40, 83, 84]).

For the centerline treatment, we implement two approaches: the first (CL1) uses the coordinate transformation and grid distribution discussed in the last section; the other (CL2) solves the equations in Cartesian coordinates at the centerline [40, 84, 83].

As an example, consider the propagation of a Gaussian acoustic pulse with unit variance located, initially, off-centered at $(r = 1, \phi = 0)$ in a cylindrical coordinates. The specific head ratio is 1.4. The outer radial non-reflecting boundary is placed at $r = 8$. The grid is 81 by 64 nodes in the radial and azimuthal directions, respectively. The acoustic pulse initially has the form of a small amplitude pressure and density disturbance superposed on their (constant) ambient values. In the present example, we take the magnitude of the acoustic pulse to be very small (10^{-6}) such that nonlinear effects are minimal and an exact solution to the linearized version of this problem can be found [148] and compared to the numerical solution. In what follows, we give the density of the acoustic wave (less the ambient density) relative to the ambient density. Lengths are normalized by the variance (width) of the initial Gaussian pulse, and time is normalized using this length and the ambient sound speed. The time step for these calculations is $\Delta t = 0.003125$.

In addition to a greater ease of implementation, we find that in viscous computations, method CL1 is stable with a much smaller viscosity (higher Re) than CL2. Long time instability of the inviscid method is characteristic of non-dissipative (centered) finite difference schemes in general, and is not directly a consequence of the coordinate singularity. The instability is believed to result from aliasing of energy onto the highest wavenumbers supported by the grid (sawtooth waves), and repeated reflections (and, indeed, amplification) of these waves by the non-periodic boundaries. In figure A.2 the numerical solution of inviscid equations for method CL1 is shown for times 2 and 4. The absolute error is plotted for both CL1 and CL2 at time $t = 2$ in figure A.3. For CL2, poorly resolved sawtooth waves can be seen. It is clear that they are produced by the centerline treatment since the pulse is initially located off-center at $r = 1$. These short wavelength disturbances are, continuously, produced at the centerline. They are similar to the sawtooth waves studied by Trefethen [151], Vichnevetsky [155], and Colonius *et al.* [18], where it has been shown that they can propagate at physically inappropriate (large and with incorrect sign) group

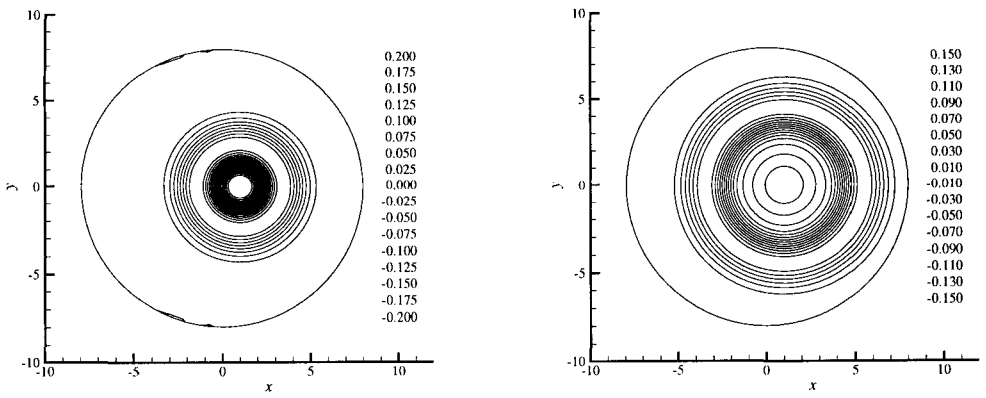

(a) (b)

Figure A.2 Numerical solution (density perturbation relative to initial amplitude) for method CL1 at (a) $t = 2$, (b) $t = 4$.

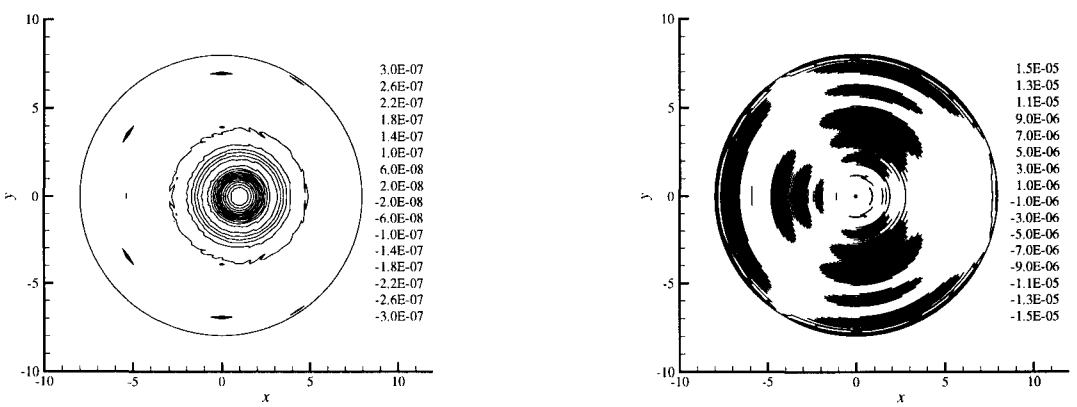

(a) (b)

Figure A.3 Absolute error in solution at $t = 2$ relative to the initial amplitude of the pulse for (a) CL1, (b) CL2.

velocities and that they are converted to smooth (well-resolved) waves upon interaction with boundary conditions (in this case at both $r = 0$ and $r = R$). By contrast, such spurious waves are not evident for treatment CL1, and the error (figure A.3a) is centered at the center of the acoustic pulse and is almost 2 orders of magnitude smaller than CL2. This error is apparently controlled only by the finite resolution.

A.0.3 Bessel's Equation

To compare the method described above to previous treatments, we consider PS and FD solutions of Bessel's equation in cylindrical and spherical coordinates:

$$\frac{1}{r^a}\frac{d}{dr}\left(r^a\frac{dy}{dr}\right) - \frac{n(n+a-1)}{r^2}y = -\lambda y, \qquad 0 \le r \le 1, \tag{A.7}$$

where $n \geq 0$, and $a = 1, 2$ for Bessel's and spherical Bessel's equations, respectively. The boundary condition for both equations is given by $y(1) = 0$. The eigenvalues for the Bessel's equation are given analytically by $\lambda_{np} = r_{np}^2$, where r_{np} are the zeroes of the Bessel's functions J: $J_n(r_{np}) = 0, \quad p = 1, 2, \cdots$. The solution to the equation is the spherical Bessel's equation $j_n(r'_{np})$, where r'_{np} are the zeroes of $j_n(r'_{np}) = 0, \quad p = 1, 2, \cdots$ and the eigenvalues are $\lambda_{np} = r'^2_{np}$.

For Bessel's equation, Gottlieb and Orszag [50] improved the convergence of their Chebyshev tau method by using the pole condition $y'(0) = 0$. Huang and Sloan [57] showed that this pole condition does not give spectral accuracy for $n = 1$. They derived an improved pole condition for $n = 1$ to preserve the spectral accuracy. Fornberg [38] used these pole equations but he changed definition of the cylindrical coordinate (eq. A.1) to allow the radial grid to run through the pole. In addition to more accuracy, he notes the possible advantage of not having a clustering of the nodes near $r = 0$. Note that unlike the present approach, a node, and therefore a pole equation, is used at the singularity, $r = 0$. Recently, Matsushima and Marcus [75] found a new set of basis functions defined by a singular Sturm-Lioville equation so that the pole condition is maintained. They applied their method successfully to Bessel's equation and the vorticity transport equation on a unit disk.

Here the present method is employed to solve Bessel's equation with a PS method based

on the Lagrange's interpolation formula [57], but without any pole conditions. We use the parity property of the Bessel's equation to reduce the calculation to only the positive half of the Chebyshev node distribution considered in section A.0.1:

$$r_k = \cos\left(\frac{\pi(k - N_r)}{2N_r + 1}\right), \quad k = 0, 1, \cdots, N_r. \tag{A.8}$$

In figure A.4 the convergence of the numerical solution to the exact eigenvalue is shown. The relative errors for the first eigenvalue, λ_{n1}, for $n = 7$ and 49 are plotted for various PS schemes and a second order FD method with the present treatment of the singularity.

All of the solutions are very accurate, and for large N it becomes difficult to compare the relative accuracy of the schemes, since the error becomes dominated by roundoff even with double precision arithmetic. To overcome this problem and make reliable comparisons between methods, we recomputed the results with sufficient precision arithmetic using the *Mathematica* [162] program when necessary.

Apparently the new pole treatment gives spectral convergence and is more accurate for all N than that of ref. [57, 75]. Matsushima and Marcus [75] pointed out that the spectral convergence of the Chebyshev expansion of Gottlieb and Orszag [50] deteriorates significantly as n becomes large. This effect was attributed to the shifting of the oscillatory part of the Bessel function moving toward the outer boundary as n increases. It is clear from the figure that our PS approach is not suffering from the oscillatory behavior of the solution near the boundary and gives better convergence. Finally, similar results for $n = 1$ presented by Fornberg [38] overlaps with our results for $n = 1$. However, his results were obtained using an exact pole equation which is not available for more complex equations, such as those considered in the previous section.

Similarly the smallest eigenvalue of the spherical Bessel's equation is calculated numerically and the relative errors for $n = 49$ is shown in figure A.5. This result is compared with a Chebyshev tau method similar to [50] and the recent results by Matsushima and Marcus [75].

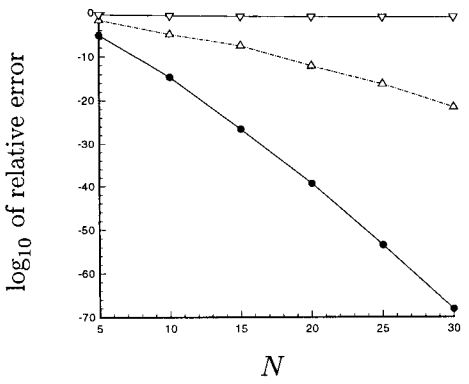

(a)

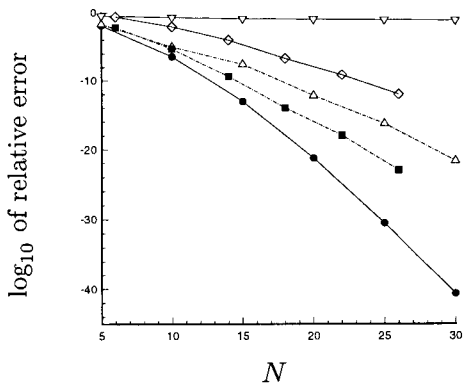

(b)

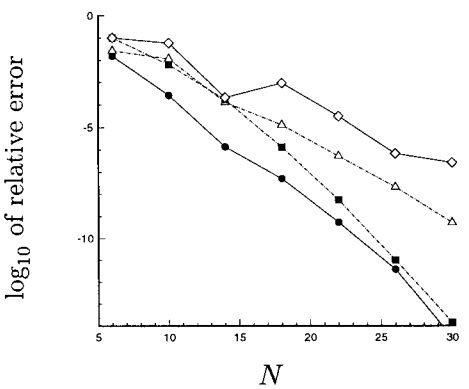

(c)

Figure A.4 First eigenvalues of the Bessel equation for (a) $n = 1$, (b) $n = 7$, (c) $n = 49$. $\triangle$ Huang & Sloan [57]; $\triangledown$ second order FD; $\bullet$ present approach; $\diamond$ Gottlieb and Orszag [50]; $\blacksquare$ Matsushima and Marcus [75].

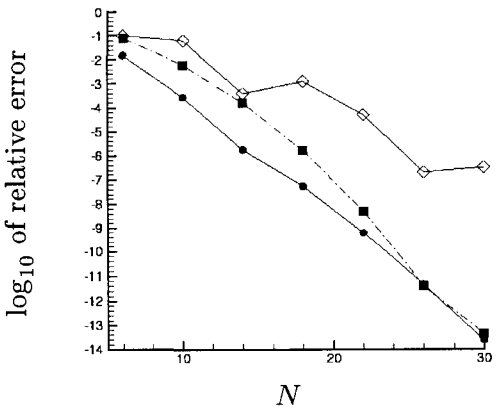

(a)

Figure A.5 The first eigenvalue of the spherical Bessel's equation for $n = 49$. • present approach; ◇ Chebyshev tau method; ■ Matsushima and Marcus [75].

A.0.4 North and South Pole Singularities

In spherical coordinates (r, ϕ, θ) the pole singularities are caused by two factors: $r \to 0$ and $\sin(\phi) \to 0$. The singularity of radial derivatives at $r = 0$ can be treated as described before, *i.e.*, by extending r to accept negative values and removing the grid point at $r = 0$. Extending the same methodology to the treatment of the SNPS's of spherical coordinates gives, essentially, the method that Merilees [79] implemented for the PS solution of the shallow water equations over a sphere. We summarize his results here and generalize them to any type of scalar and vector equations with SNPS's in spherical coordinates.

The singularities at $\phi = 0$ and π can be handled as follows. We eliminate the grid points at the south and north poles and extend θ from 0 to 2π. Therefore, a periodicity in the θ will be achieved which could be used to easily calculate the derivatives in the θ-direction. Similar rule of transformation as in the cylindrical coordinate is applied for transforming from one coordinate system to the other coordinate system: for $0 \leq \phi < \pi$ all quantities are the same in both coordinate systems; for $\pi \leq \phi < 2\pi$ we multiply any polar component of a vector quantity or any derivative with respect to θ by -1. The most appropriate grid

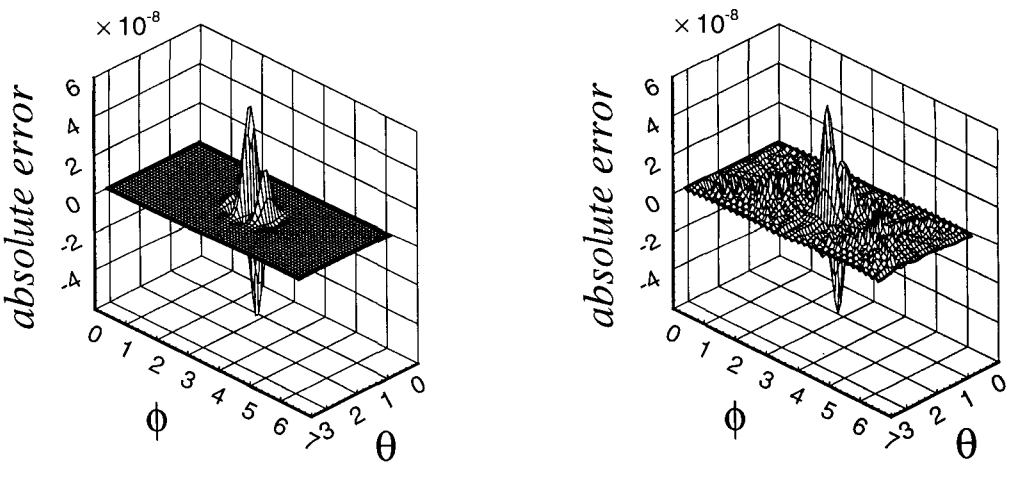

(a) (b)

Figure A.6 Absolute error for solid convection over a sphere: (a) along the equator (b) over the pole.

distribution in this case is shifted equidistance grid in latitude direction. Computations by Fornberg (private communications) and our own results for solid convection over a sphere reconfirmed the robustness of this approach.

As an example consider the convection of a passive scalar on a sphere. Consider the solid convection of a Gaussian with variance 0.2 on the surface of a sphere. We use a Fourier pseudospectral method to solve:

$$\frac{\partial u}{\partial t} = a\frac{\partial u}{\partial \theta} + b\frac{\partial u}{\partial \phi} \tag{A.9}$$

for two cases: rotation around the equator ($a = 0,\ b = -1$) and rotation across the pole ($a = -\cos\phi,\ b = \sin\phi\cot\theta$). This problem was also studied by Fornberg and Sloan [39, 37, 38] with the same approach, except that grid points where located at the poles and the following pole condition was used: $\frac{\partial u}{\partial t}|_{all\ \phi} = -\frac{\partial u}{\partial \phi}|_{\phi=0}$.

Figure A.6 shows the results after 10 revolutions for 32 and 64 grid points along the θ

and ϕ directions, respectively. We used very small time steps so that all the visible errors are due to the spatial discretization. The errors are of the same magnitude for both rotation around the equator and the pole, indicating good performance of the present method. Note that the small amplitude noise present in the rotation across the pole is dispersive error caused by convection through the non-uniform mesh near the poles.

A.0.5 Accurate Calculation of Eigenvalues of Orr-Sommerfeld Equation

In a recent study with professor J. Marsden on transition to turbulence in a pipe flow [90], we applied the polar coordinate singularity treatment described previously in section A.0.1 to calculate the eigenvalues of Orr-Sommerfeld equations in cylindrical coordinates. Here we present some of these results (further detail is provided in Mohseni and Marsden [90]).

There are three distinct modes for axisymmetric disturbances [29], namely the wall, center, and mean modes. The pioneering work of Orszag [106] on accurate calculations of all three branches of eigen spectrums for the plane Orr-Sommerfeld equation inspired many other publications to extend his results to other applications and different methods. Although Orszag's results were accurate for the mean modes, the calculated eigenvalues for the wall modes suffered from oscillations, and their eigenfunctions were somewhat scattered. The same behavior is observed for the wall modes in pipe flows [1, 29] (which is not surprising, since when the disturbance is confined to a thin layer near the wall of the pipe the problem becomes identical to a thin layer near the wall in plane Couette flow, see J. Pretsch, *ZAMM*, 21, 204 (1941)). Here we use a different approach. We treat the coordinate singularity by the method presented in section A and [88]. The differential equation is discretized by a pseudospectral method based on Lagrange's interpolation formula.

The usual parabolic profile is assumed for the mean velocity distribution in the pipe. For simplicity, we present results only for the axisymmetric mode of pipe flow. Figure A.7 presents the eigenvalues for the axisymmetric mode of Orr-Sommerfeld equations. 46 nodes are used in this calculation. Note that the lower two branches in figure 4.18 of Drazin [29] are due to numerical artifacts and are not physical modes. Our numerical techniques capture the correct behavior of the wall modes, as predicted by Gill [48], while the results based on the Chebyshev expansion [1, 29] are scattered around the correct wall modes. The spectral

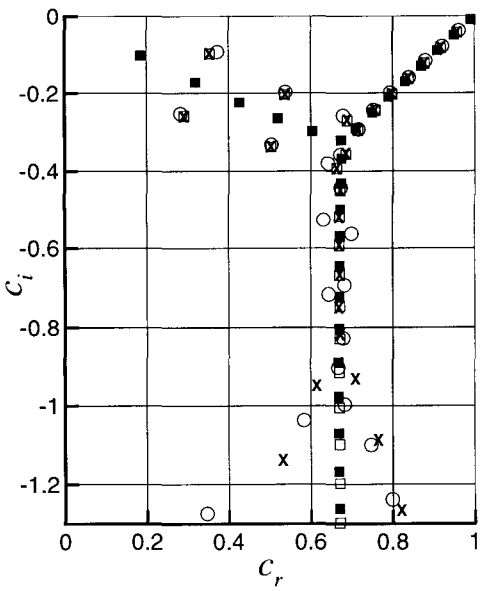

Figure A.7 Eigenvalues of axisymmetric mode of pipe flow, wavenumber $\alpha = 1, Re_R = 5000$. (∘) Davey and Drazin; (×) Abbot and Moss, $N = 46$; (□) Abbot and Moss $N = 80$; and (▪) present approach, $N = 46$.

convergence of the Chebyshev expansion based on Gottlieb and Orszag [50] deteriorates significantly (see [75, 88]), if the solution has oscillatory behavior close to the boundary. We suspect the same effect is responsible for the oscillations observed in calculations by [29] and [1] for the eigenvalues of wall modes.

We suspect that some of the oscillations in wall mode eigenvalues in Poiseulle and Couette flows as well as nonaxisymmetric modes of pipe flows presented in the literatures are only numerical artifact (spurious modes) that can be removed by a technique similar to the one presented here.

Appendix B

Axisymmetric Vortex Filament Method

In this section we study the Hamiltonian structure of axisymmetric vortex filaments. To derive the Hamilton equations for discrete vortex filaments we use the field Poisson bracket (3.14) and the field Hamilton equation (3.15). A similar approach has been pursued by Morrison [99] for deriving the point vortex equations in a plane, and is closely followed here. We assume that the vorticity density distribution can be approximated by a combination of discrete axisymmetric vortex filaments as

$$\xi(\boldsymbol{x}) = \sum_{i=1}^{N} c_i \, \delta(\boldsymbol{x} - \boldsymbol{x}_i). \tag{B.1}$$

Substituting equation (B.1) into the Hamiltonian (3.10) we obtain

$$H = \pi \sum_{i=1}^{N} \sum_{j=1}^{N} c_i c_j \mathcal{M}(\boldsymbol{x}_i | \boldsymbol{x}_j) \tag{B.2}$$

where $\mathcal{M}(\boldsymbol{x}_i|\boldsymbol{x}_j)$ is given by (3.12). One can use the symmetry of the kernel function $\mathcal{M}(\boldsymbol{x}_i|\boldsymbol{x}_j)$ to simplify the double sum in (B.2). It can be easily shown that

$$\frac{\partial H}{\partial x_i} = c_i \frac{\partial}{\partial x} \left. \frac{\delta H}{\delta \xi} \right|_{\boldsymbol{x}_i}, \tag{B.3}$$

$$\frac{\partial H}{\partial y_i} = c_i \frac{\partial}{\partial y} \left. \frac{\delta H}{\delta \xi} \right|_{\boldsymbol{x}_i}. \tag{B.4}$$

Consequently, the Poisson bracket (3.14) can be represented as

$$\{F, G\} = \sum_{i=1}^{N} \frac{1}{c_i} \left(\frac{\partial F}{\partial x_i} \frac{\partial G}{\partial y_i} - \frac{\partial F}{\partial y_i} \frac{\partial G}{\partial x_i} \right). \tag{B.5}$$

Hence using (B.3), (B.4), and (B.1), the Poisson bracket of ξ and H can be represented by

$$\{\xi, H\} = \sum_{i=1}^{N} \frac{1}{c_i} \left(\frac{\partial \xi}{\partial x_i} \frac{\partial H}{\partial y_i} - \frac{\partial \xi}{\partial y_i} \frac{\partial H}{\partial x_i} \right). \tag{B.6}$$

Since ξ obtains its t dependence through $\boldsymbol{x}_i$ we can substitute (B.1) and (B.6) in equation (3.15) to yield

$$\begin{aligned} c_i \frac{dx_i}{dt} &= \frac{\partial H}{\partial y_i}, \\ c_i \frac{dy_i}{dt} &= -\frac{\partial H}{\partial x_i}. \end{aligned} \tag{B.7}$$

Note that these equations are similar to Hamilton equations for point vortices in plane.

Appendix C

Evaluation of Giles and Tam's Nonreflecting Boundary Conditions for The Euler Equation

Jet noise problem is categorized among the socalled exterior problems. To simulate these types of problems it is necessary to impose nonreflecting boundary conditions at the boundaries of the computational domain. As discussed in section 7.3, linearized Euler equations can support three types of waves. Therefore, a general disturbance interacting with the boundary would contain in general a combination of these waves. An effective boundary condition is the one that produces minimum reflection in interaction with a general disturbance. Our objective in this section is to compare the short-time and long-time behavior of Giles and Tam's nonreflecting boundary conditions (BC's), for the Euler equations. Both sets of BC's are evaluated using the same discretization, order of approximation and time advancement. Results are shown for two different test cases. One test had zero mean flow while the other had a uniform subsonic mean flow.

C.0.6 Introduction

The physical domain of an aeroacoustic problem is often infinite. There are various numerical methods which can be used for problems defined on an infinite space. One approach is to map the infinite physical space to a finite computational space. This approach is not recommended because poor resolution near infinity can produce large errors and therefore degrade the accuracy of the computed solution. An alternative approach is to truncate the physical domain at some finite, artificial surface. This creates a finite computational

domain at the expense of imposing additional BC's at the artificial boundary.

If there is a propagating solution in the vicinity of the artificial boundary, the BC's must correctly specify the energy leaving the computational domain. Any inaccuracy in the specification of these BC's can produce spurious waves which propagate into the computational domain. In this case there will be a spurious energy propagation into the computational domain from "infinity." There are various possibilities to reduce these undesired reflections. One possibility is to use progressively coarser grid spacing as the waves move out toward the far-field boundary. If the mesh is coarse enough that the wavelength of the wave is comparable to a few mesh cells, then artificial viscosity can be used to damp out the oscillations such that the waves will not reach the boundary. However, it should be pointed out that nonuniform grids themselves produce spurious reflections [151, 30]. Furthermore, this approach is not effective at inflow boundaries.

Apart from artificial viscosity one can use the filtering process to remove the poorly resolved waves near the boundary [22]. All of the above methods still produce some spurious reflections. To minimize these reflections one can enlarge the computational domain. However, this increases both the running time and the memory requirements for the program. Therefore, it is preferable to construct a better nonreflecting BC (see [49] for the goals of an effective nonreflective BC).

We base our BC analysis on the inviscid equations (Euler equations), even though one may solve viscous equations (Navier-Stokes equations) for the interior points. At high Re, viscous effects are generally not important in the far-field.

Two different nonreflecting BC's are considered in this study. The first uses a decomposition of the solutions into Fourier components. The second is of an asymptotic far-field nature. The idea is to evaluate these two boundary conditions for short and long times. For short times we compare the numerical results obtained with a known analytical solution. For long times we expect that the numerical scheme and the nonreflecting BC's be stable and remain stable for large number of time steps. These two nonreflecting boundary conditions are as follows.

A. Giles BC: Giles BC is derived based on Fourier analysis of the 2-D linearized Euler equation [47]. It is known that in Fourier space an exact nonreflecting BC for Euler equation

can be obtained. The idea is to prevent propagation of waves with inward group velocities. The resulting modified dispersion relation in Fourier space does not correspond to a local boundary condition in physical space. However, it can be expanded in a Taylor series to find a hierarchy of approximate local non-reflecting BC's. For details of the derivations of BC's we refer to Giles [47]. Two classes of Giles BC's are implemented:

- **Giles BC I** is Giles BC's with "modified" outflow and "modified" inflow.
- **Giles BC II** is Giles BC's with "modified" inflow but the outflow is not modified.

Note that both Giles BC's are modified to handle the incoming entropy wave in the manner suggested by Colonius *et al.* [22].

B. Tam's BC: Tam and Webb [148] considered the linearized Euler equations. They used Fourier and Laplace transforms to derive the first term of the asymptotic expansion for the convective wave equation for large distance from a source located in the center of the computational domain. They then derived a set of nonreflecting BC's based on the far-field asymptotic solutions. Note that the final form of these BC's are represented in cylindrical coordinates.

C.0.7 Numerical Method

As noted in references [22] and [148], it is essential to use a numerical scheme which reproduces the dispersion relation of the governing partial differential equation very accurately. Therefore, in this study we use the fourth order Padé scheme [63]. For the points near the boundaries one requires additional relations. To determine the derivatives which occur in the BC's Gustafsson [52] has pointed out that the accuracy of the numerical procedure for a linear equation can usually be one order lower than the order of the interior scheme without adversely influencing the global accuracy of the solution. Therefore, by using a third order accurate Padé next to the boundary, we preserve the fourth order global accuracy. For the time advancement a fourth order Rung-Kutta method is used.

C.0.8 Results

We nondimensionalize the equations using the speed of sound at infinity, a_∞, the density and pressure at infinity, ρ_∞ and $\rho_\infty a_\infty^2$ respectively. All geometrical length scales are normalized relative to the variance of the initial Gaussian pressure disturbance σ.

To evaluate the nonreflecting BC's introduced above, we construct two test cases:

Test Case I: First, to demonstrate the nonreflectivity of these BC's, we consider a stationary case $M = 0$. Consider an initial Gaussian pressure and density disturbances in the center of a square domain which extends to $\pm\frac{3}{2}$ in both x and y (nondimensionalized). The mesh size is 60×60. Figure C.1 shows many decades of drop in the total energy of

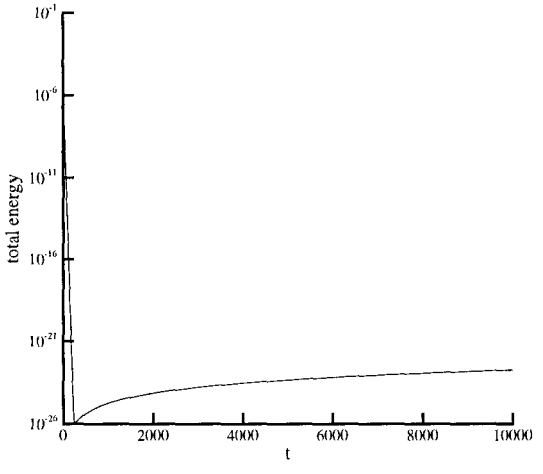

Figure C.1 L_2 norm of energy in the computational domain.

fluid within the computational domain. A good nonreflecting BC should be stable; *e.g.*, the energy does not grow in time (particularly exponentially). Note that the slope of the energy drop is also important. The theoretical answer drops exponentially after the acoustic wave leaves the domain. Therefore, steeper slope in energy means better nonreflective behavior.

We observed that Giles BC's I and II are both stable whether the boundaries are considered as either outflow or inflow. Note that when M=0, it is ambiguous in the case of the

vorticity and entropy waves whether the boundary should be considered inflow or outflow. Tam's outflow conditions are also stable; however, Tam's inflow BC is unstable after the first interaction of the outgoing waves with the boundary. The energy profile is almost the same in all stable cases. It is important to note that Giles BC's are quite sensitive to the treatment at corners. In all of our computations Giles BC's are applied at 45° at the corners, as recommended by [22].

Since in this case the first waves and therefore the corresponding characteristics cross the boundary at the radial direction, it might seem reasonable to apply the Giles BC's at the radial directions for any point on the boundary. The solution in this case was unstable (at least for long times) even when only a few points near the corners are modified. Studying the wave patterns in the computational domain after a few reflections reveals that the radial directivity of characteristics at the boundary points is no longer valid and this could be the main source of instability. Further results related to the long-time behavior are given below.

Test Case II: The performance of the nonreflecting BC's for short times are investigated in test case II. Consider a uniform mean flow of $M = 0.5$ in the x direction. We know that the linearized Euler equations support three types of waves, namely the acoustic, the entropy, and the vorticity waves. Test case II consists of an initial acoustic wave and a combination of vorticity and density disturbances. The acoustic wave propagates with the speed of sound superimposed on the mean flow. The entropy and vorticity waves propagate in the direction of mean flow with the same speed as the flow.

The acoustic pulse is generated by an initial Gaussian pressure distribution in the center of computational domain. A schematic diagram of the computational domain is shown in figure C.2. Lengths are made nondimensional with the variance of the Gaussian pulse. Downstream of the pressure pulse at $\frac{x}{\sigma} = \frac{200\sqrt{2\ln 2}}{9}$, a vorticity and entropy pulse (also with Gaussian distributions) are also preset. All the three pulses reach the outflow boundary simultaneously. In the simulation the computational domain extends to $\pm\frac{100\sqrt{2\ln 2}}{3}$ (nondimensional) is divided into 200×200 mesh. The parameters for the initial conditions are

pressure pulse amplitude = 0.01, variance = 1,

entropy pulse amplitude = 0.001,variance = $\frac{5}{3}$,

vorticity pulse amplitude = 0.0004,variance =$\frac{5}{3}$.

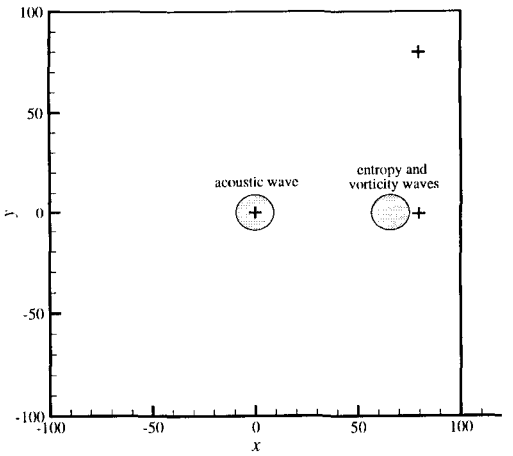

Figure C.2 Computational domain. Location of points for calculating the short time errors are marked by (+).

The analytical solution was provided by Tam and Webb [148].

The accuracy of the BC's was evaluated at three points in the computational domain. These points are located at $(\frac{x}{\sigma}, \frac{y}{\sigma}) = (0,0)$, $(\frac{80\sqrt{2\ln 2}}{3}, \frac{80\sqrt{2\ln 2}}{3})$, and$(\frac{80\sqrt{2\ln 2}}{3}, 0)$, respectively (see figure C.2). The first is mainly affected by the initial acoustic waves and not by the entropy or the vorticity waves. Obviously, the point $(\frac{80\sqrt{2\ln 2}}{3}, \frac{80\sqrt{2\ln 2}}{3})$ will be most affected by the corner points. The second point gives a good measure of the error when the acoustic, entropy and vorticity waves simultaneously interact with the boundary. A comparison of the computational results with the analytical solution is given in figures (C.3- C.5). These figures show the absolute error in the density fluctuations as a function of time. In figure C.3 there is a high peak in the absolute error for the Tam's BC's around $\frac{t\sigma}{a_\infty} = 300$. This shows the sensitivity of the Tam's BC's to the acoustic reflections from the top and bottom boundaries of the computational domain. In figure C.4 all the different BC's have a high error when the initial acoustic front reaches the point $(\frac{80\sqrt{2\ln 2}}{3}, \frac{80\sqrt{2\ln 2}}{3})$ around $\frac{t\sigma}{a_\infty} = 90$. This could be due to inaccuracy in the magnitude or direction of the group velocities of the resolved waves. While Tam's and Giles BC's I represent a reasonable accuracy at a later time, Giles BC's II produce much larger error when the reflected acoustic waves from the

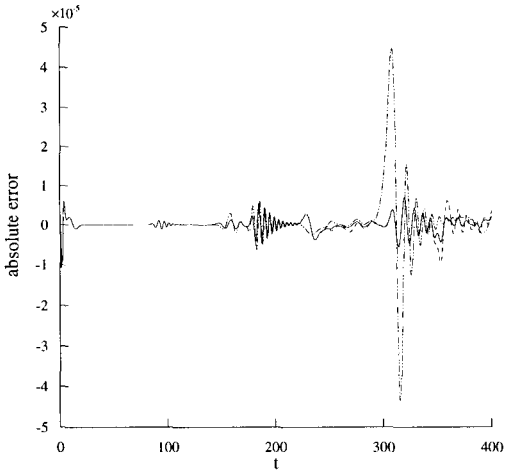

Figure C.3 Absolute error in density at point (0, 0). (———) Giles BC's, modified inflow and outflow; (----) Giles BC's, modified inflow; (—··—) Tam's BC's.

outflow BC reaches the point $(\frac{80\sqrt{2\ln 2}}{3}, \frac{80\sqrt{2\ln 2}}{3})$. At the third point $(\frac{80\sqrt{2\ln 2}}{3}), (\frac{80\sqrt{2\ln 2}}{3}, 0)$, near the outflow BC, all of the three BC's behave almost the same.

A long time comparison of the different nonreflecting BC's is presented in figure C.6. The best long time behavior is obtained with Giles BC II. Giles BC I is also stable but it saturates at higher energy levels. Tam's BC's is unstable after multiple reflections. One reason for this behavior could be the restriction of Tam's BC to be nonreflecting only to waves radiating from the center of the computational domain.

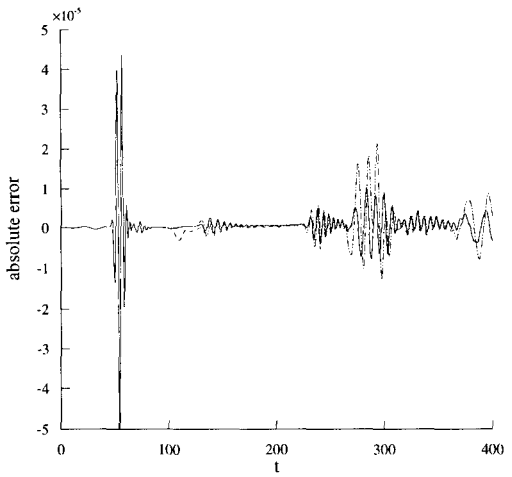

Figure C.4 Absolute error in density at point $(\frac{80\sqrt{2\ln 2}}{3}, 0)$. (———) Giles BC's, modified inflow and outflow; (- - - -) Giles BC's, modified inflow; (—··—) Tam's BC's.

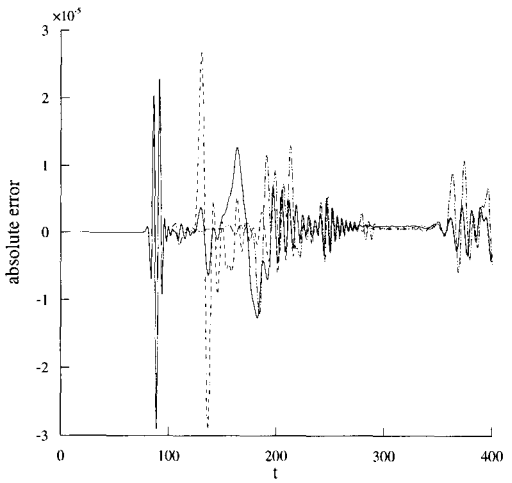

Figure C.5 Absolute error in density at point $(\frac{80\sqrt{2\ln 2}}{3}, \frac{80\sqrt{2\ln 2}}{3})$. (———) Giles BC's, modified inflow and outflow; (- - - -) Giles BC's, modified inflow; (—··—) Tam's BC's.

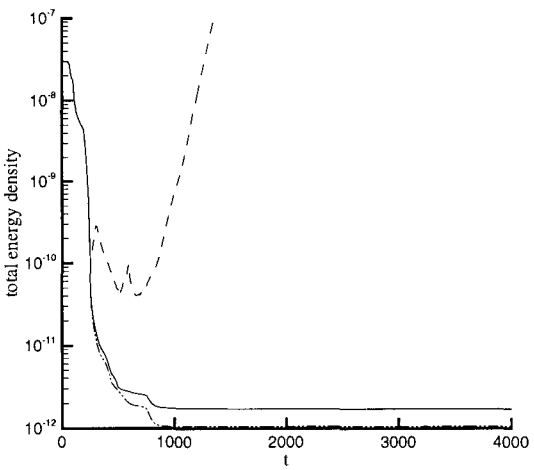

Figure C.6 Total energy in the computational domain. (———) Giles BC's, modified inflow and outflow; (- - - -) Giles BC's, modified inflow; (— · · —) Tam's BC's.

Bibliography

[1] A.H. Abbot and E.A. Moss. Sources of error in eigenvalue spectra for pipe-Poiseuille flows. *J. Fluids Eng., Trans. ASME*, 118(2):414–416, 1996.

[2] M.A. Abramowitz and I.A. Stegun. *Handbook of Mathematical Functions.* Dover, 1972.

[3] K. Akselvoll and P. Moin. An efficient method for temporal integration of the Navier-Stokes equations in confined axisymmetric geometries. *J. Comp. Phys.*, 125(2):454–463, 1996.

[4] V.I. Arnold. Sur la géometrie différentielle des groupes de lie de dimension infinie et ses applications a l'geometry. hydrodynamique des fluides parfaits. *Ann. Inst. Fourier (Grenoble)*, 16:319–361, 1966.

[5] V.I. Arnold. The Hamiltonian nature of the Euler equations in the dynamics of a rigid body and of a perfect fluid. *Usp. Mat. Nauk.*, 24:225–226, 1969.

[6] V.I. Arnold. On an a priori estimate in the theory of hydrodynamical stability. *Am. Math. Soc. Transl. Ser.*, 2(79):267–69, 1969. Translation from 1966.

[7] V.I. Arnold. *Mathematical Methods of Classical Mechanics.* Springer-Verlag, 1978.

[8] G.K. Batchelor. Computation of the energy spectrum in homogeneous two-dimensional turbulence. *Phy. Fluids*, Supplement II:233–239, 1969.

[9] T.B. Benjamin. The alliance of practical and analytical insights into the nonlinear problems of fluid mechanics. In *Applications of Methods of Functional Analysis to Problems in Mechanics*, volume 503, pages 8–29. Springer-Verlag, 1976.

[10] R. Betchov and W.O. Criminale. *Stability of Parallel Flows.* Academic Press, 1967.

[11] G. Brown and A. Roshko. On density effects and large structure in turbulent mixing layers. *J. Fluid Mech*, 64:775–816, 1974.

[12] C. Canuto, M.Y. Hussaini, A. Quarteroni, and T.A. Zang. *Spectral Methods in Fluid Dynamics*. Springer-Verlag, 1987.

[13] Y.Y. Chan and R. Westley. Directional acoustic radiation generated by spatial jet instability. *Can. Aero. and Space Inst. Trans.*, 6:36–41, 1973.

[14] P.H. Chavanis and J. Sommeria. Classification of robust isolated vortices in two-dimensional hydrodynamics. *J. Fluid Mech*, 356:259–296, 1998.

[15] P. Chen. *Coherent Vortex States in Two-Dimensional Ideal Fluid.* PhD thesis, California Institute of Technology, 1996.

[16] P. Chen and M.C. Cross. Mixing and thermal equilibrium in the dynamical relaxation of a vortex ring. *Phys. Rev. Lett.*, 77(20):4174–4177, 1996.

[17] T.S Chyczewski and L.N. Long. Numerical prediction of the noise produced by a perfectly expanded rectangular jet. AIAA Paper 96-1730, 1996.

[18] T. Colonius. Numerically nonreflecting boundary and interface conditions, for compressible flow and aeroacoustic computations. *AIAA J.*, 35(7):1126–1133, 1997.

[19] T. Colonius and J.B. Freund. Application of Lighthill's equation to mach 1.92 turbulent jet. *AIAA J.*, 38(2):368–370, 2000.

[20] T. Colonius, S. K. Lele, and P. Moin. Direct computation of aerodynamic sound. Report no. TF-65, Department of Mechanical Engineering, Stanford University, 1995.

[21] T. Colonius, S.K. Lele, and P. Moin. The free compressible viscous vortex. *J. Fluid Mech.*, 203:45–73, 1991.

[22] T. Colonius, S.K. Lele, and P. Moin. Boundary conditions for direct computation of aerodynamic sound generation. *AIAA J.*, 31(9):1574–1582, 1993.

[23] T. Colonius, S.K. Lele, and P. Moin. Sound generation in a mixing layer. *J. Fluid Mech.*, 330:375–409, 1997.

[24] T. Colonius, K. Mohseni, J.B. Freunda, S.K. Lele, and P. Moin. Evaluation of noise radiation mechanisms in turbulent jet. In *Proceedings of the 1998 Summer Program*, pages 159–167. NASA Ames/Stanford Univ., November 1998.

[25] S.C. Crow and F.H. Champagne. Orderly structures in jet turbulence. *J. Fluid Mech*, 77:397–413, 1971.

[26] M.D. Dahl and P.J. Morris. Noise from supersonic coaxial jets .1. mean flow predictions. *J. of Sound and Vibration*, 200(5):643–663, 1997.

[27] M.D. Dahl and P.J. Morris. Noise from supersonic coaxial jets .2. normal velocity profile. *J. of Sound and Vibration*, 200(5):665–669, 1997.

[28] M.D. Dahl and P.J. Morris. Noise from supersonic coaxial jets .3. inverted velocity profile. *J. of Sound and Vibration*, 200(5):701–719, 1997.

[29] P.G. Drazin and W.H. Reid. *Hydrodynamic Stability.* Cambridge Univ. Press, Cambridge, UK, 1981.

[30] A.H.M. Eisenga, R. Verzicco, and G.J.F. van Heijst. Wave propagation analysis of difference schemes for hyperbolic equations: A review. *Int. J. Num. Methods Fluids*, 7:409–452, 1987.

[31] B. Engquist and A. Majda. Absorbing boundary conditions for numerical simulation of waves. *Math. Comp.*, 31(139):629–651, 1977.

[32] B. Engquist and A. Majda. Radiation boundary conditions for acoustic and elastic wave calculations. *Comm. on Pure and Applied Math.*, 32:313–357, 1979.

[33] FAA. *DOT/FAA Noise Standards: Aircraft Type and Airworthiness Certification*, Far part 36 edition, 1990.

[34] FAA. *Transition to an All Stage 3 Fleet Operating in the 48 Contiguous United States and the District of Columbia*, Federal Aviation Administration, 14 CFR Part 91 Amendment edition, September 1991.

[35] FAA, Advisory Circular AC36-1F. *Noise Levels for U.S. Certificated and Foreign Aircraft*, Federal Aviation Administration edition, June 1992.

[36] J.H. Ferziger and M. Peric. *Computational Methods for Fluid Dynamics.* Springer Verlag, 1996.

[37] B. Fornberg. A pseudo-spectral approach for polar and spherical geometries. *SIAM J. Sci. Comput.*, 1995.

[38] B. Fornberg. *A Practical Guide to Pseudo-spectral Methods.* Cambridge Univ. Press, 1996.

[39] B. Fornberg and D. M. Sloan. A review of pseudo-spectral methods for solving partial differential equations. In *Acta Numerica*, pages 203–267. 1994.

[40] J. B. Freund, S. K. Lele, and P. Moin. Direct simulation of a supersonic round turbulent shear layer. AIAA Paper 97-0760, 1997.

[41] J.B. Freund. Proposed inflow/outflow boundary condition for direct computation of aerodynamic sound. *AIAA J.*, 35(4):740–742, 1997.

[42] J.B. Freund, S.K. Lele, and P. Moin. Direct simulation of a Mach 1.92 jet and its sound field. AIAA/CEAS Paper 98-2291, 1998.

[43] J.B. Freund, P. Moin, and S.K. Lele. Compressibility effects in a turbulent annular mixing layer. Technical Report TF-72, Dept. Mech. Eng., Stanford University, Stanford, California, September 1997.

[44] A. Friedman and B. Turkington. Vortex rings: Existence and asymptotic estimates. *Trans. Am. Math. Soc.*, 268(1):1–37, 1981.

[45] M. Gaster, E. Kit, and I. Wygnanski. Large-scale structures in a forced turbulent mixing layer. *J. Fluid Mech*, 150:23–39, 1985.

[46] M. Gharib, E. Rambod, and K. Shariff. A universal time scale for vortex ring formation. *J. Fluid Mech*, 360:121–140, 1998.

[47] M. Giles. Non-reflecting boundary conditions for Euler equations. *AIAA J.*, 28(12):2050–2058, 1990.

[48] A.E. Gill. On the behaviour of small disturbances to Poiseuille flow in a circular pipe. *J. Fluid Mech*, 21:145–147, 1967.

[49] D. Givoli. Non-reflecting boundary conditions. *J. Comp. Physics*, 94:1–29, 1991.

[50] D. Gottlieb and S. A. Orszag. *Numerical Analysis of Spectral Methods: Theory and Applications.* Society for Industrial and Applied Mathematics, 1977.

[51] M. D. Griffin, E. Jones, and J. D. Anderson. A computational fluid dynamic technique valid at the centerline for non-axisymmetric problems in cylindrical coordinates. *J. Comp. Physics*, 30:352–360, 1979.

[52] K. Gustafsson. The convergence rate for difference approximations to mixed initial boundary value problems. *Math. Comp.*, 29(130):396–406, 1975.

[53] D.C. Hill. Parabolized stability equations. *Ann. Rev. Fluid Mech.*, 29:245–283, 1997.

[54] R. Hixon, S.H. Shih, and R.R. Mankbadi. AIAA/CEAS Paper 95-0116, CEAS/AIAA, 1995.

[55] J.H. Horne and Baliunas. A prescription for the analysis of unevenly sampled time series. *Astrophys J.*, 302:757–763, 1986.

[56] F.Q. Hu. On absorbing boundary conditions for linearized Euler equations by a perfectly matched layer. *ICASE 95-70*, 1995.

[57] W. Huang and D M. Sloan. Pole condition for singular problems: The pseudo-spectral approximation. *J. Comp. Physics*, 107:254–261, 1993.

[58] G. Joyce and D. Montgomery. Negative temperature states for the two-dimensional guiding-centre plasma. *J. Plasma Physics*, 10(1):107–121, 1973.

[59] L. Kelvin. Vortex statics. *Phil. Mag.*, 10:97–109, 1880.

[60] R.H. Kraichnan. Inertial ranges in two-dimensional turbulence. *Phy. Fluids*, 10(7):1417–1423, 1967.

[61] R.H. Kraichnan. Statistical dynamics of two-dimensional flow. *J. Fluid Mech.*, 67:155–175, 1975.

[62] H. Lamb. *Hydrodynamics.* Dover Publications, New York, 6th edition, 1945.

[63] S.K. Lele. Compact finite difference schemes with spectral-like resolution. Technical Report 107, CTR, Stanford University, 1990.

[64] S.K. Lele. Compact finite difference schemes with spectral-like resolution. *J. Comp. Physics*, 103(1):16–42, 1992.

[65] H. R. Lewis and P. M. Bellan. Physical constraints on the coefficients of fourier expansions in cylindrical coordinates. *J. Math. Phys.*, 31(1):2592–2596, 1990.

[66] T.T. Lim and T.B. Nickels. Vortex rings. In S.I. Green, editor, *Fluid Vortices*, pages 95–153. Kluwer Academic Publishers, 1995.

[67] J.T.C. Liu. Developing large-scale wavelike eddies and the near jet noise field. *J. Fluid Mech*, 62:437–464, 1974.

[68] J.T.C. Liu. On eddy-Mach wave radiation source mechanism in the jet noise problem. AIAA Paper 71-0150, 1974.

[69] N.R. Lomb. Least-squares frequency analysis of unequally spaced data. *Astrophysics Space Science*, 39:447–462, 1976.

[70] H.J. Lugt. *Vortex flow in Nature and Technology.* Wiley-Interscience publication, New York, 1983.

[71] T.S. Lundgren and Y.B. Pointin. Statistical mechanics of two-dimensional vortices. *J. Stat. Phys.*, 17:323–355, 1977.

[72] R.R. Mankbadi, M.E. Hayer, and L.A. Povinelli. Structure of supersonic jet flow and its radiated sound. *AIAA J.*, 32(5):897–906, 1994.

[73] J.E. Marsden and T.S. Ratiu. *Introduction to Mechanics and Symmetry.* Springer-Verlag, New York, Inc., 1994.

[74] J.E. Marsden and A. Weinstein. Coadjoint orbits, vortices and clebsch variables for incompressible fluids. *Physica D*, 7:305–323, 1983.

[75] T. Matsushima and P. S. Marcus. A spectral method for polar coordinates. *J. Comp. Physics*, 120:365–374, 1995.

[76] P.D. McCormack and L. Crane. *Physical Fluid Dynamics.* Academic Press, New York, 1973.

[77] D.K. McLaughlin, J.M. Seiner, and H. Liu. On the noise generated by large scale instabilities in supersonic jets. AIAA Paper 80-0964, 1980.

[78] J.C. McWilliams. The emergence of isolated coherent vortices in turbulent flow. *J. Fluid Mech*, 146:21–43, 1984.

[79] P.E. Merilees. The pseudospectral approximation applied to the shallow water equations on a sphere. *Atmosphere*, 11(1):13–20, 1973.

[80] L. Merkine and J.T.C. Liu. On the development of noise-producing large-scale wave-like eddies in a plane turbulent jet. *J. Fluid Mech*, 70:353–368, 1975.

[81] J. Miller. Statistical mechanics of Euler equations in two dimensions. *Phys. Rev. Lett.*, 65(17):2137–2140, 1990.

[82] J. Miller, P.B. Weichman, and M.C. Cross. Statistical mechanics, Euler's equation, and Jupiter's red spot. *Physical Rev. A*, 45(4):2328–2359, 1992.

[83] B. E. Mitchell, S. K. Lele, and P. Moin. Direct computation of the sound generated by subsonic and supersonic axisymmetric jets. Report no. TF-66, Department of Mechanical Engineering, Stanford University, 1995.

[84] B. E. Mitchell, S. K. Lele, and P. Moin. Direct computation of the sound generated by an axisymmetric jet. *AIAA J.*, 35(10):1574–1580, 1997.

[85] K. Mohseni. Statistical equilibrium theory for axi-symmetric flows. 1999. to be published.

[86] K. Mohseni. Universality in von Karman street behind bluff bodies. *to be published*, 2000.

[87] K. Mohseni and T. Colonius. Polar coordinate singularities in pseudo-spectral and finite difference schemes. *Bulletin of the American Physical Society*, 42(11), 1997.

[88] K. Mohseni and T. Colonius. Numerical treatment of polar coordinate singularities. *J. Comp. Physics*, 157(2):787–795, 2000.

[89] K. Mohseni and M. Gharib. A model for universal time scale of vortex ring formation. *Phys. Fluids*, 10(10):2436–2438, 1998.

[90] K. Mohseni and J. Marsden. Accurate calculation of eigenfunctions of the Orr-Sommerfeld equations in pipe flows. *in preparation*, 2000.

[91] K. Mohseni, H. Ran, and T. Colonius. Numerical experiments on vortex formation. *J. Fluid Mech*, 1999. submitted.

[92] C.J. Moore. The role of shear layer instability waves in jet exhaust noise. *J. Fluid Mech*, 80:321–367, 1977.

[93] P.J. Morris. Flow characteristics of the large-scale wave-like structure of a supersonic round jet. *J. of Sound and Vibration*, 53:223–244, 1977.

[94] P.J. Morris and T.R.S. Bhat. The noise from supersonic elliptical jets. Technical Report 92-02-042, DGLR/AIAA 14th Aeroacoustic Conference, Aachen, Germany, 1992.

[95] P.J. Morris and T.R.S. Bhat. Supersonic elliptic jet noise. Technical Report AIAA Paper93-4409, 1993.

[96] P.J. Morris and T.R.S. Bhat. The spatial stability of compressible elliptic jets. *Phys. Fluids*, 7:185–194, 1995.

[97] P.J. Morris, L.N. Long, A. Bangalore, and Q. Wang. A parallel three-dimensional computational aeroacoustic method using nonlinear disturbance equations. *J. Comp. Physics*, 133:56–74, 1997.

[98] G.L. Morrison and D.K. McLaughlin. Instability process in low Reynolds number supersonic jets. *AIAAJ*, 18:793–800, 1980.

[99] P.J. Morrison. Hamiltonian field description of two-dimensional vortex fluids and guiding center plasmas. Technical Report PPPL-1783, Plasma Physics Laboratory, Princeton University, March 1981.

[100] A.H. Nayfeh and N.M. El-Hady. Nonparallel stability of compressible boundary layer flows. Technical Report Rep. No. VPI-E-79.13, Engineering Science and Mechanics Dept., Virginia Polytechnic and State University, Blacksburg, VA, 1980.

[101] J. Norbury. A family of steady vortex rings. *J. Fluid Mech*, 57(3):417–431, 1973.

[102] H. Oertel. Mach wave radiation of hot supersonic jets. In E.A. Muller, editor, *Mechanics of Sound Generation in Flows*, pages 275–281. Springer, 1979.

[103] H. Oertel. Mach wave radiation of hot supersonic jets investigated by means of the shock tube and new optical techniques. In A. Lifshitz and J. Rom, editors, *Shock Tubes and Waves*, pages 266–275, Jerusalem, 1979. 12th International Symposium on Shock Tubes and waves.

[104] H. Oertel. Coherent structures producing Mach waves inside and outside of the supersonic jet. In R. Dumas and L. Fulachier, editors, *Structure of Complex Turbulent Shear Flow*, pages 334–343. IUTAM Symposium Marseille, Springer-Verlag, 1982.

[105] L. Onsager. Statistical hydrodynamics. *Nuovo Cimento Suppl.*, 6:279–287, 1949.

[106] S. Orszag. Accurate solution of the Orr-Sommerfeld stability equation. *J. Fluid Mech*, 50(4):689–703, 1971.

[107] D. Papamoschou and A. Roshko. The compressible turbulent shear layer: an experimental study. *J. Fluid Mech*, 197:453–477, 1988.

[108] D. Papamoschou and A. Roshko. Structure of the compressible shear layer. AIAA-paper 90-0126, AIAA, Jan. 1989.

[109] R.A. Petersen and M.M. Samet. On the preferred mode of jet instability. *J. Fluid Mech*, 194:153–173, 1988.

[110] O.M. Phillips. On the generation of sound by turbulent shear layers. *J. Fluid Mech*, 9(1):1–28, 1960.

[111] W.H. Press and G.B. Rybicki. Fast algorithm for spectral analysis of unevenly sampled data. *Astrophysical J.*, 338:277–280, 1989.

[112] W.H. Press, S.A. Teukolsky, W.T. Vetterling, and B.P. Flannery. *Numerical Recipes*. Cambridge Univ. Press, 2nd edition, 1992.

[113] M.M. Rai and P. Moin. Direct numerical simulation of transition and turbulence in a spatially evolving boundary layer. *J. Comp. Phys.*, 109(2):169–192, 1991.

[114] G. Raman. Supersonic jet screech: Half-century from powell to the present. *J. Sound and Vibration*, 225(3):543–571, 1999.

[115] R. Robert and J. Sommeria. Statistical equilibrium states for two-dimensional flows. *J. Fluid Mech*, 229:291–310, 1991.

[116] P.H. Roberts. A Hamiltonian theory for weakly interacting vortices. *Mathematika*, 19:169–179, 1972.

[117] M. Rosenfeld, E. Rambod, and M. Gharib. Circulation and formation number of laminar vortex rings. *J. Fluid Mech*, 376:297–318, 1998.

[118] P.G. Saffman. *Vortex Dynamics*. Cambridge University Press, 1992.

[119] P.G. Saffman and R. Szeto. Equilibrium shapes of a pair of equal uniform vortices. *Phys. Fluids*, 23(12):2339–2342, 1980.

[120] J.D. Scargle. Studies in astronomical time series analysis. II. statistical aspects of spectral analysis of unevely spaced data. *Astrophys J.*, 302:757–763, 1982.

[121] M. Schulz and K. Stattegger. Spectrum: Spectral analysis of unevenly spaced paleoclimatic time series. *Computers and Geosciences*, 23(9):929–945, 1997.

[122] T.K. Sedelnikov. The frequency spectrum of the noise of a supersonic jet. *Phys. Aero. Noise.*, Nauka:Transl. 1969 *NASA TTF*–538, pp. 71–75, 1967.

[123] J.M. Seiner, M.K. Ponton, B.J. Jansen, and N.T. Lagen. The effect of temperature on supersonic jet noise emission. Technical Report AIAA Paper92-02-046, DGLR/AIAA 14th Aeroacoustic Conference, Aachen, Germany, 1992.

[124] K. Shariff and A. Leonard. Vortex rings. *Ann. Rev. Fluid Mech.*, 34:235–279, 1992.

[125] K. Shariff, A. Leonard, and J.H. Ferziger. Dynamics of a class of vortex rings. TM-102257, NASA, December 1989.

[126] S.H. Shih, R. Hixon, and R.R. Mankbadi. Three-dimensional structure in a supersonic jet: behavior near centerline. AIAA Paper-95-0681, 1995.

[127] M. Shusser and M. Gharib. A model for vortex ring formation in a starting buoyant plume. *J. Fluid Mech*, 2000. accepted for publication.

[128] B.L. Smith and A. Glezer. The formation and evolution of synthetic jets. *Phys. Fluids*, 10(9):2281–2297, 1998.

[129] S. K. Stanaway and B. J. Cantwell. A numerical study of viscous vortex rings using a spectral method. NASA TM- 101041, 1988.

[130] J.T. Stuart. On the non-linear mechanics of hydrodynamic stability. *J. Fluid Mech*, 4:1–21, 1958.

[131] J.P. Sullivan, S.E. Widnall, and S. Ezekiel. Study of vortex rings using a laser doppler velocimeter. *AIAA J.*, 11(10):1384–1389, 1973.

[132] J.P. Sullivan, S.E. Widnall, and S. Ezekiel. Study of vortex rings using a laser doppler velocimeter. *AIAA J.*, 11:1384–1386, 1973.

[133] J.D. Swearingen, J.D. Crouch, and R.A. Handler. Dynamics and stability of a vortex ring impacting a solid boundary. *J. Fluid Mech*, 297:1–28, 1995.

[134] A. Szeri and P. Holmes. Nonlinear stability of axisymmetric swirling flows. *Phil. Trans. R. Soc. London A*, 326:327–354, 1988.

[135] S. Taasan and D.M. Nark. An absorbing buffer zone technique for acoustic wave propagation. *AIAA Paper95-0146*, 1995.

[136] C.K.W. Tam. Directional acoustic radiation from a supersonic jet generated by shear layer instability. *J. Fluid Mech*, 46:757–768, 1971.

[137] C.K.W. Tam. On the noise of a nearly ideally expanded supersonic jet. *J. Fluid Mech*, 51:69–95, 1972.

[138] C.K.W. Tam. Supersonic jet noise generated by large-scale disturbances. *J. of Sound and Vibration*, 38:51–79, 1975.

[139] C.K.W. Tam. Stochastic model theory of broadband shock associated noise from supersonic jets. *J. of Sound and Vibration*, 116:265–302, 1987.

[140] C.K.W. Tam. *Aeroacoustics of Flight Vehicles: Theory and Practice*, volume 1: Noise Source, chapter Jet noise generated by large-scale coherent motion, pages 311–390. NASA RP-1258, 1991.

[141] C.K.W. Tam. Supersonic jet noise. *Ann. Rev. Fluid Mech.*, 27:17–43, 1995.

[142] C.K.W. Tam and D. Burton. Sound generation by instability waves of supersonic flows. part 1. two-dimensional mixing layers. *J. Fluid Mech*, 138:249–271, 1984.

[143] C.K.W. Tam and D. Burton. Sound generation by instability waves of supersonic flows. part 2. axisymmetric jets. *J. Fluid Mech*, 138:273–295, 1984.

[144] C.K.W. Tam and P. Chen. Turbulent mixing noise from supersonic jets. *AIAA J.*, 32(9):1774–1780, 1994.

[145] C.K.W. Tam, P. Chen, and J.M. Seiner. Relationship between instability waves and noise of high-speed jets. *AIAA J.*, 30(7):1747–1752, 1992.

[146] C.K.W. Tam and F.Q. Hu. On the three families of instability waves of high-speed jets. *J. Fluid Mech*, 201:447–483, 1989.

[147] C.K.W. Tam and P.J. Morris. The radiation of sound by the instability waves of a compressible plane turbulent shear layer. *J. Fluid Mech*, 98:349–381, 1980.

[148] C.K.W. Tam and J.C. Webb. Dispersion relation preserving finite difference schemes for computational acoustics. *J. Comp. Physics*, 107:262–281, 1993.

[149] K.W. Thompson. Time dependent boundary conditions for hyperbolic systems. *J. Comp. Physics*, 68:1–24, 1987.

[150] P.A. Thompson. *Compressible-Fluid Dynamics*. McGraw-Hill Book Company, 2nd edition, 1972.

[151] L. N. Trefethen. Group velocity in finite difference schemes. *SIAM Review*, 124(2):113–136, 1982.

[152] T.R. Troutt and D.K. McLaughlin. Experiments on the flow and acoustic properties of a moderate-Reynolds-number supersonic jet. *J. Fluid Mech*, 116:123–156, 1982.

[153] R. Verzicco and P. Orlandi. A finite-difference scheme for three-dimensional incompressible flows in cylindrical coordinates. *J. Comp. Physics*, 123:402–414, 1996.

[154] R. Verzicco, P. Orlandi, A.H.M. Eisenga, G.J.F. van Heijst, and G.F. Carnevale. Dynamics of a vortex ring in a rotating fluid. *J. Fluid Mech*, 317:215–239, 1996.

[155] R. Vichnevetsky and J. B. Bowles. *Fourier Analysis of Numerical Approximations of Hyperbolic Equations*. SIAM, Philadelphia, 1982.

[156] Y.H. Wan. Variational principles for Hill's spherical vortex and nearly spherical vortices. *Trans. Am. Math. Soc.*, 308(1):299–312, 1988.

[157] P.B. Weichman. Statistical mechanics, Euler's equation, and Jupiter's red spot. In *Nonlinear waves and weak turbulence with applications in oceanography and condensed matter physics (Cleveland, OH, 1992)*, pages 239–277. Birkhuser Boston, Boston, MA, 1993.

[158] P.B. Weichman and D. Petrich. Shallow water equilibria. 1999. in preparation.

[159] A. Weigand and M. Gharib. On the evolution of laminar vortex rings. *Experiments in Fluids*, 22:447–457, 1997.

[160] F.M. White. *Viscous Fluid Flow.* McGraw-Hill Book Company, 2nd edition, 1992.

[161] J.E. Ffowcs Williams. The noise from turbulence convected at high speed. *Philosophical Transactions of the Royal Society of London, Ser. A*, 225(1061):469–503, 1963.

[162] S. Wolfram. *Mathematica.* Wolfram Research, Inc., 2.2 edition, 1994.